DRIFT WAVE ION FLUID VELOCITY FIELD MEASURED BY PLANAR LASER INDUCED FLUORESCENCE

Thesis by

Andrew Dewey Bailey III

In Partial Fulfillment of the Requirements

for the Degree of

Doctor of Philosophy

California Institute of Technology

Pasadena, California

1993

(Defended February 17, 1993)

ACKNOWLEDGEMENTS

I want to thank my parents Andrew and Irene Bailey, Jr. for teaching me that to achieve ambitious goals I must accept the risk of failure, patiently work as hard as I can, revel in the effort, laugh at my mistakes and savor the moments of success before starting all over again.

My advisor Professor Paul Bellan has always given me his full support during my years at Caltech. This work would have suffered without his insightful comments and careful direction. Professor Raul Stern of the University of Colorado - Boulder spent many hours in the lab teaching me the tricks of the trade and sharing his experimental expertise, especially in laser induced fluorescence. I feel incredibly fortunate to have had the opportunity to work with two plasma physicists who are not only exceptional in the field, but who also enriched my life with their humor and kindness. I also want to thank Frank Cosso for helping me build, rebuild and maintain much of the apparatus used in this experiment, Dr. Michael Brown for his friendship and constant interest in my work, Steve Sanders for proofreading this thesis and my wife Lauren Purcell for her love and support during the past two and a half years filled with change for both of us.

During my first three years as a graduate student I was supported by a DOE Fusion Science Fellowship. The experiment was performed under NSF Grants PHY-8707338 and PHY-9114146.

ABSTRACT

The first plasma planar laser induced fluorescence (PLIF) diagnostic has been developed and used to study Ar plasma discharges in Caltech's Encore tokamak. The first two-dimensional time resolved measurements of the ion fluid velocity have been made with this diagnostic. PLIF excited in a poloidal cross section by a narrow linewidth laser sheet is imaged onto a 10x10 anode microchannel plate photomultiplier. Both the ion temperature and one component of the fluid velocity of metastable ArII ions are measured by scanning the laser wavelength through the Doppler broadened and shifted PLIF absorption line. The maximum measured wavelength shifts correspond to velocities $\sim (1.5 \pm 0.08) \times 10^5$cm/s. A periodic spatial structure in the fluid velocity field is observed to oscillate in phase with a coherent, large amplitude, mostly electrostatic drift-Alfvén wave with poloidal and toroidal mode numbers m = 2, n = 1. Previous work (McChesney '87) indicates that the anomalously hot ion temperatures measured ($\langle T_i \rangle \approx 6$eV) are due to stochastic ion motion in the drift waves. Using PLIF, oscillations in the temperature ($\tilde{T}_i \sim 3$eV) out of phase with the drift wave potential have been observed for the first time.

To provide an interpretation of the PLIF fluid velocity data, Langmuir probe measurements were made in a nearby poloidal cross section. The calculated ion fluid flow pattern in the drift approximation agreed qualitatively with the measured velocity field, but the calculations predict much larger velocities than are measured. The general agreement, despite the stochastic dynamics, emphasizes the robust nature of the two-fluid description of the plasma. The discrepancies with the PLIF measurements also highlight the need for a better understanding of the relationship between stochastic particle dynamics and macroscopic plasma parameters.

An *explicit* connection is made between the ion distribution and Poincaré maps of the single particle dynamics in prescribed mean fields by considering the characteristics of the collisionless Vlasov equation. A self-consistent distribution function is restricted to being constant in stochastic regions of phase space where one particle orbit comes arbitrarily close to any point in the region. The implications of this viewpoint are explored for a simplified model of the drift wave. When the bulk of the ions are stochastic, the center of the distribution function is flattened leading to higher ion 'temperatures' derived from Maxwellian fits, but the envelope of the stochastic region and thus the fluid velocity and temperature continue to oscillate periodically with the wave despite the nonperiodicity of the individual particle orbits.

Contents

Figures

Tables

1

Introduction

Despite the fundamental nature of the velocity field in a plasma, velocity field measurements are rarely made due to their experimental difficulty. Two general techniques have previously been used to measure ion fluid velocities. The Doppler shifts of *spontaneously* emitted lines of impurity and charge exchange ions have been used to measure rotation profiles of plasmas during spheromak formation (Peyser '88) and H-mode transitions in tokamaks (Groebner '90, Ida '90). For this method, interpretation of data from the experiments depends on detailed plasma models and Abel inversion of chord averaged measurements. A directly interpreted and more spatially localized method is laser *induced* fluorescence (LIF). High spatial resolution is possible with LIF because the diagnosed plasma volume is determined by the intersection of the exciting laser and the plasma viewed by the detection optics. When Doppler shifts due to ion motion dominate the absorption linewidth, LIF excited by scanning the *wavelength* of a narrow linewidth laser gives the ion *velocity* distribution directly. This technique has been used to obtain rotation profiles in a plasma column by measuring the Doppler shifted peaks of majority ion velocity distributions (Anderegg '86). LIF has also been used to make detailed, time resolved measurements of ion velocity distributions in *one* spatial dimension in driven electrostatic waves (McWilliams '86, Skiff '87b).

This thesis describes time resolved *planar* laser induced fluorescence (PLIF) measurements of one component of the majority ion fluid velocity field in an undriven drift-Alfvén wave in a poloidal cross section of a tokamak. A sheet of narrow linewidth laser light is used to excite LIF in a plane inside the plasma which is then imaged onto a detector. These are the first ion fluid velocity field

measurements reported in *two* spatial dimensions. Although PLIF from atoms has been used in fluid visualization for a number of years (Kychakoff '82), these are also the first PLIF images from plasma ions.

The experiments were conducted on Ar discharges in Caltech's Encore tokamak. The discharges were dominated by reproducible, coherent, nearly electrostatic drift-Alfvén waves. Fredrickson ('85) identified the waves in Encore by comparing Langmuir probe measurements to a two-fluid model of the drift-Alfvén waves. Chapter 2 describes Encore and an extensive probe characterization of the plasma. A scanning Langmuir probe was used to measure plasma parameters in a poloidal cross section. The measured density, plasma potential and electron temperature all oscillate in the dominant m = 2 poloidal mode of the drift wave. McChesney ('87, '89, '91) also studied the ion temperatures in similar drift waves in Encore using single point LIF. It was discovered that the ions are anomalously hot due to stochastic ion motion in the drift wave. These LIF results stimulated the development of the plasma PLIF diagnostic system.

The essential physical principles used in LIF support a number of extremely powerful diagnostic tools which have been used in plasmas since 1975 (Stern '75). The plasma PLIF diagnostic extends these techniques and presents new experimental opportunities. Chapter 3 outlines the history and techniques of LIF in plasma physics. The unique capabilities and possibilities of PLIF in plasmas are also described. Imaging the ion density in a thin sheet on extremely fast time scales without severe spatial averaging was a goal of the PLIF system on Encore. Chapter 4 addresses a number of questions which must be answered before quantitative single shot ion density measurements are practical.

LIF depends on pumping bound electrons from a highly populated low energy quantum state to a higher energy state with a laser in resonance with the

transition. The increased spontaneous emission from the upper state is the laser *induced* fluorescence. A metastable of ArII is the pumped state in the Encore PLIF experiment. Predicting the initial population of a metastable as a function of the total ion density is a very difficult problem. In Chapter 4 the results of a model including the dominant metastable reactions illustrate the sensitivity of the metastable population to the electron density and temperature in regimes appropriate to the Encore plasmas. The metastable density is too sensitive to the exact plasma conditions to make direct interpretation of LIF metastable density measurements possible with the current model.

Using LIF to measure metastable densities or velocity distributions requires an understanding of the physics of LIF. In Chapter 4 a semi-classical model of the LIF interaction is used to relate the fluorescence to the metastable population as a function of laser parameters and the initial ion velocity distribution. The LIF signal estimated by combining both models is in good agreement with an estimate based on single point LIF *data* from a plasma.

The details of the PLIF system developed on Encore are described in Chapter 5. The heart of the diagnostic is a 10x10 anode microchannel plate photomultiplier (MCP PMT) which detects the weak PLIF signal, provides most of the gain in the system and maintains the spatial resolution of the optical image. A significant fraction of a poloidal cross section centered on the m = 2 mode of the drift wave in Encore is imaged with $\sim 1 cm^2$ resolution.

The PLIF experimental results are presented in Chapter 6. A wavelength scanning narrow linewidth laser is used to measure the Doppler broadened and shifted absorption line of metastable ArII ions at a number of times during the discharge. The PLIF data is then χ^2 fit to a Maxwellian. The width of the distribution is a measurement of the ion temperature and the shift in the peak of

the distribution is a measurement of the component of the ion fluid velocity u_R in the direction of laser propagation. A periodic spatial structure in the u_R field is observed to oscillate in phase with the drift wave ($|u_{max}| \sim (1.5 \pm 0.08) \times 10^5 cm/s$).

The complete two-dimensional velocity flow field consistent with the PLIF measurements is not immediately obvious since only a single velocity component is measured. The interpretation is also complicated by the fact that the Encore plasma is not a uniform plasma with a controlled, single mode, monochromatic perturbation, but a dynamic plasma dominated by the naturally occurring, spatially complex, time dependent drift wave. Rather than using analytic functions approximating the plasma parameters when interpreting the PLIF data, the Langmuir probe measurements made in a nearby poloidal cross section were used to calculate the ion fluid velocity in the drift approximation. The measured and calculated velocity flow patterns agree qualitatively in space, but disagree in magnitude. In the m = 2 drift-Alfvén waves, the ion fluid is flowing in two pairs of counter-rotating vortices around the potential hills and valleys of the wave. As the entire mode structure rotates, the direction of the u_R components oscillate in the imaged plasma.

The mean PLIF measured ion temperatures in these discharges are observed to be much higher than predicted by standard ion heating mechanisms in agreement with earlier single point LIF measurements (McChesney '87). Previously unobserved fluctuations of the ion temperatures out of phase with the plasma potential in the drift waves were also observed with the PLIF data ($\tilde{T}_i \sim 3eV$). Although stochastic ion motion in the drift waves is the primary ion heating mechanism in Encore (McChesney '87), it is not clear how the stochastic dynamics of ions in the bulk of the distribution affect the ion fluid velocity or the detailed behavior of the ion temperatures.

Combining these time resolved PLIF *measurements* with the Langmuir probe *measurements* in the same Encore discharge provides temporally and spatially resolved T_i, T_e, ϕ_p, n and u_R data which place new stringent levels of accuracy on any description of the plasma. The increasingly complete and detailed picture of the drift waves in Encore challenges the limits of standard theoretical approaches. Since the characteristic frequencies (wave and ion cyclotron) and spatial scales (ion gyroradius, wavelength and density gradient scale length) are not well separated as required by the drift approximation, it is surprising that the drift approximation predicts the observed fluid velocity field as well as it does.

The qualitative agreement between the calculations and the PLIF measurements, despite the stochastic dynamics, emphasizes the robust nature of the fluid equations as a description of the plasma. This might be expected since the waves were identified using a two-fluid model (Fredrickson '85). On the other hand the discrepancies between the PLIF measurements and the calculations highlight the need for a self-consistent treatment of the plasma. Moments of the ion distribution function are observed to differ from drift theory predictions for the wave: the temperatures are very high and have large oscillations in phase with the wave and the fluid velocity magnitudes are lower than predicted.

A novel approach to understanding the relationship between the stochastic single particle dynamics and macroscopic plasma parameters is developed in Chapter 7. An *explicit* connection between the ion distribution function and Poincaré maps of the single particle dynamics in prescribed mean fields is made by considering the characteristics of the collisionless Vlasov equation. A self-consistent distribution function is restricted to a constant in stochastic regions of phase space where one particle orbit comes arbitrarily close to any point in the region. The implications of this view are explored for a simplified model of the drift wave in

Encore. When the ions in the bulk of the distribution are stochastic, the center of the distribution function is flattened leading to higher ion 'temperatures' derived from Maxwellian fits. Although the stochasticity affects the bulk of the distribution, the center of the envelope of the stochastic region and thus the fluid velocity continues to oscillate periodically with the wave despite the nonperiodicity of the individual particle orbits. The width of the envelope, i.e., the temperature, also oscillates. This new point of view shows promise for integrating the experimental observations.

A summary of the thesis results is given in Chapter 8. A number of appendices follow which contain detailed presentations of calculations and related work which would have interrupted the exposition in the main text. The outline of the derivation of the drift-Alfvén dispersion in Appendix A supports comments in Chapter 2. Appendix B contains an original evaluation of LIF and tagging schemes in terms of the atomic parameters, laser pulse length and plasma conditions. It also contains the first comprehensive compilation of the LIF schemes based on the ArII metastable states. Appendices C and D present the details of the metastable population and semi-classical LIF models discussed in Chapter 4. Appendix E describes technical aspects of the design of the PLIF optical system and the program LENSYS which was used in designing the system and calculating system performance. Appendix F contains additional comments primarily of interest to experimentalists planning to use Encore in the future.

2

CALTECH'S ENCORE TOKAMAK PLASMA

2.1 Drift Waves in Encore

The experiments described in this thesis were conducted on Caltech's Encore tokamak. The word tokamak refers to the magnetic field topology which is the leading candidate to confine a plasma for a thermonuclear fusion reactor. The Encore tokamak is used primarily as a versatile plasma source for studying basic plasma physics. Usually, a tokamak is a toroidal (doughnut shaped) vacuum vessel filled with a gas (argon at 3.5×10^{-5} torr in this case) which acts as a single turn secondary of a transformer (see Figure 2.1). When the the flux through the center of the tokamak is changing, inducing a voltage around the torus, the gas is broken down and the plasma current I_p flows in the toroidal direction. The poloidal magnetic field (in the short direction) due to the toroidal current tends to confine the plasma. Since this configuration alone would be unstable, e.g., to the kink instability, a strong stabilizing toroidal magnetic field B_ϕ is applied with external coils. Thus, the characteristic magnetic field lines in a tokamak are toroidally helical, the sum of the strong applied toroidal field and the weaker poloidal field due to the plasma current. Further details of tokamak operation can be found elsewhere (e.g., Wesson '87).

Caltech's Encore tokamak (see Figure 2.1) is a small, high repetition rate tokamak (major radius R = 38.1cm, minor radius a = 12.8cm, rep. rate 15 Hz). The unusually high repetition rate is achieved by using a constant toroidal magnetic field and a high power audio frequency amplifier to drive the transformer primary.

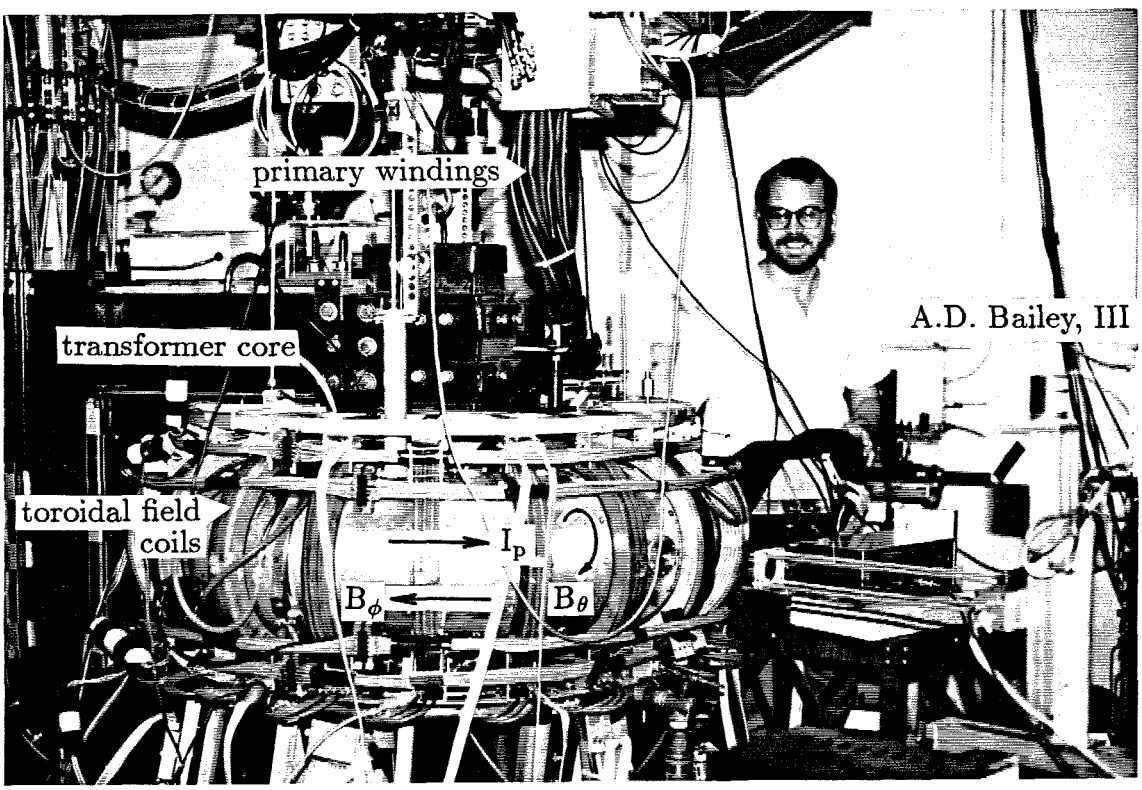

Figure 2.1 : Photograph of the Encore tokamak and identification of critical components. The magnetic and current directions shown are correct for the experiments described in this thesis.

The nearly fully ionized Ar plasma parameters used in these experiments were as follows: plasma density $n \approx 10^{12}cm^{-3}$, electron temperature $\langle T_e \rangle \approx 10eV$, ion temperature $\langle T_i \rangle \approx 6eV$, peak plasma current $I_p = 1.35kA$ and constant toroidal magnetic field $B_\phi = 275$ gauss on axis giving an ion cyclotron frequency $f_{ci} \approx 10kHz$. Figure 2.2 shows the plasma current and the toroidal loop voltage V_{loop} induced by the transformer for the discharges used in this work. The Ar discharges in Encore are dominated by drift-Alfvén waves which were coherent in the plasmas used in these experiments. The waves in Encore were first investigated with probes and identified as drift-Alfvén waves by comparing measured parameters to a linear two-fluid theory of the coupling of the drift and shear-Alfvén modes (Fredrickson '85).

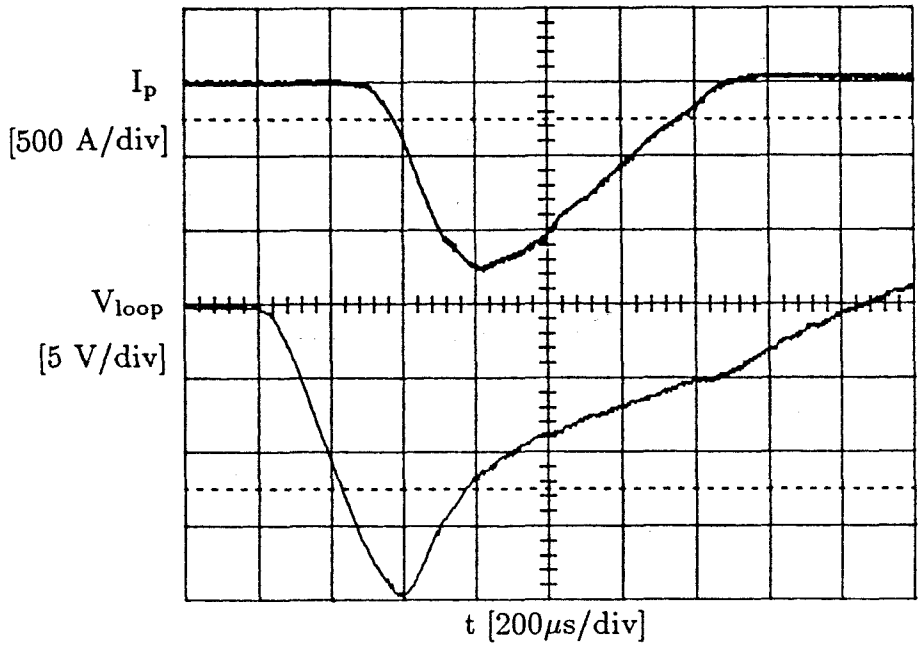

Figure 2.2 : Oscilloscope traces of the plasma current measured with a Rogowski coil (top) and the loop voltage measured with a single turn magnetic coil (bottom) for the plasmas used in the thesis.

The drift wave is an electrostatic wave driven by density and temperature gradients across magnetic fields. To be unstable, the wave density and field fluctuations must be slightly out of phase either due to electron-ion collisions, Landau damping or an electron drift parallel to the magnetic field such as the plasma current. In Encore the drift waves are primarily current driven and propagate nearly perpendicular to the magnetic field in the electron diamagnetic direction. The oscillating currents in the wave along the magnetic field cause their own magnetic fluctuations which couple the electrostatic drift wave to the shear-Alfvén wave. The dispersion for the drift-Alfvén wave can be derived via two-fluid or kinetic approachs (see Appendix A) which give the real part of the wave frequency as

$$\omega_r = \frac{\omega_*}{1+b}\left[1 - \left(\frac{\omega_*}{k_z v_A}\right)^2 \frac{b}{(1+b)^3}\right]$$

where k_z and $k_\perp$ are the wave numbers parallel and perpendicular to the magnetic field, $v_A = (B^2/nm_i\mu_o)^{1/2}$ is the Alfvén velocity, $\omega^* = -k_\perp \nabla(nT_e)/enB$ is the diamagnetic drift frequency, $\rho_s^2 = T_e/m_i\omega_{ci}^2$ and $b = k_\perp^2\rho_s^2$. In Encore the observed wave frequency $f \sim 5$kHz is in good agreement with this expression.

Langmuir probes were used to determine the dominant poloidal and toroidal modes of the waves in these experiments. A stepper motor driven Langmuir probe (Fredrickson '85) was used to characterize the plasma on a 10x10 R-z grid in a poloidal cross section (see Figure 2.3) and a fixed probe was used to monitor the plasma reproducibility. The probes are made of tungsten wire in an alumina sheath leaving ~4mm tips exposed to the plasma (wire diameters: 0.25mm for the fixed probe, 0.75mm for the R-z scanning probe). The plasma in Encore is sufficiently benign to allow full insertion of probes without damage.

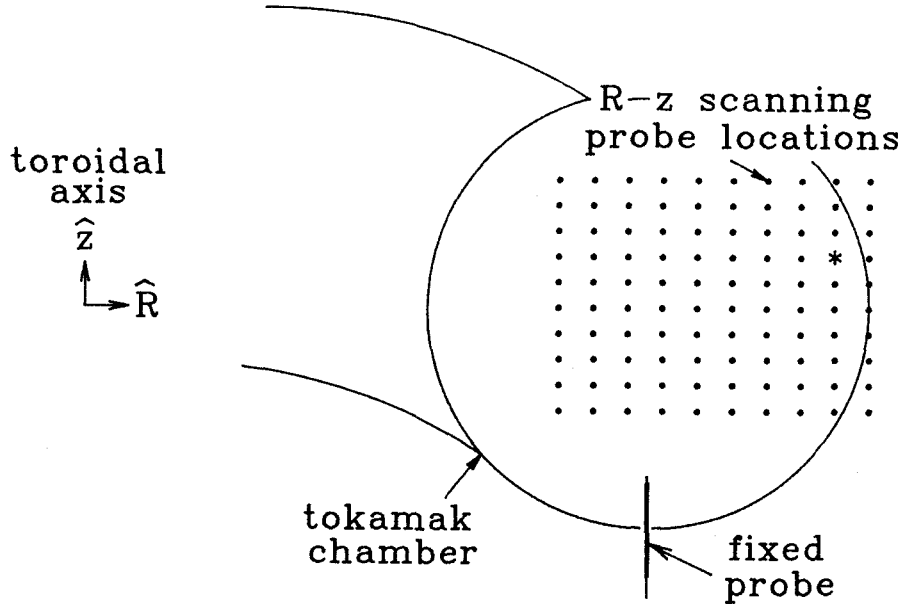

Figure 2.3 : Poloidal cross section showing access of R-z scanning Langmuir probe and the fixed probe location. The fixed probe is in the same cross section used for PLIF, separated toroidally by $\pi/5$ from the R-z scanning probe cross section. The position for the data in Figure 2.7 is marked with *.

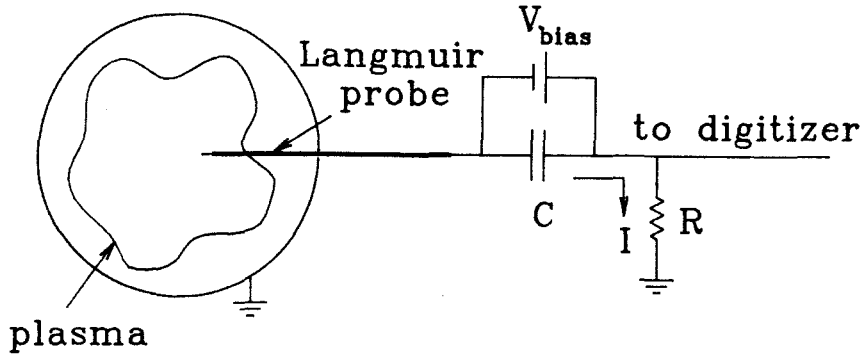

Figure 2.4 : Langmuir probe circuit. For the data presented in the thesis C=380μf, R=5.5Ω for $V_{bias} \geq -25V$ and R=200Ω for $V_{bias} \leq -30V$.

The plasma density n, electron temperature T_e and plasma potential ϕ_p can be measured using unmagnetized probe theory (Hutchinson '87) to describe the current to the probe I as a function of the probe bias voltage V_{bias} (see Figure 2.4 for bias circuit). T_e is found from the inverse of the slope of $\ln(I_i - I)$ vs V where I_i is the current due to the ions. The plasma potential is calculated from

$$\phi_p = \phi_f + \frac{T_e}{2}\left[\ln\left(\frac{m_i}{2\pi m_e}\right) + 1\right]$$

where ϕ_f is the floating potential of the probe, i.e., the bias voltage which draws no current. Figure 2.5 shows a measured and fitted I-V characteristic and the linear fit used to find the electron temperature. The density is found by biasing the probe very negative to collect the ion saturation current $I_{is} = enAc_s \exp(-1/2)$ where A is the probe collection area, n the density far from the probe, the ion acoustic speed is $c_s = (T_e/m_i)^{1/2}$ and the exponential factor enters from the conservation of ion flux through the presheath potential drop of $T_e/2e$ (Hutchinson '87). Figure 2.6 shows the coherent (primarily density) oscillations of the wave measured with a Langmuir probe biased to collect the ion saturation current in the plasma edge.

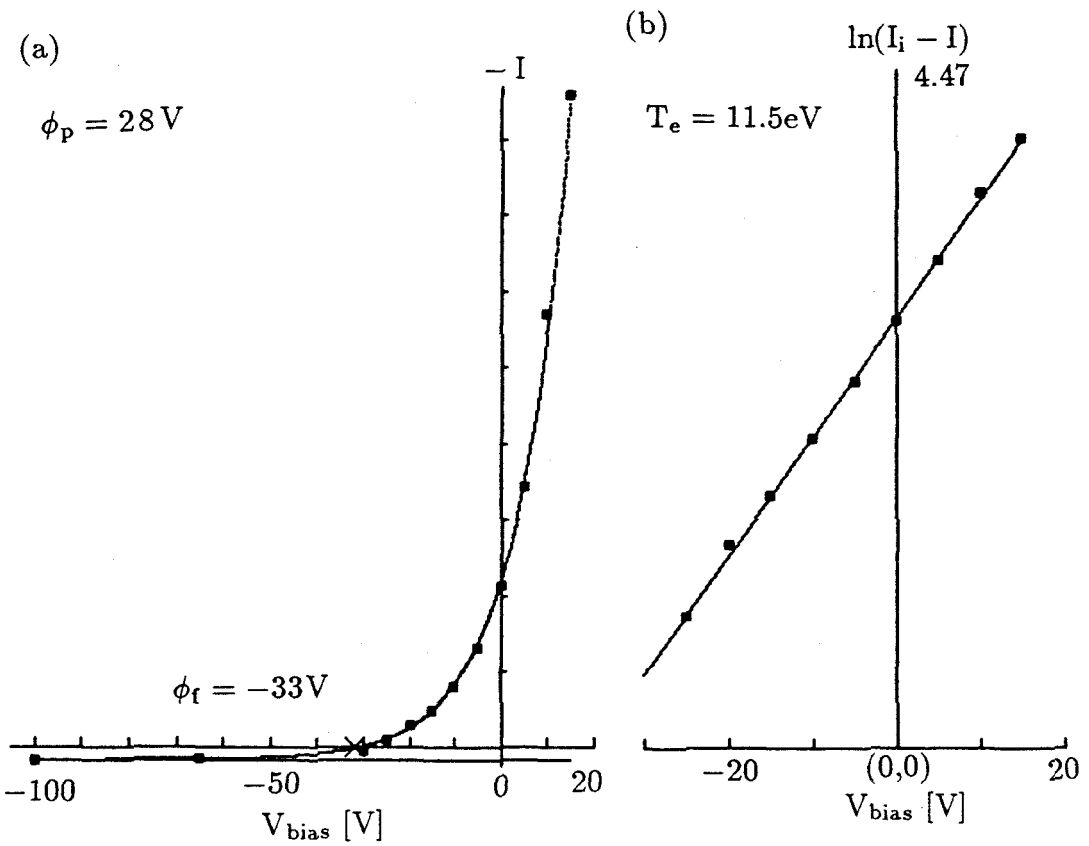

Figure 2.5 : (a) Probe I-V trace. Squares are raw data points. The data from the lowest two or three points are used to determine the ion current (straight line below horizontal axis) which is subtracted from the remaining points to calculate the electron current. The curve is the fit based on the unmagnetized probe theory. The floating potential (marked with an X) used in the calculations was based on the zero crossing of the analytic I-V trace. For this trace $\phi_f = -33V$, $\phi_p = 28V$, vertical scale -10 to 372 mA. (b) The good (but not unusual) fit used to determine T_e in this case.

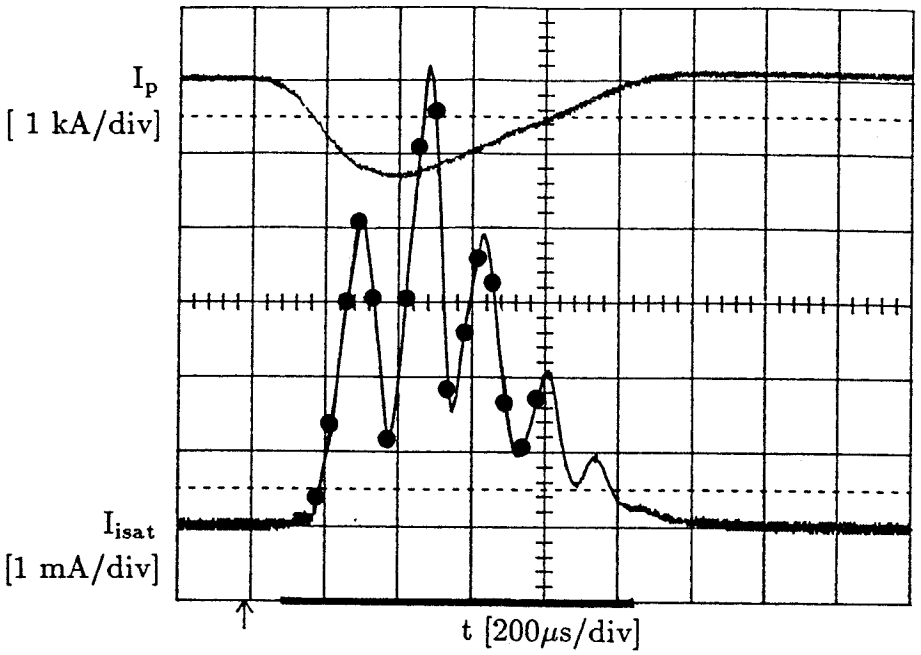

Figure 2.6 : Ion saturation current to the fixed probe in the edge (lower trace) with the plasma current. The probe position is displayed in Figure 2.3. Langmuir probe measurements at each position in the R-z probe scan were made in 10μs intervals during the time indicated by the heavy bar on the time axis. Filled circles mark the times for the data displayed in Figure 2.8.

The R-z scanning Langmuir probe data, averaged over 5 discharges at each point, was collected using a computer to control the probe position and bias (12 voltages, Kepco BOP 100-2M) and a computer aided measurement and control (CAMAC) digitizer (5MHz, 8 bit, BiRa 5326). These data represent the most extensive probe characterization of an Encore discharge to date. The probe measurements and the PLIF data to be presented in Chapter 6 were taken during an uninterrupted night of Encore discharges with the same machine conditions

reported earlier in this chapter. Figure 2.7 shows the plasma parameters n, ϕ_p, T_e and ϕ_f at one point in the plasma. The errors in the T_e fits during the majority of the discharge are $\sigma_{T_e}/T_e \sim 0.05$ (see Appendix F). Given the estimated uncertainty in the floating potential of $\sigma_{\phi_f}/\phi_f \sim 0.1$, the calculated plasma potentials have uncertainties $\sigma_{\phi_p}/\phi_p \sim 0.28$. Figure 2.8 shows smoothed images of the plasma parameters in the whole cross section at a number of times during the discharge. The frequencies, amplitudes and phases of the fluctuating parameters vary in time and space, but (in very general terms) the drift wave dominates the discharge with $\tilde{n}/n \approx 0.5$-1, $\tilde{\phi}_p \sim 5$-7V and $\tilde{T}_e \sim 3$eV. In the fluctuating parameters, the density leads the potential by $\sim \pi/4$ and the electron temperature by $\sim \pi/3$. The dominant m = 2 poloidal mode of the drift wave rotating in the electron diamagnetic direction is apparent in all the parameters (see Figure 2.8). The toroidal mode number in the edge was determined to be n = 1 using probes in five toroidal positions.

Although the magnetic fluctuations were not measured in these discharges, an estimate on the magnitude of the Alfvén portion of the wave can be made. According to the equations used to derive the drift-Alfvén dispersion in Appendix A, the plasma behavior deviates from being Boltzmann ($\tilde{n}/n = e\tilde{\phi}/T_e$) by an amount proportional to the Alfvén character of the wave.

$$\frac{\tilde{n}}{n} = \frac{e}{T_e}\left(\tilde{\phi} + \frac{\omega|\tilde{B}_\perp|}{k_\perp k_z}\left(\frac{\omega_*}{\omega} - 1\right)\right).$$

By calculating $\tilde{n}/n$ and $e\tilde{\phi}/T_e$ from the probe data, the drift waves in these experiments were found to be mostly electrostatic and very nearly Boltzmann. The estimated $\tilde{B}_\perp \sim 2$-5 gauss gives a ratio of Alfvén to electrostatic wave components $\omega A_\parallel / k_\parallel \tilde{\phi} \lesssim 0.1$.

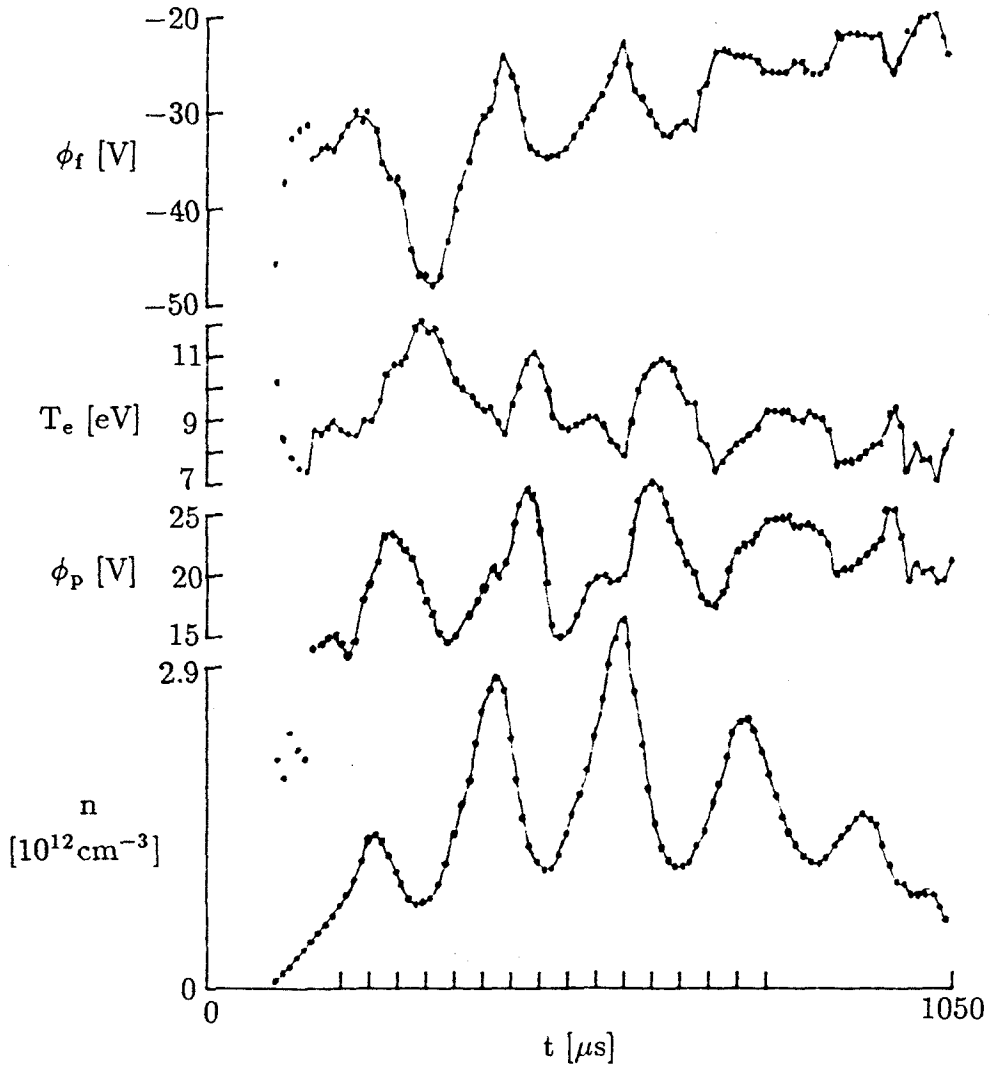

Figure 2.7 : Plasma parameters at one point in the plasma (see Figure 2.3 for position). Tics on time axis mark times for Figure 2.8.

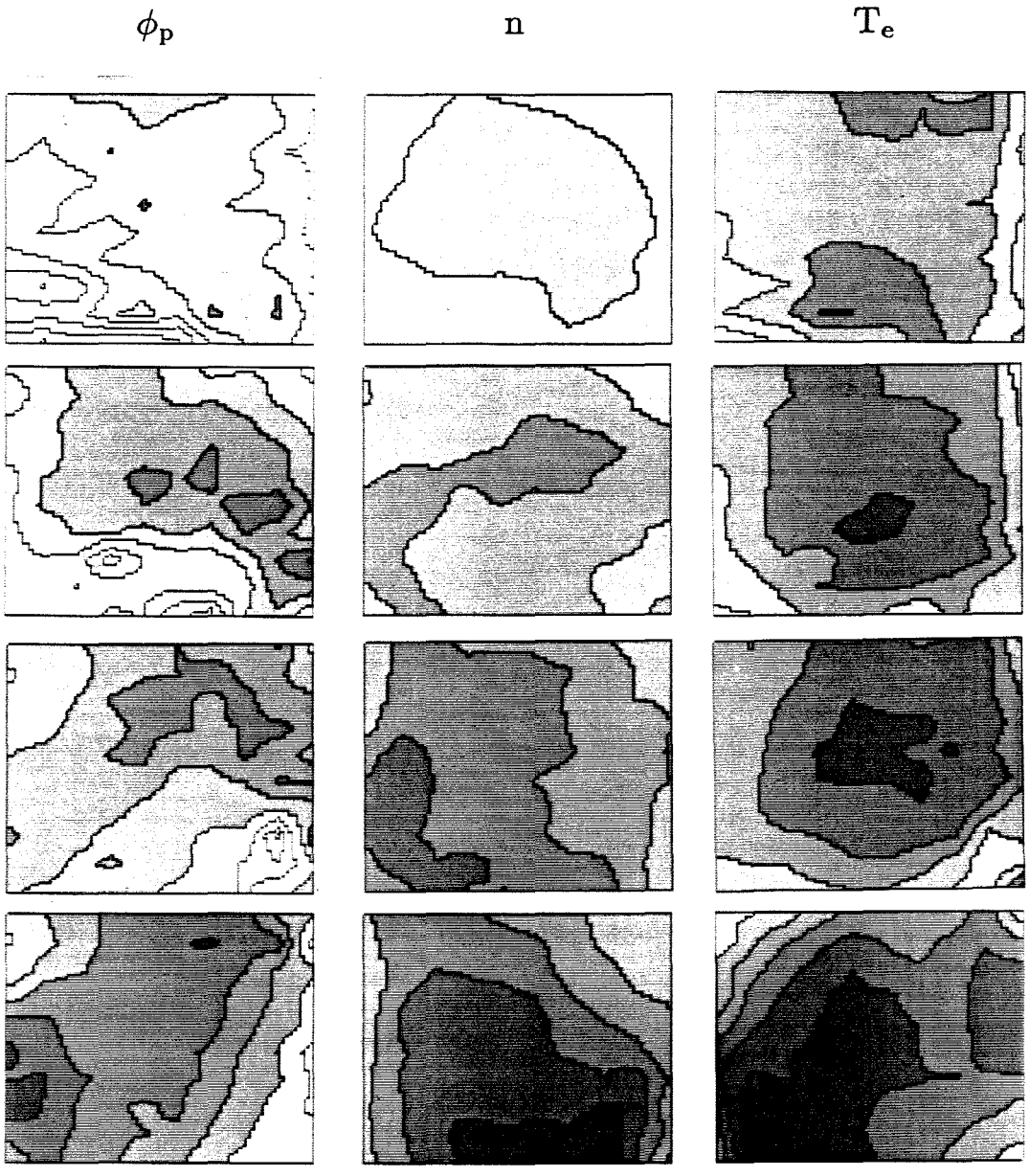

Figure 2.8 : Plasma parameters in a poloidal cross section. Time progresses from the top down in 40μs intervals corresponding to the filled circles in Figure 2.6. B is out of the page so that the electron diamagnetic rotation is counterclockwise. Each image is plotted in a six level linear gray scale progressively darker for larger data values; overscale data is displayed in checks and underscale in white. Full scales for entire series: 15 to 35V for ϕ_p, 0 to $2.9 \times 10^{12} cm^{-3}$ for density, 5 to 15eV for T_e.

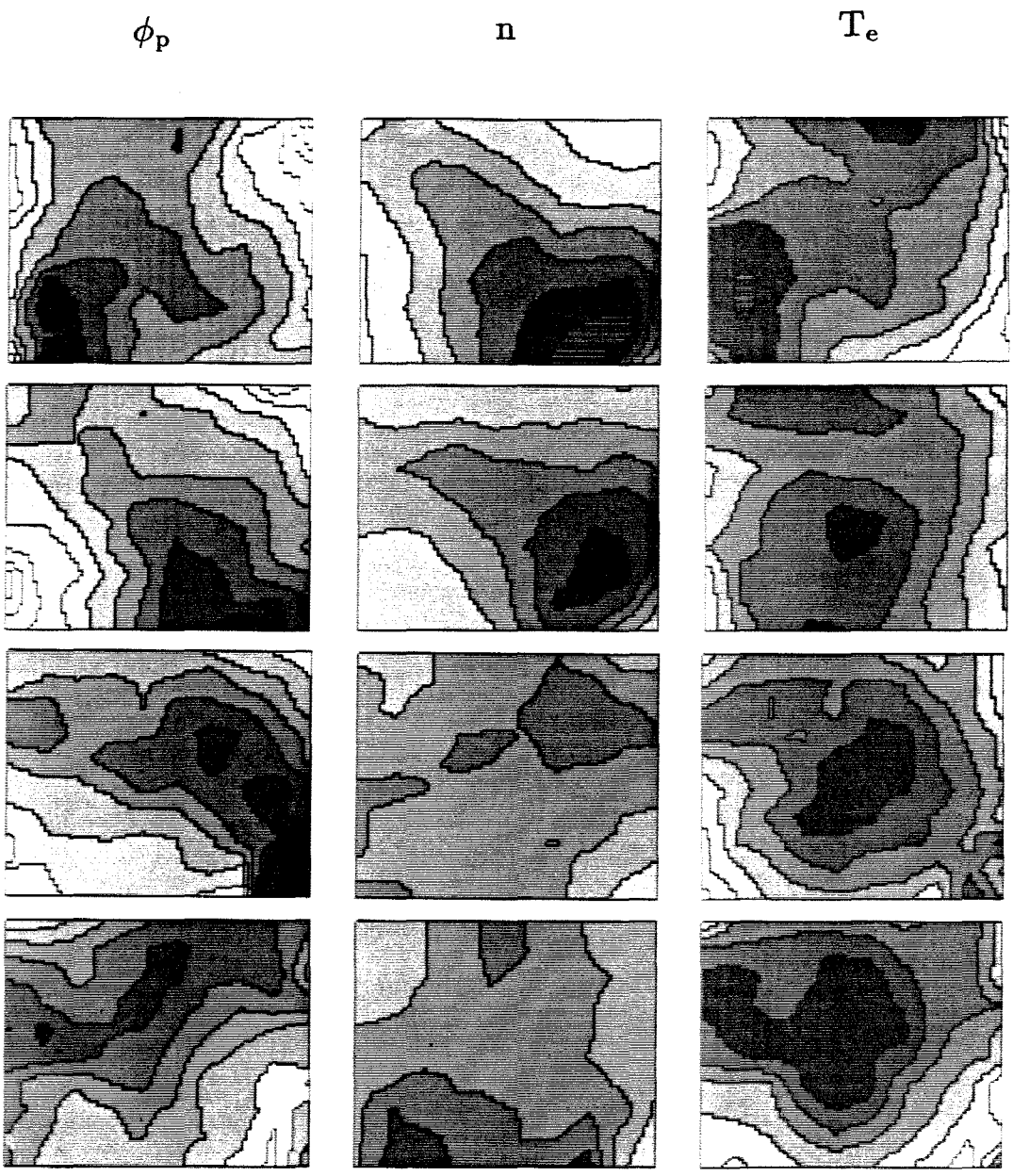

Figure 2.8 (continued): ϕ_p 15 to 35V, n 0 to $2.9 \times 10^{12}\text{cm}^{-3}$, T_e 5 to 15eV.

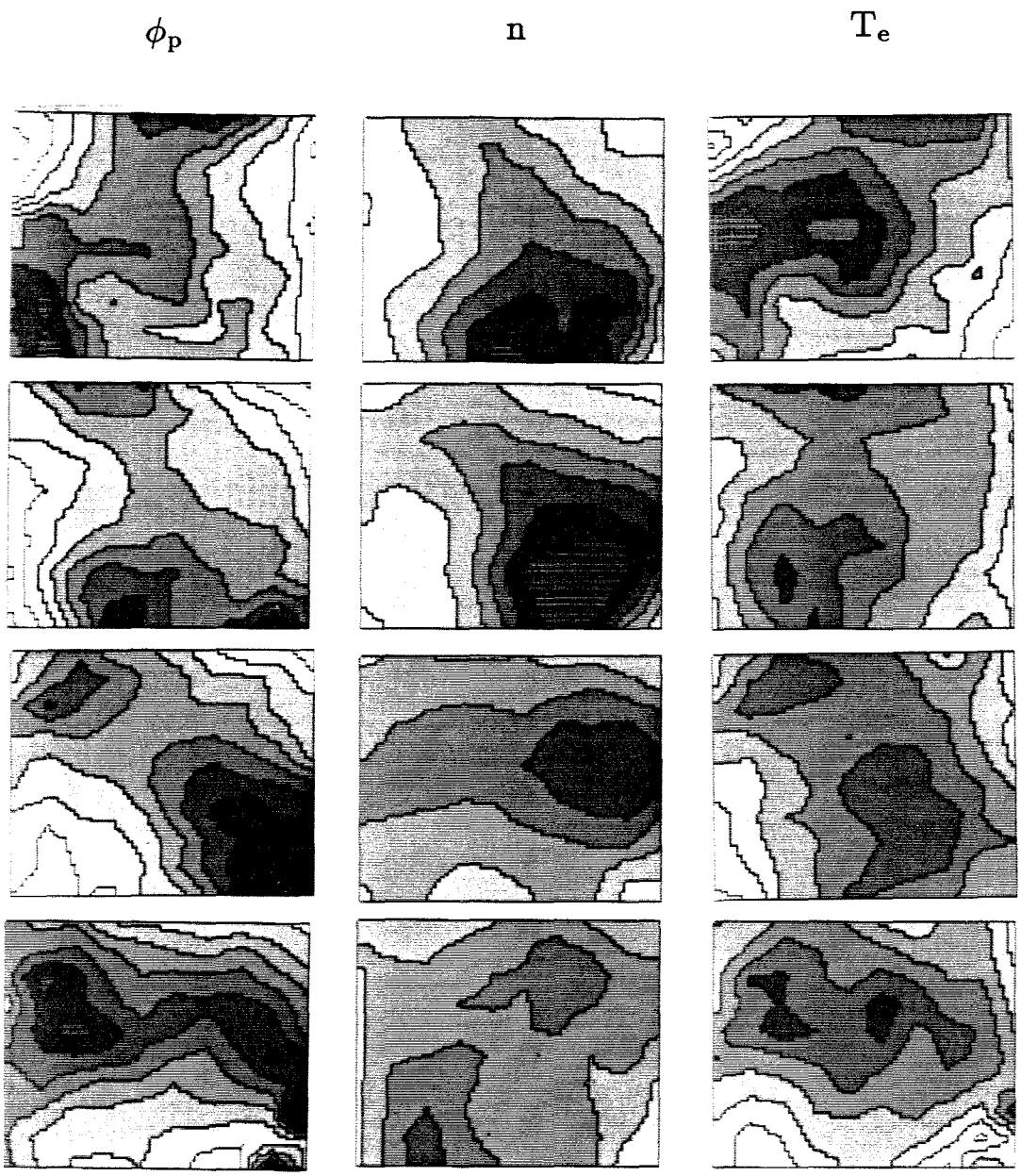

Figure 2.8 (continued) : ϕ_p 15 to 35V, n 0 to $2.9 \times 10^{12}cm^{-3}$, T_e 5 to 15eV.

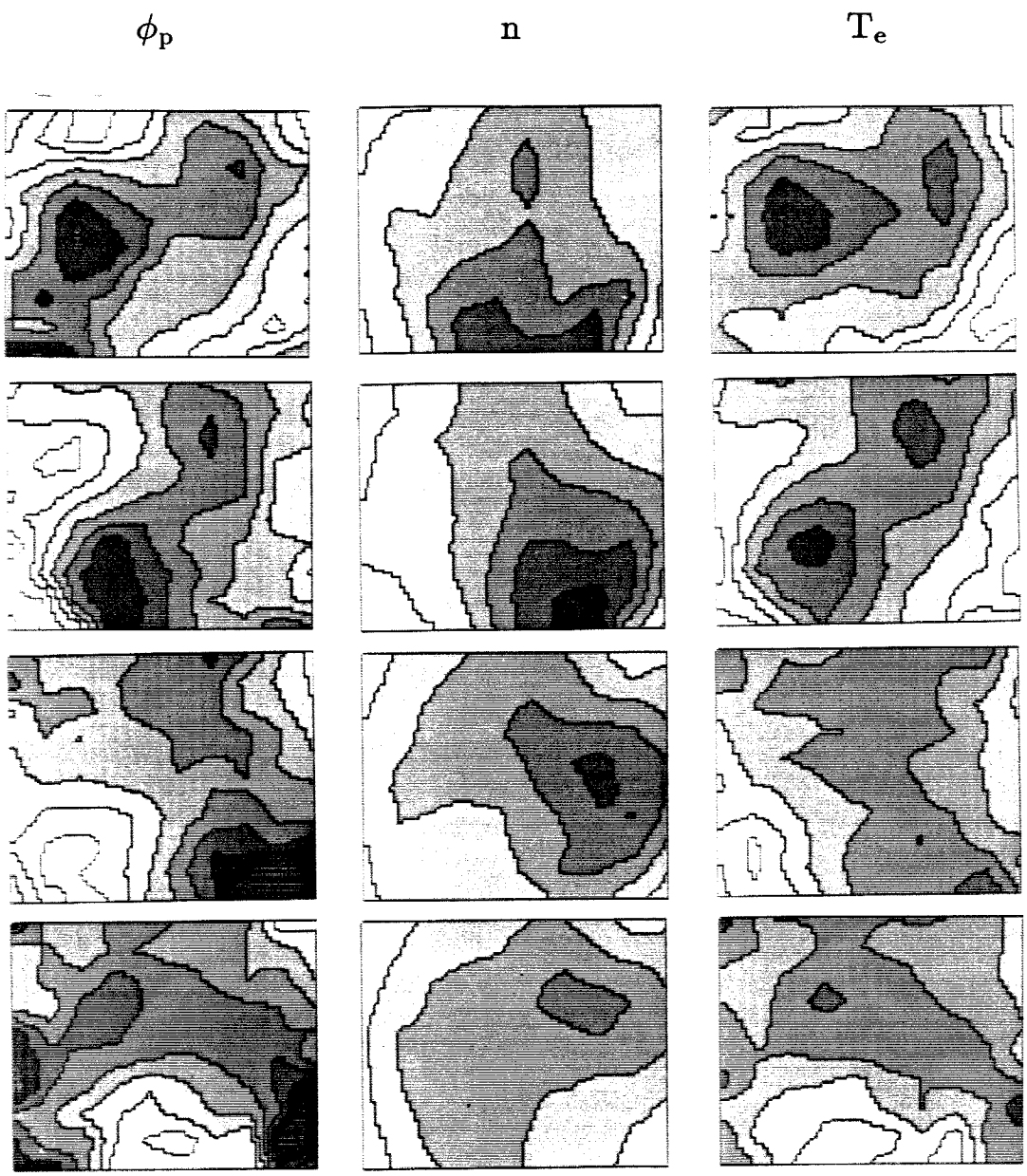

Figure 2.8 (continued): ϕ_p 15 to 35V, n 0 to $2.9 \times 10^{12} cm^{-3}$, T_e 5 to 15eV.

2.2 Stochastic Ion Heating in the Coherent Drift Waves

Ion heating in similar coherent drift waves in Encore has previously been investigated using single point laser induced fluorescence (LIF) (McChesney '85). A number of observations based on experimental data and numerical work showed that the heating was caused by stochastic ion motion in the coherent drift waves. 1) The broadening of the ion distribution function was found to be much faster than can be explained by the usual heating mechanisms, i.e., Ohmic heating, collisional heating, turbulent heating. 2) The strongest heating was observed near the plasma edge where the drift wave amplitude was the largest. 3) Many ions were observed to have energies greater than the electrostatic potential of the wave fields. 4) Poincaré surface of section plots demonstrated stochastic dynamics in the ion equations of motion in simplified wave fields modeling the experiment. 5) A threshold in the peak ion temperature as a function of the normalized wave amplitude in the experiment was reported and qualitatively agreed with the simplified model. 6) A Monte-Carlo calculation of ion trajectories in an electric field with the mode structure observed in the experiment showed that a distribution of ions starting at rest does in fact broaden much faster than predicted by standard mechanisms, in agreement with the experiment (McChesney '91).

The drift wave in Encore is a mostly electrostatic wave propagating in the poloidal direction perpendicular to the dominant toroidal magnetic field. This situation can be simplified to a monochromatic electrostatic plane wave propagating in the $\hat{\mathbf{y}}$ direction perpendicular to a uniform magnetic field in the $\hat{\mathbf{z}}$ direction. The $\hat{\mathbf{x}}$ direction corresponds to the minor radius in the tokamak and points in the direction of $-\nabla \mathrm{n}$ for a drift wave. Using

$$\mathbf{B} = \mathrm{B}\hat{\mathbf{z}}, \qquad \mathbf{E} = \tilde{\phi}\mathrm{k}\sin(\mathrm{ky} - \omega\mathrm{t})\hat{\mathbf{y}}, \tag{2.1}$$

the ion equation of motion

$$m\frac{d\mathbf{v}}{dt} = e(\mathbf{E} + \mathbf{v} \times \mathbf{B}) \tag{2.2}$$

has surprisingly complicated dynamics. The dynamics are in fact stochastic in some regions of phase space for certain field values. These particular wave fields have been studied extensively in connection with particle heating and will be discussed in more detail in Chapter 7. For the parameters in the drift wave in Encore the plausibility of stochastic dynamics can be demonstrated by carefully following the standard methods for solving the Lorentz equation (Eq. 2.2) using the drift approximation.

Focussing on the ion motion perpendicular to the magnetic field, the ion velocity in the drift approximation can be found a number of ways. *Assuming* the ion velocity is the sum of the cyclotron motion and a velocity periodic with the wave frequency and ignoring the particle position appearing in the phase of the wave, the Lorentz equation (Eq. 2.2) can be solved exactly

$$\begin{aligned} v_x &= \frac{\omega_c^2}{(\omega_c^2 - \omega^2)} \frac{k\tilde{\phi}\sin(ky_o - \omega t)}{B} + v_{Lx} \\ v_y &= \frac{-\omega\omega_c}{(\omega_c^2 - \omega^2)} \frac{k\tilde{\phi}\cos(ky_o - \omega t)}{B} + v_{Ly} \end{aligned} \tag{2.3}$$

where y_o is the particle position at $t = 0$, $\omega_c = eB/m$ is the cyclotron angular frequency and $\mathbf{v}_L$ is the Larmor motion which satisfies the homogeneous equation $m d\mathbf{v}_L/dt = e\mathbf{v}_L \times \mathbf{B}$. This solution is clearly well behaved for all times, but it is only a good approximation for the particle motion when $k|y - y_o| \ll 2\pi$.

$$\begin{aligned} k(y - y_o) = k\int_0^t v_y dt \approx \frac{\omega_c^2}{\omega_c^2 - \omega^2}\frac{k^2\tilde{\phi}}{\omega_c B}\left[\sin(ky_o - \omega t) - \sin(ky_o)\right] \\ + \frac{kv_{L\perp}}{\omega_c}\sin(\omega_c t + \delta) \end{aligned} \tag{2.4}$$

where $v_{L\perp}^2 = v_{Ly}^2 + v_{Lx}^2$, $v_{L\perp}/\omega_c = r_L$ the ion gyroradius and δ is the initial gyrophase. Eq. 2.4 shows that the length of time this approximate solution (Eq. 2.3) is valid depends on the particle initial conditions. Using $\omega \ll \omega_c$, taking $\delta = 0$ and defining $\alpha \equiv k^2\tilde{\phi}/\omega_c B$, for small times $\omega t \ll 2\pi$

$$k|y - y_o| \approx \left|\alpha[\frac{\omega^2 t^2}{2}\sin(ky_o) - \omega t\cos(ky_o)] + kv_{L\perp}t\right| \ll 2\pi,$$

implying the approximation is uniformly valid only for times

$$\omega t \ll \frac{2\pi}{\alpha + kv_{L\perp}/\omega}. \tag{2.5}$$

If the right-hand side of Eq. 2.5 is large compared to 2π ($\omega t \not\ll 2\pi$) then the validity criterion must be recalculated. According to the approximation in Eq. 2.4 $k|y - y_o| \leq 2\alpha + kr_L$ for long times. This implies

$$2\alpha + kr_L \ll 2\pi \tag{2.6}$$

must hold for the approximation to be valid. Eq. 2.5 and Eq. 2.6 show that (if kr_L is small) this standard approximation is valid for $\alpha \ll 1$, but may break down for α order unity. If time and space in the equations of motion (Eq. 2.2) in these fields (Eq. 2.1) are normalized to ω_c and k, α is found to be the normalized wave amplitude that controls the appearence of stochasticity. When $\alpha \gtrsim 0.7$ large regions of phase space exhibit stochastic dynamics. The particle orbits become very complicated and non-periodic. α also appears in another approximate solution to the ion motion which displays the breakdown of the drift approximation in a more dramatic way.

For low frequency waves ($\omega \ll \omega_c$) the approximate solutions in Eq. 2.3 are the well known $\mathbf{E}\times\mathbf{B}$ and polarization drifts

$$\mathbf{v}_{\mathbf{E}\times\mathbf{B}} = \frac{\mathbf{E}\times\mathbf{B}}{B^2}, \quad \mathbf{v}_p = \frac{dE/dt}{\omega_c B}.$$

Traditionally the time derivative of the particle position in

$$\frac{dE}{dt} = \tilde{\phi} k \frac{d}{dt} \sin\left(ky(t) - \omega t\right)$$

is ignored when calculating the polarization drift; this is equivalent to assuming $k|y - y_o| \ll 2\pi$. By taking this term into account and solving Eq. 2.2 iteratively

$$\mathbf{v}_p = \frac{\alpha[v_{L\perp} \sin(\omega_c t + \delta) - \frac{\omega}{k}] \cos(ky - \omega t)}{1 - \alpha \cos(ky - \omega t)} \hat{\mathbf{y}} \tag{2.7}$$

where $\alpha = k^2\tilde{\phi}/\omega_c B$ as before. This approximation will diverge when $\alpha \approx 1$ since the denominator in Eq. 2.7 can vanish. Eq. 2.7 also suggests that the particle orbits can not be constructed as a linear superposition of a trajectory with wave periodicity and simple cyclotron motion. These calculations show that standard approximations break down as α increases. This demonstration coupled with the appearence of multiple frequencies in the approximate solution makes the existence of stochastic dynamics in these wave fields less surprising.

No mechanism by which stochasticity *causes* ion heating has been shown explicitly, but plausible arguments based on the phase space 'available' to stochastic ions have been made by many authors (e.g., Smith and Kaufman '75,'78 and Karney '77), backed up by particle simulations (Abe '84) and experimental work (Doveil '81, Skiff '87a, McChesney '87). It is clear that stochastic single particle dynamics play a role in determining macroscopic plasma parameters yet the connection between the single particle dynamics discovered numerically in simple models and the macroscopic parameters measured in real plasmas is not well understood. The fields depend on the particle orbits, but the particle orbits are so complicated that a tractable analytic theory has not yet been developed to explicitly 'integrate' over the stochastic trajectories to predict macroscopic parameters consistent with the stochasticity. A new approach to understanding the effects of

stochastic particle dynamics on macroscopic plasma parameters will be presented in Chapter 7.

This problem is particularly relevant to the uniquely detailed PLIF measurements of the ion fluid velocity field and ion temperatures in the drift waves in Encore. The gross features of the drift waves (ω, $\tilde{n}/n$ and $e\tilde{\phi}/T_e$) obey the two-fluid theory with 'reasonable' simplifications, i.e., T_e is assumed constant and the hot (and fluctuating) ion temperatures are ignored. Yet the parameters of the drift waves in these experiments are such that the ions *in the bulk of the distribution* are expected to have stochastic dynamics. This is confirmed by the large measured ion temperatures. Since there is no theory relating the stochastic dynamics of the ions to the ion fluid velocity, it is unclear what fluid velocity should be *expected.* As will be shown in Chapter 6, the measured fluid flow pattern is well described by a two-fluid approach, but the magnitudes of the predicted velocities are much larger than those measured. The next four chapters detail the PLIF experiment, the measurements and their interpretation.

3

LASER INDUCED FLUORESCENCE TECHNIQUES

3.1 Introduction to Laser Induced Fluorescence

Laser induced fluorescence (LIF) is a powerful technique for measuring the properties of systems of particles with quantum energy levels. It is used on electronic states in molecules, atoms and ions in chemistry (Kinsey '77), fluids (Bechtel '82) and plasmas. The simplest form of LIF may be described using the schematic quantum energy level diagram of a species of interest in Figure 3.1. If the initial population of the upper state is less than that of the lower state a laser in resonance with the $l \rightarrow u$ transition will increase the population of the upper state. The increase in the isotropic spontaneous emission from the decay of the increased upper state population to any final state is laser *induced* fluorescence.

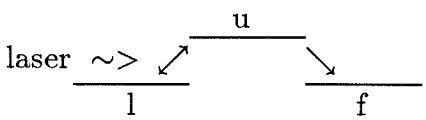

Figure 3.1 : Schematic LIF energy level diagram.

R.W. Wood made the first observation of excited 'resonance radiation' in Na gas (1904) and conducted many subsequent experiments developing the physical principles which would lead to LIF (Wood '34). The earliest experiments on ions in a plasma using 'resonant scattering', a precursor to LIF, were performed in BaII by Hinnov ('63) and Hoffman ('64). With the advent of the laser, 'selective excitation spectroscopy' was proposed as a plasma diagnostic by Measures ('68). A number of techniques and possible applications of LIF in plasmas were explored conceptually by Measures ('68) and Dimock ('69). Burrell and Kunze ('72) first demonstrated LIF in a plasma on He neutrals. Stern and Johnson ('75) were the

first to successfully demonstrate LIF on the ions of a plasma, using it to measure the velocity distribution of ArII ions in a hot-cathode dc discharge.

If a suitable species exists in the plasma, LIF is an ideal plasma diagnostic. An LIF measurement does not perturb the plasma and still has excellent spatial, velocity and temporal resolution for the fluorescing species. The cross section for resonant absorption $\sim 10^{-11}\text{cm}^2$ is typically 10-14 orders of magnitude larger than cross sections for other (often nonresonant) laser interactions such as Thomson scattering. The usual geometry for detection is displayed in Figure 3.2. The exciting laser beam and the optic axis of the detector are at right angles. The diagnosed volume is the intersection of the laser inducing the fluorescence and the solid angle subtended by collection optics. Usually the LIF is detected at a wavelength different from that of the exciting laser line so scattered laser light can be easily filtered out before reaching a detector.

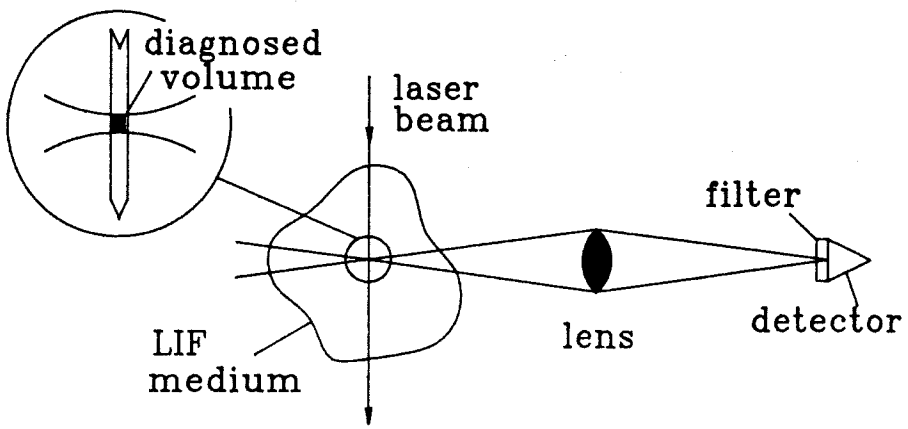

Figure 3.2 : Typical geometry for single point LIF.

Interpreting LIF signals in terms of plasma parameters may be an involved process. The intensity of the LIF can depend on the laser intensity, linewidth or pulse length, the physical constants of the transitions as well as the local plasma conditions. However, if an experiment is arranged so the LIF intensity depends strongly on only one plasma parameter, interpretation is often straightforward. The neutral density (Burakov '77), impurity density (Meng '79, Schweer '80), majority ion density and temperature (Stern '75, '76), electron density (Chall '85), local magnetic field (Stern '85), local electric field (Moore '84) and ion trajectories (Stern '83) have all been measured with variations on the basic LIF technique presented above. The sophistication of LIF techniques and the number of parameters measured continues to increase (Skiff '87b, McWilliams '90, Bowles '92). LIF techniques can be categorized in three groups following the chronological development and increasing complexity of LIF as a plasma diagnostic.

Broad laser linewidth excited LIF

The linewidths of most lasers available to early plasma LIF experimentalists were much greater than the plasma ion absorption linewidths. In considering techniques for early LIF experiments Measures ('68) derived an expression relating LIF intensity from two transitions to local values of the electron temperature and density. Dimock ('69) pointed out that, for sufficient laser intensity, a broad linewidth laser centered on an allowed transition essentially holds the two populations in balance and the LIF signal will depend only on the pumped species density. Many plasma experiments used broad linewidth excited LIF to measure species densities in just this way, e.g., ArII (Stern '75), BaII (Stern '76), HI (Burakov '77), AlI (Meng '79) and FeI (Schweer '80).

The spectrum of the fluorescence *emitted* from many plasmas is dominated by Doppler broadening due to the velocity distribution of the emitting particles. In

these cases, the temperature of the fluorescing species can be determined (Stern '76) by measuring the linewidth of the emitted light using standard spectroscopic techniques, e.g., a scanning monochrometer or Fabry-Perot etalon. A technique using narrow linewidth tunable dye lasers to scan the *absorption* line has made this technique less common.

Another interesting broadband excited LIF technique was used by Chall ('85) to measure the local electron density n_e in a hollow-cathode arc. The LIF from a pulsed laser was detected with fast time resolution (2.4 ns). The decay times of the LIF were related to the local value of n_e via a collisional deexcitation model.

Narrow laser linewidth excited LIF

A number of LIF techniques requiring a tunable laser with a linewidth much narrower that the absorption linewidth were proposed before such lasers were readily available. Measures ('68) discussed using a single mode tunable laser to detect the mean drift velocity of a flow field via the Doppler shifted absorption peak. Dimock ('69) first proposed scanning a narrow linewidth laser through the Doppler broadened absorption profile to measure the one-dimensional velocity distribution f(v) of the particles. The temperature of impurity FeI was measured using the latter LIF technique in the ISX-B tokamak by Schweer ('80). Stern ('81) measured not only the bulk ion temperature, but also ion beam features of f(v) coherent with an electrostatic ion cyclotron wave (EICW) in a BaII Q-machine plasma. Stochastic heating of ArII in an EICW with a neutralized ion Berstein wave (NIBW) (Skiff '87a) and in a coherent drift wave (McChesney '87) have also been studied using this LIF technique.

Other line broadening mechanisms may complicate LIF measurements of one quantity, yet allow the measurement of another. Magnetic fields may be measured from Zeeman splitting of resonance lines. Electric fields in some plasmas may be

measured from Stark broadening of resonance lines although Stark broadening due to collisions is negligible in many basic plasma physics experiments. Mean fields needed for dominant Stark broadening are extremely high, but electric fields as small as 40 V/cm have been measured using Stark mixing of parity levels in BCl (Moore '84).

Detailed examination of f(v) can lead to precise measurements of parameters difficult to measure with traditional methods. Skiff ('87b) measured simultaneously a component of the electric field amplitude $\geq$1V/cm and a perpendicular wave number of a NIBW in ArII by analyzing a coherent modulation of the perturbed velocity distribution. The ion fluid velocity is another basic plasma parameter that is rarely measured. This thesis describes spatially and temporally resolved two-dimensional imaging of one component of the ion fluid velocity field using LIF techniques.

Multiple Beam Techniques

Optical tagging is currently one of the more sophisticated LIF techniques. Though a rudimentary tagging scheme for measuring temperature was proposed by Dimock ('69), Stern ('83) described and demonstrated optical tagging with clear emphasis on the powerful general nature of the technique. It offers the ability to *tag* a selected group of particles in a small volume of phase space and follow their evolution in the total phase space. The tagging is localized spatially by the laser dimensions and can also be localized in velocity space by the laser linewidth (for more details see Appendix B).

Since Stern's ('83) initial measurements, optical tagging has been used in a number of Q-machine BaII plasma experiments studying cross-field ion transport and heating (McWilliams '83, '87, '90), chaotic particle dynamics (Skiff '88, Fasoli '93) and ion phase space trajectories (Fasoli '89). The first attempts at tagging in

an ArII plasma were limited by the lifetimes of the tagged particles (McChesney '91).

3.2 Planar Laser Induced Fluorescence

An obvious extension of single point LIF is *planar* laser induced fluorescence (PLIF); a two-dimensional array of points within a plasma is diagnosed simultaneously (see Figure 3.3). PLIF has been an important diagnostic tool in the study of fluids for many years (Kychakoff '82,'84, Dyer '82), especially NO and OH in flames, yet PLIF has not been used as a plasma diagnostic until now. The first PLIF system for use on the ions in a plasma has been developed for the Ar plasma discharges in Caltech's Encore tokamak and is the subject of this thesis.

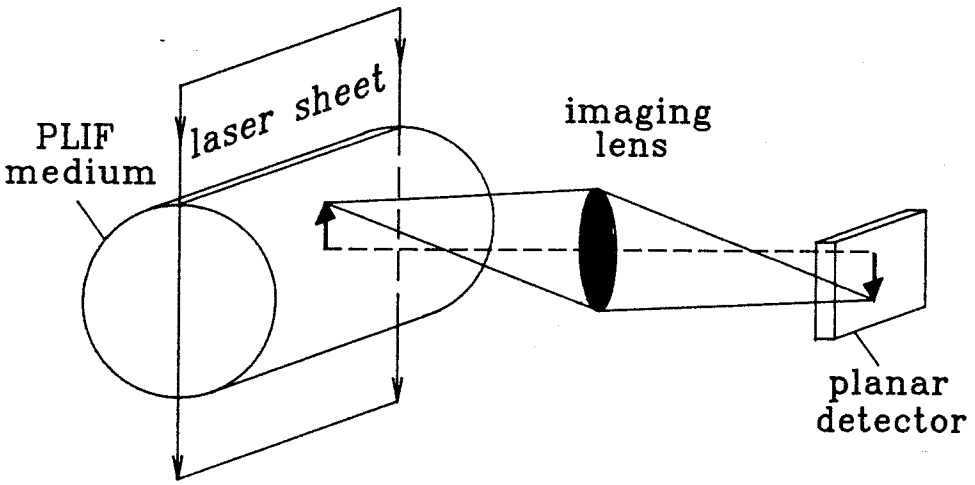

Figure 3.3 : Ideal geometry for a PLIF experiment.

In addition to expanding the LIF techniques available for plasma physics experiments, the development of plasma PLIF was motivated by the exciting opportunities for nonperturbing measurements of plasma ion parameters over large

plasma areas with precise spatial, velocity and temporal resolution. The possibilities for new and unique measurements of plasma ions may be attainable with relatively straightforward data analysis and interpretation. PLIF (and LIF) experiments usually require only *known* spectroscopic information to interpret raw data as opposed to inversion of chord averaged measurements based on plasma *models* which may be complicated, iterative or based on assumptions difficult to verify.

All of the LIF techniques described in the last section may be used directly in PLIF experiments designed to *image* plasma ion properties. Exciting PLIF with a broad linewidth laser could provide nonintrusive ion density images. Of particular interest is the possibility of imaging the ion density in waves or turbulence on very short time scales compared with the time scales of the plasma phenomena. Two-dimensional, time resolved images of ion density could stimulate new insight into the physics of turbulent plasmas as fluid visualization has in fluid dynamics (Dahm '90). PLIF would simultaneously provide the *quantitative* data base with which to test hypotheses suggested by any new ideas.

Other possible experiments include using one spatial dimension of an imaging detector as a spectral axis which may provide a means to measure virtually instantaneous ion distribution functions while still retaining spatial resolution in one direction. Since tagging has not been used in fluids and PLIF is new to plasmas, the possibilities for planar tagging experiments can also be explored. This thesis describes time resolved two-dimensional images of a component of the ion fluid velocity field and images of the ion temperature field in a wave.

An extremely important, but rather prosaic advantage of the PLIF system is accelerated data acquisition. Even at the high repetition rate of the Encore tokamak (15 Hz), the raw PLIF data used for figures in this thesis took a number

of hours to compile. Although it is conceivable that single point LIF could have been used to take the same data, practically speaking it is the PLIF diagnostic which made the measurements possible. Ignoring the time required to change the position of a single detector, the optics and a laser beam, single point LIF measurements would take hundreds of hours of continuous data acquisition to reproduce the data from a single PLIF experimental run.

A system with such high data rates also gives the experimentalist the flexibility to make many measurements in a particular plasma or in different plasmas in a reasonable time. Since the raw PLIF data is straightforward to interpret, this rapid data acquisition is accompanied by rapid data analysis and display. This allows the experimentalist to make many observations of the plasma without a predetermined observational goal, but with an eye to discover or observe new phenomena.

4

LASER INDUCED FLUORESCENCE IN ENCORE

4.1 Introduction

The PLIF measurements described in this thesis were made during Ar plasma discharges in Caltech's Encore tokamak. Electron collisions excite some fraction of the ions to ArII metastable states suitable for optical LIF. One of the motivations to develop the PLIF diagnostic was to make quantitative single shot images of the plasma ion density using broad laser linewidth excited PLIF. The feasibility of such an experiment depends on three important issues: the ratio of the metastable population to the mean ion density, the relationship between the induced fluorescence and the metastable density and the ability to detect the fluorescence. In an ideal situation, the metastable population would be linearly related to the total ion density, the PLIF would be linearly related to the metastable population and the detector would produce an easily measurable signal linearly proportional to the PLIF with the same proportionality for each image element. Unfortunately, the PLIF experiment on the Encore plasma is far from this ideal.

The metastable population depends in a very nonlinear way on the plasma parameters. A simple model for the metastable population is outlined in Section 4.2. It is found that the relative metastable population depends most strongly on the electron temperature and density for parameter regimes in Encore discharges. Because these parameters fluctuate in the drift waves in Encore (see Chapter 2), the metastable ion population is not a good measure of the total ion density.

Despite this drawback, it is still important to understand the relationships between the LIF signal, laser parameters and the metastable population. The results of a semi-classical model relating the LIF signal to the metastable density are

presented in Section 4.3. It is found that the existing broad linewidth operational mode of the PLIF laser system is sufficient to make simple broad linewidth density measurements only in discharges when the ion temperatures are very low. The effect of power broadening in scanning narrow laser linewidth temperature measurements is also discussed. Within the limits of the two calculations, the results are combined to estimate the expected LIF signal and compared to a single point LIF measurement using a single photomultiplier.

4.2 ArII Metastable State Population

LIF requires a population of particles with a specialized quantum energy level structure. The lower state must be highly populated and connected to an upper state by an allowed transition (ideally accessible by a tunable dye laser line). In an ArII plasma the highly populated 3p ground state is separated from the other ionic states by more than 15 eV (see Figure 4.1). Fortunately ArII has seven metastable states in the 3d level (Luyken '72) which are expected to have relatively large populations in the plasma. Six of the metastable states have clear LIF schemes which are all considered in detail in Appendix B. Although most of the schemes have not previously been proposed or used, they may prove useful in future experiments. Figure 4.2 shows those which have previously been used in experiments. The $3d'\,^2G_{9/2} \rightarrow 4p'\,^2F^o_{7/2} \rightarrow 4s'\,^2D_{5/2}$ scheme was used for the experiments described in this thesis.

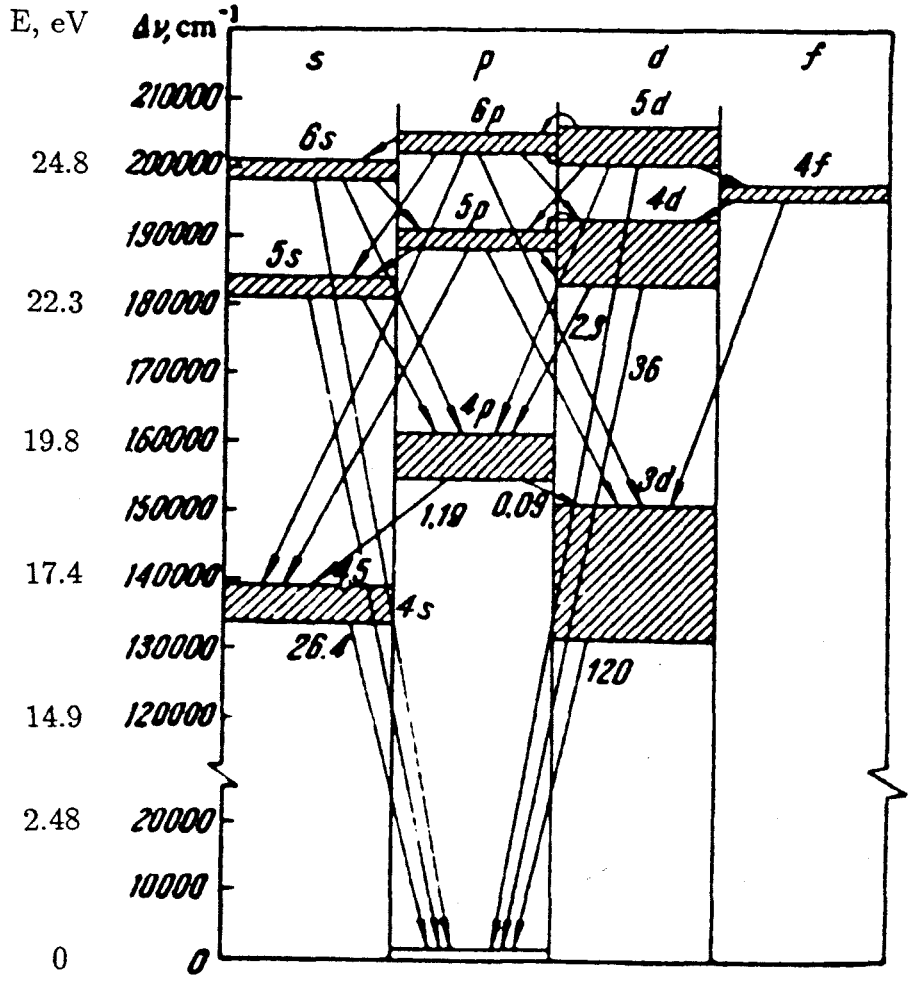

Figure 4.1 : Electronic configuration of the ArII ion. The numbers at the arrows designate the radiative probabilities of the transitions in units of $10^8 \mathrm{sec}^{-1}$ (Kitaeva '70).

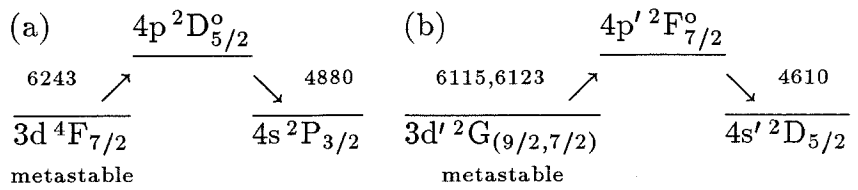

Figure 4.2 : Three LIF schemes pumped from ArII metastable states. Wavelengths given in Å. (a) Watanabe ('87) (b) Rosner ('76), McChesney ('87).

Since an LIF measurement of the metastable density is straightforward, it is desirable to relate the metastable density to other parameters more useful in characterizing the plasma. If the ratio between the metastable density and the total Ar ion density remained constant in a plasma, the metastable density could be directly interpreted as the plasma ion density. A model predicting the metastable density is developed in Appendix C to test this hypothesis.

The dominant metastable production and quenching reactions in Encore are identified by considering the approximate rates for a number of reactions involving the metastables. It is found that electron impact ionization of neutral Ar and electron collisional excitation of Ar ions are the dominant sources of the metastables in Encore. Electron collisional de-excitation is combined with an ad hoc wall recombination term to model the metastable quenching. A set of equilibrium equations are derived and solved analytically to give the metastable ion, non-metastable ion and neutral Ar densities in terms of the the electron density n_e and the relevant cross sections averaged over a Maxwellian electron distribution with a specified temperature T_e. The wall recombination time is taken to be $\tau = 100\mu s \approx c_s/a$ (where $c_s = (T_e/m_i)^{1/2}$ is the ion acoustic velocity and a is the minor radius).

The results of the model for two cases relevant to the Encore discharges are shown in Figure 4.3. The metastable ratio predicted by the model is very sensitive to changes in T_e and n_e. Since both T_e and n_e have large oscillations in the drift

waves in Encore, a measurement of the metastable population cannot be directly interpreted in terms of a single plasma parameter. Figure 4.4 shows the results of the model using Langmuir probe measurements of T_e and n_e to calculate the metastable density for a single point in the plasma during the discharge. The calculations predict the metastable density fluctuations should be dominated by fluctuations in T_e. This prediction can be compared to the metastable density actually measured using PLIF in the same discharge (see Figure 4.4). The model and the measurements do not agree on the relative phase of the metastable oscillations during most of the discharge. Effects due to the precise electron distribution or processes ignored in this model must play an important role in determining the metastable density in Encore. Due to these considerations, metastable density measurements cannot be directly interpreted in terms of other plasma parameters at this time. Although a more detailed model may be developed, it appears that *measurements* of the primary plasma parameters are required *before* a metastable density measurement can be interpreted.

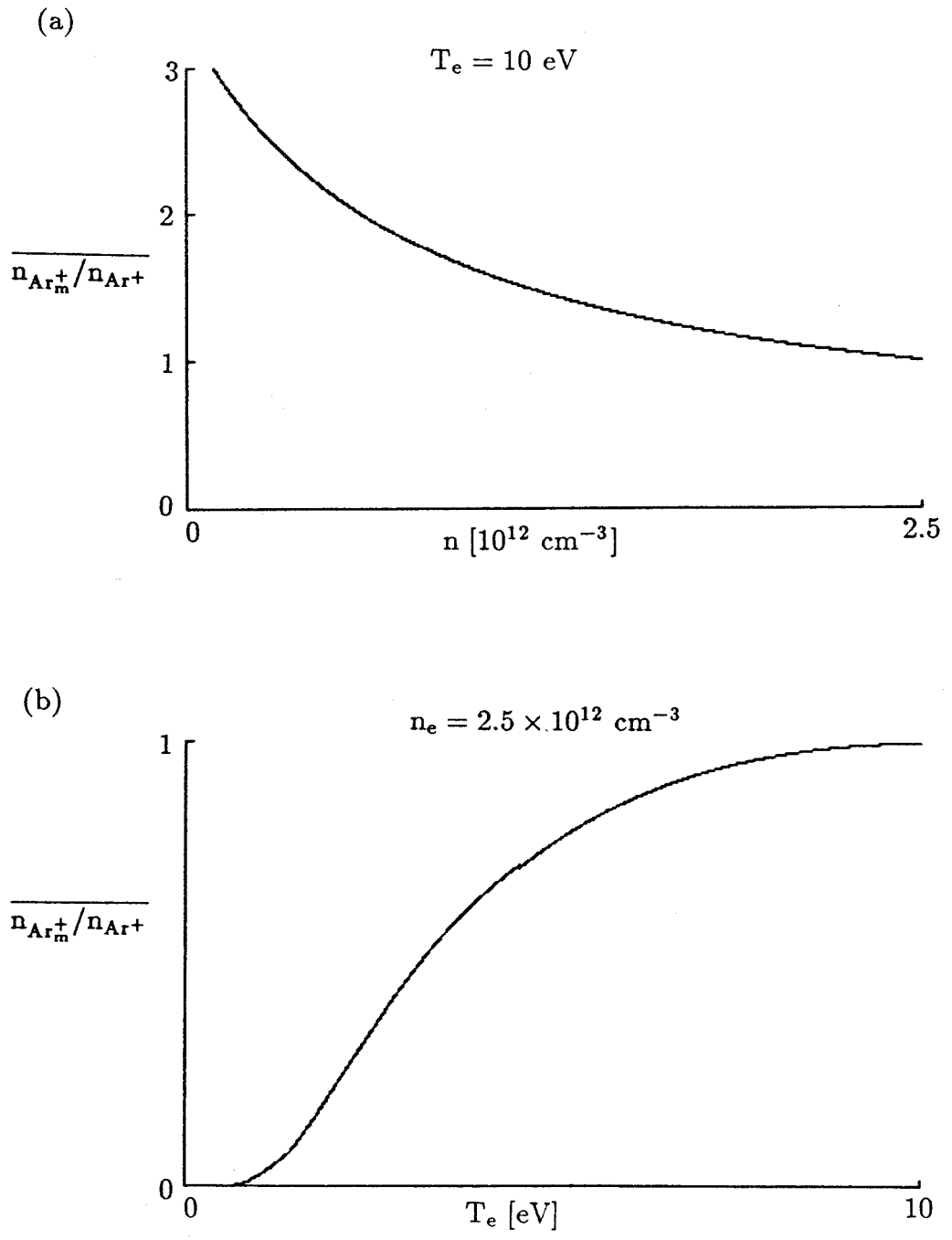

Figure 4.3 : Calculated ratio of metastable to majority ions normalized to 2.6 × 10^{-3}. (a) The ratio as a function of n_e with $T_e = 10$eV. (b) The ratio as a function of T_e with $n_e = 2.5 \times 10^{12}$ cm^{-3}.

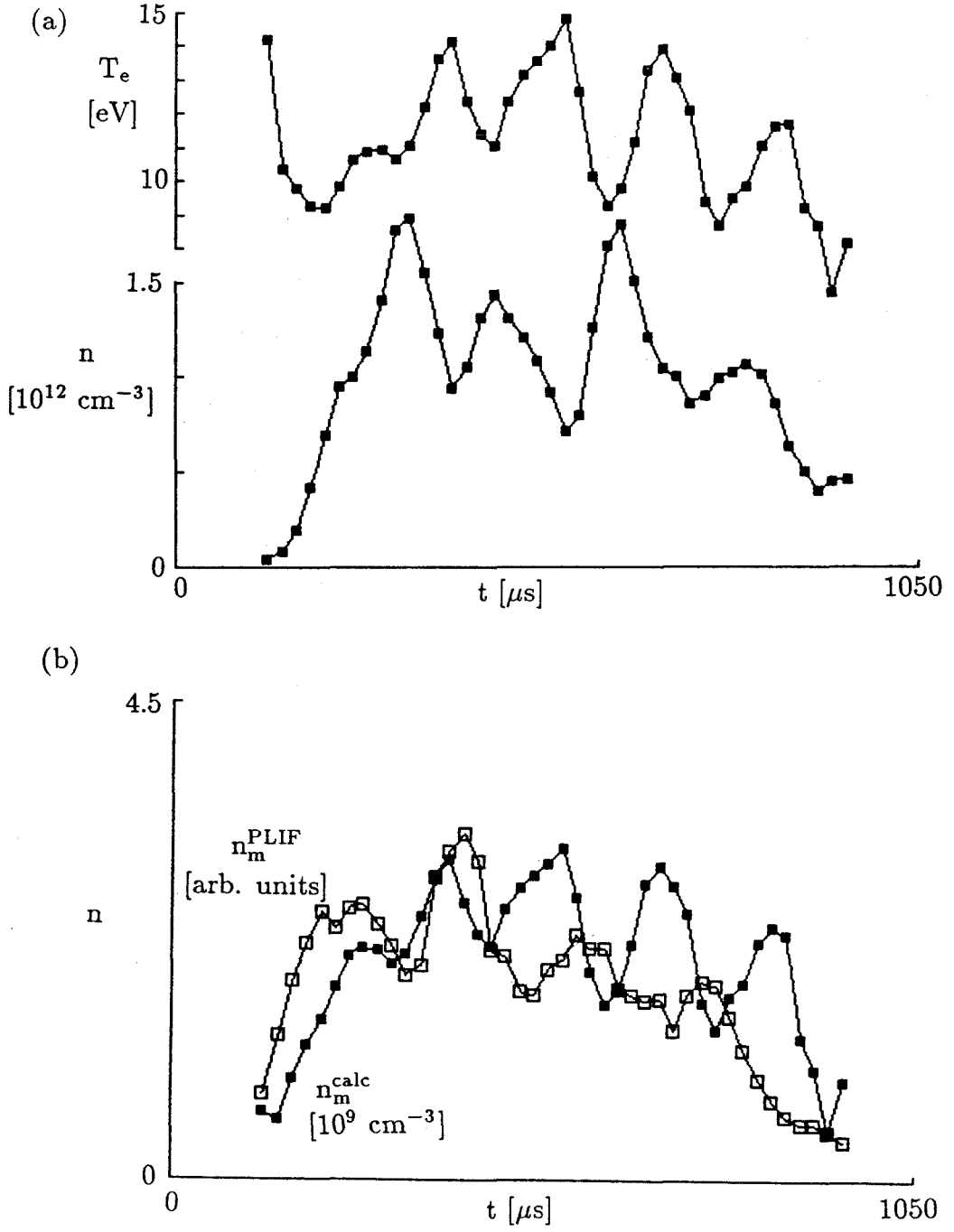

Figure 4.4 : Comparison of the calculated and measured metastable ion densities. (a) Probe measured electron temperature and plasma density used to calculate the metastable density. (b) Metastable density during the discharge. Filled squares are calculated from the model; the open squares are PLIF measured values.

4.3 LIF Signal Calculation

Ideally the LIF signals in an experiment are proportional to the pumped metastable density. Due to the Doppler broadened absorption line in Encore, only certain velocity classes of the metastables interact with the laser. Since optical wavelengths are related to particle velocities via the Doppler shift $v/c = \Delta\lambda/\lambda_o$, there are two extreme cases which make LIF measurements easily interpreted. The laser linewidth could be either extremely narrow *or* extremely broad compared to the width of the velocity distribution. In the broad laser linewidth case, the LIF signal would be proportional to the *total* density of the pumped state. The LIF signal in the narrow linewidth case would be proportional to the *resonant* ions, only those with the velocity resonant with the laser. LIF data in the narrow laser linewidth case can be directly interpreted as values of the ion velocity distribution function.

In fact, the LIF signal depends on other parameters including the intensity and pulse length of the laser. Since the laser has a finite linewidth, the proportionality between LIF signal and density for different velocity classes will vary. The total LIF signal will be a weighted average of the signal due to particles in many velocity classes. If the laser linewidth is of the order of the Doppler broadening, different density measurements (in space or time) will not be comparable if the distribution varies between measurements. Likewise, if a narrow linewidth laser is centered on a given velocity class, the LIF may not be dominated by signal from that class if the LIF due to the wings of the laser line are significant.

A semi-classical model for the interaction of light with a resonant electronic transition is described in detail in Appendix D. The model gives quantitative expression to the physical arguments above. Spatial uniformity of the laser and

plasma is assumed and only the three states of the PLIF scheme used for this experiment are considered (see Figure 4.5).

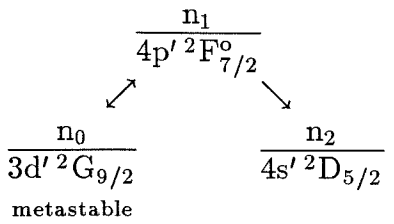

Figure 4.5 : ArII LIF scheme with notation for the semi-classical model.

The model is based on the standard rate equations describing the state populations as a function of the ion speed parallel to the laser propagation vector and time $n_i(v,t)$.

$$\dot{n}_0 = -(\frac{1}{\tau_0} + B_{01}\Phi)n_0 + (A_{10} + B_{10}\Phi)n_1$$

$$\dot{n}_1 = B_{01}\Phi n_0 - (\tau_1^{-1} + B_{10}\Phi)n_1$$

A_{10}, B_{01} and B_{10} are the Einstein coefficients in terms of intensity for the transition with resonant frequency f_0; τ_0 and τ_1 are the radiative lifetimes of the states and

$$\Phi(v,t) \equiv \int_{-\infty}^{+\infty} I(f,t)\, g(v,f)\, df$$

is the effective intensity of the laser radiation for a class of particles with speed v taking into account the Doppler shifted homogeneous absorption lineshape $g(v,f)$ and the laser intensity linewidth $I(f,t)$. The equations are solved in matrix form for each velocity class. An analytic expression for the number of LIF photons emitted per volume $N_{h\nu}$ for a laser pulse is derived. The necessary integrals are calculated numerically assuming the upper state population is initially zero, a step function laser pulse with a Gaussian frequency lineshape and homogeneous Maxwellian velocity distributions.

The LIF signal is directly proportional to $N_{h\nu}$. $N_{h\nu}$ can be expressed as the product of the pumped state density n_0 and a factor Υ which contains the dependence of the signal on atomic parameters and the laser: $N_{h\nu} = \Upsilon n_0$. In an experiment designed to make single shot ion density measurements, the LIF signal should depend only on the metastable ion density; Υ should be constant for the plasma and laser parameters expected in the experiment. The current laser system can be operated in either a narrow or broad linewidth mode; $\Delta f_L = 1.5$ GHz or $\Delta f_L = 6$ GHz respectively. Figure 4.6 shows Υ calculated for different linewidth lasers centered on the absorption line as a function of the ion temperature T_i and laser pulse energy E_{las}.

For all laser energies in the $\Delta f_L = 1.5$ and 6GHz cases, Υ (and thus the LIF signal) is a strong function of T_i in the parameter regime expected in Encore. Therefore, the currently available laser linewidths cannot be used to make reliable single shot metastable density measurements in Encore unless it is known that the distribution function does not change between measurement sites or times. Figure 4.6 also displays the $\Delta f_L = 25$GHz case which is broad enough to eliminate variations in signal due to likely Encore parameter fluctuations as well as laser energy variations for $E_{las} > 50\mu$J/pulse. Possiblities for broadening the existing laser line are discussed in Chapter 5.

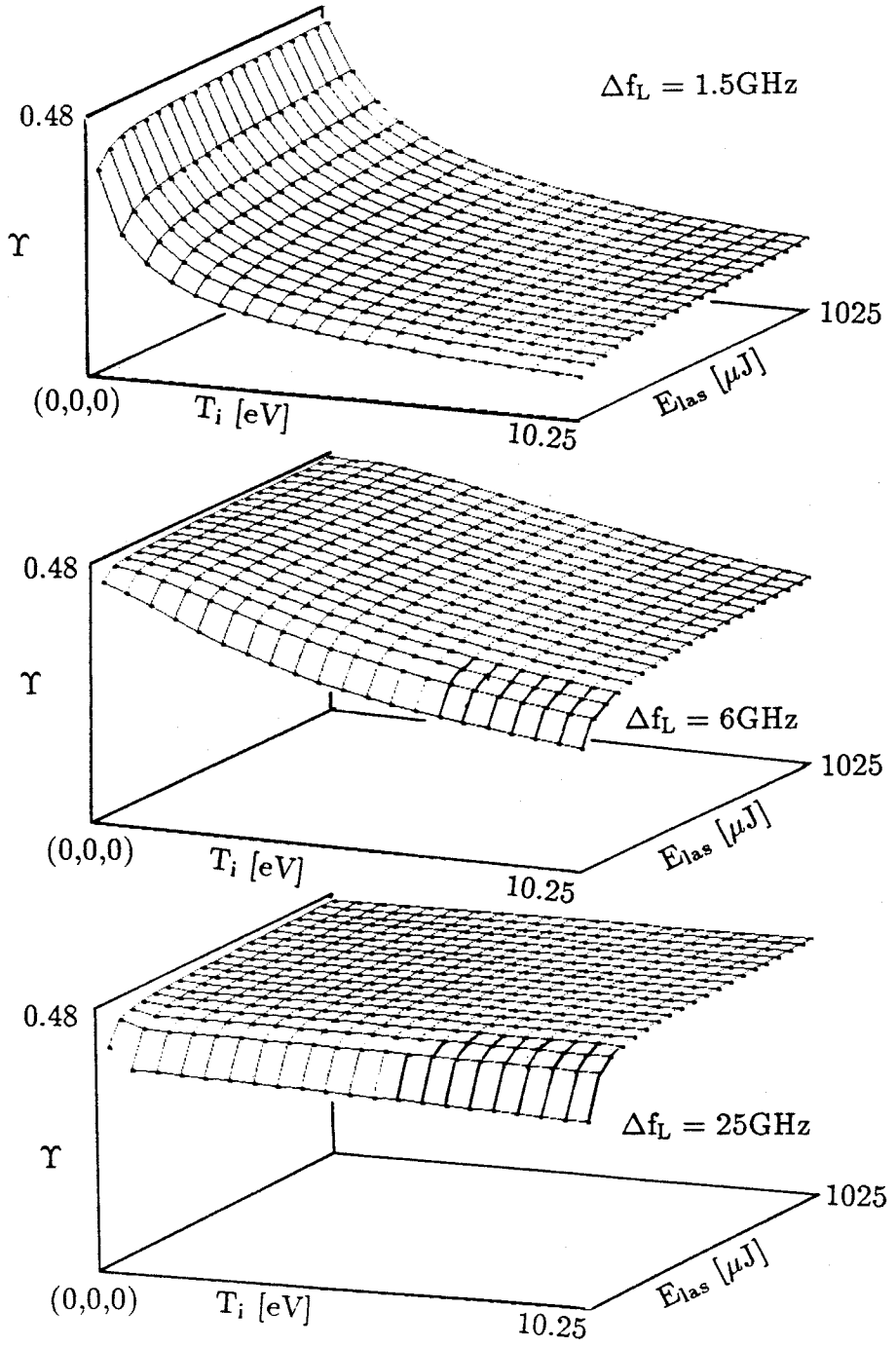

Figure 4.6 : Calculated Υ for three laser linewidths centered on the Doppler broadened ion absorption line as a function of ion temperature (0.5 eV steps) and laser energy (50μJ steps, t_{las} = 15ns, laser area 0.00015m^2). For constant metastable density the LIF signal $N_{h\nu} = \Upsilon n_0$ is proportional to Υ.

Ion velocity distributions are deduced by *scanning* the wavelength of the narrow linewidth laser through the Doppler broadened absorption line, measuring the resulting PLIF signals and χ^2 fitting the signals to a Maxwellian. Figure 4.6 shows that higher laser energies increase the LIF signal until a saturation value is reached. As the pulse energy is increased from zero, more of the metastable population is pumped into the upper state increasing the LIF signal. Saturation occurs if the laser energy becomes large enough that ratio of the metastable and upper state populations is the ratio of the statistical weights of the states; absorption and stimulated emission balance. Some of the upper state population is still lost via LIF to states other than the metastable, but this rate cannot be increased.

Larger LIF signals make detection easier, but the increased laser energy increases the importance of the wings of the laser line. This is a problem when it is assumed that the PLIF signal is proportional to the density of ions in resonance with the *center* of the laser line. Figure 4.7(a) shows how LIF measurements with a high intensity laser centered in the wings of the *distribution* actually reflect the ion density nearer the center of the distribution. If such measurements are used directly, the measured distribution is broader than the true distribution (see Figure 4.7(b)). This is called power broadening. It is important to note that a power broadened measurement is *not* shifted from the true velocity distribution.

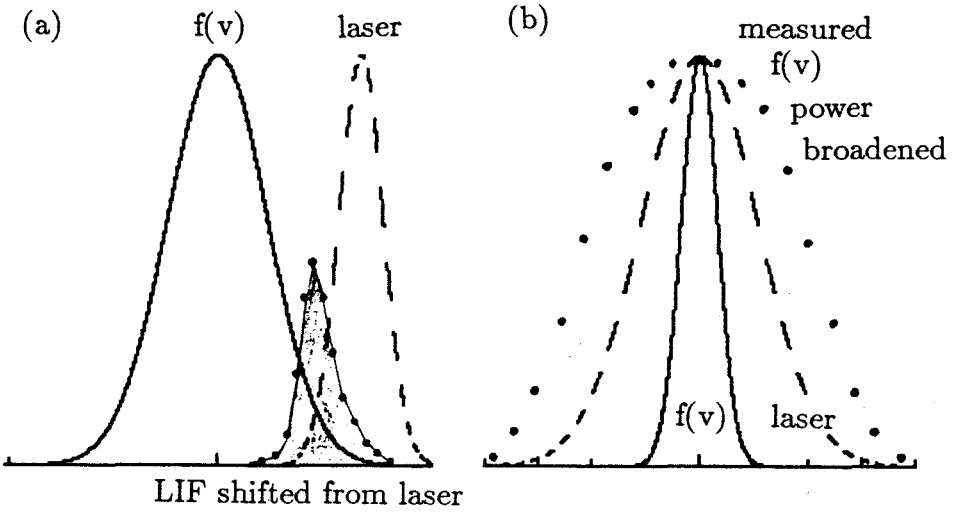

Figure 4.7 : Illustrations of the effects of power broadening. The solid lines indicate the true velocity distribution; the dashed lines indicate the laser line. (a) For a single LIF measurement the peak in the LIF signal (the dots around the shaded region) is representative of the ions with lower speeds than those in resonance with center laser line. (b) If the LIF signal is interpreted as the population of ions with a velocity in resonance with the center of the laser line (the dots), the LIF determined distribution is power broadened compared to the actual velocity distribution.

Figure 4.8 shows the calculated errors in an LIF measured temperature as a function of the actual ion temperature and laser energy. For typical laser energies in this experiment ($\lesssim 300\mu$J/pulse) the temperature error is < 0.2. Since the error is *always* overestimation, the PLIF measurements of the lowest temperatures are upperbounds on those temperatures and a check that the higher temperatures are not significantly power broadened. In this experiment temperatures as low as 1 eV were measured. The uncertainty due to power broadening is less than other uncertainties in the experiment, predominantly from shot-to-shot reproducibility of the plasma.

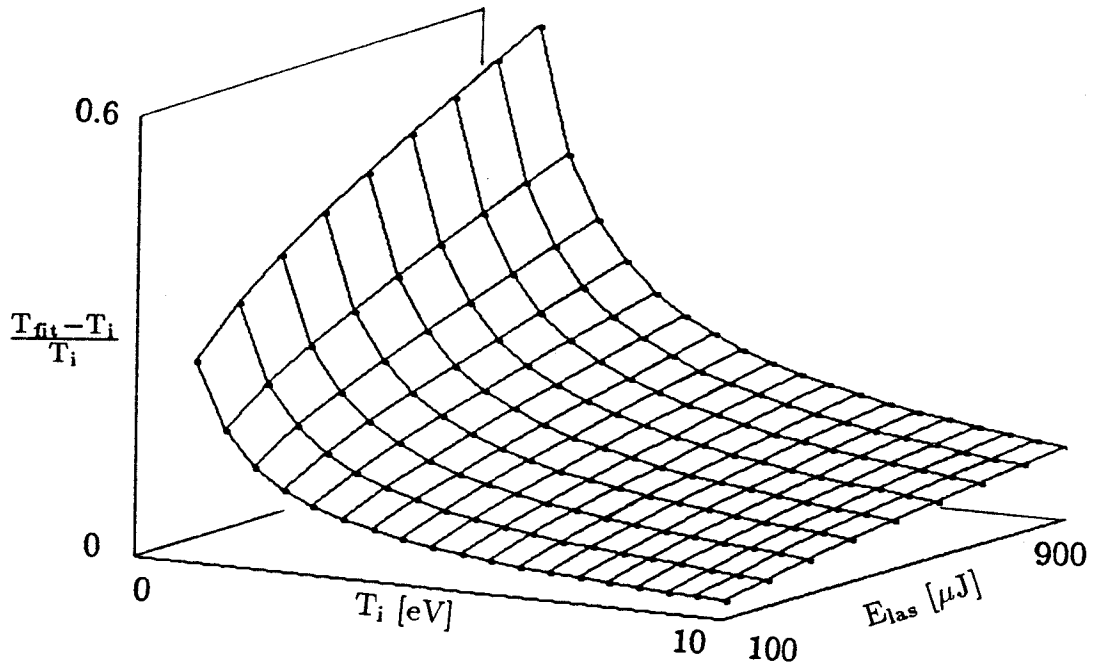

Figure 4.8 : Calculated power broadening errors in LIF temperature measurements. Data displayed in 0.5eV and 100μJ steps.

Transit time broadening (Stern '78) is another broadening mechanism similar to power broadening. The interaction time for slow particles moving through a laser beam is longer than that for fast particles. If there is a big difference in

interaction times for different velocity classes, the LIF signal will be primarily due to slower particles. Since the laser pulse length is very short in these experiments, the interaction time for all the particles is essentially the laser pulse length and transit time broadening is not a problem.

Using the models presented in this chapter, an estimate on the number of LIF photons/cm^3 can be made. Assuming a narrow bandwidth pulsed laser (Δf = 1.3GHz, Δt = 15ns, E = 300μJ/pulse) centered on the resonance and a metastable density $n_0 \sim 10^9 cm^{-3}$ consistent with the metastable model, there should be $N_{h\nu} \sim 5 \times 10^8$ photons/cm^3 available for detection.

The number of photons which are detected depends on the geometry of the collection optics and the sensitivity of the detector. The theoretical approximation can be compared to single point LIF data. The experimental setup is displayed in Figure 4.9. It is straightforward to relate the signal voltage V_{LIF} to an estimate of $N_{h\nu}$ using the energy per LIF photon hν, the diagnosed volume v, laser pulse length t, solid angle subtended by the optics Ω, filter transmission T, gain of the photomultiplier g_{PMT}, terminating resistor R and amplifier gain g_{amp}. Doing the calculations indicated in Figure 4.9 gives an estimate of $N_{h\nu} \sim 9 \times 10^8$ photons/cm^3 from $\sim$ 350 detected photons. The agreement between the measurement and the model is well within the errors introduced by the approximations used in both methods. The single point LIF measurements also make it clear that only a small number of photons are actually detected with a simple lens system. This fact played an important role in the design of the PLIF diagnostic system.

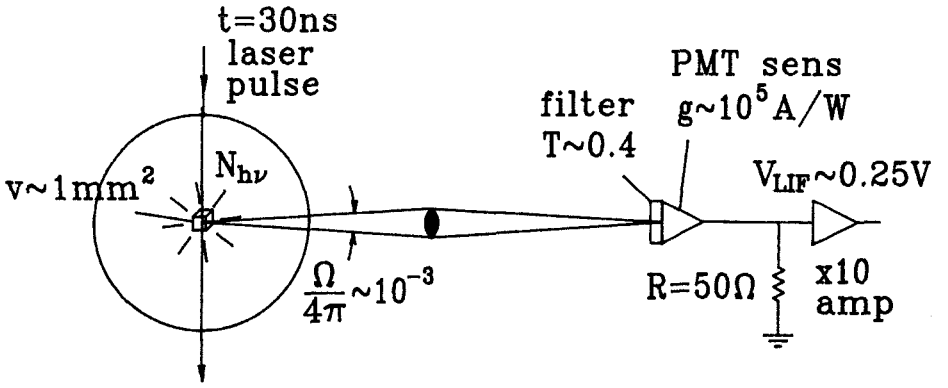

$$V_{LIF} = N_{h\nu}\frac{h\nu}{t}v\frac{\Omega}{4\pi}Tg_{PMT}Rg_{amp}$$

$$\#\text{photons detected} \approx \frac{V_{LIF}t}{Rg_{amp}g_{PMT}h\nu} \approx 350$$

Figure 4.9 : Metastable density estimate based on single point LIF measurements with simple geometry and detection circuitry.

5

PLASMA PLANAR LASER INDUCED FLUORESCENCE DIAGNOSTIC

5.1 System Goals

The plasma PLIF diagnostic has been designed to study ion dynamics in a poloidal cross section of the Ar plasma discharges in Caltech's Encore tokamak. A tokamak is a toroidal plasma device with a strong dc toroidal magnetic field and a weaker poloidal field due to the inductively driven toroidal current. Ideally the magnetic fields in a tokamak form nested toroidal flux surfaces which confine the plasma. To first order, the electrons are free to move along the magnetic field lines and are confined to flux surfaces perpendicular to the field. Since the electrons can move to 'cancel out' potential variations in the toroidal direction, often the most interesting plane to consider in a tokamak is a poloidal cross section perpendicular to the flux surfaces. The coherent drift waves which dominate Encore discharges are an example of a large amplitude, low frequency ($\omega \ll \omega_{ci}$) wave which is not 'canceled out' by the electron motion. A primary motivation for developing this diagnostic was to make PLIF images in a poloidal cross section of the plasma to further study the drift waves.

Simply imaging a poloidal cross section presents many challenges which constrain the experimental design. A number of these competing constraints are listed below. The optical viewing access to a poloidal cross section from outside the torus is limited. The object of the proposed optical system (the poloidal cross section) extends over a wide range of object distances. This makes imaging a two-dimensional surface a three-dimensional problem. The *image* area is fixed by

the size of the detector array, but the location of the imaged plasma is a complicated and sensitive function of the detector placement. Although a uniform image brightness is desirable, vignetting is a problem when imaging an extended object. As shown in Chapter 4, the number of LIF photons expected from an Encore LIF experiment is small so it is critical to collect as many photons as possible. The light collected must be filtered to eliminate scattered laser light and other emission lines from the plasma, but the simplest filter solution, a narrow bandpass interference filter, limits the collection efficiency *differently* over the image due to the shift in its transmission with the angular incidence of the light.

The detector and data acquisition system must also meet stringent requirements. The detector circuitry must be able to make measurements on $\sim$ 50ns time scales precisely timed with the laser pulse. The system must have high enough gain to make single shot measurements of the weak PLIF. To make *images* of the plasma a significant number of detectors must be used to achieve an acceptable spatial resolution. Many detectors with fast time response must be coupled with fast data handling so measurements can be made quickly. All of these goals cannot be achieved simultaneously with reasonable cost and complexity. The PLIF system resulting from the inevitable trade-offs between these competing goals is the subject of this chapter.

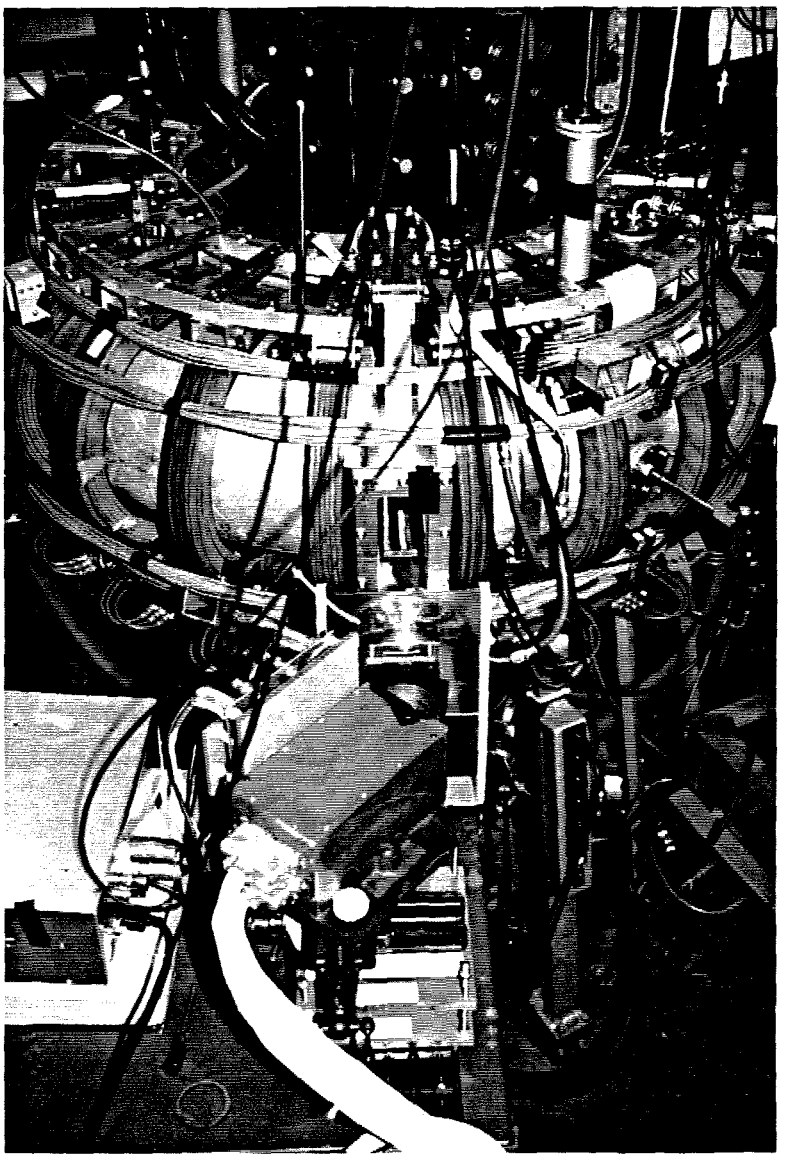

Figure 5.1 : Photograph of the PLIF experiment.

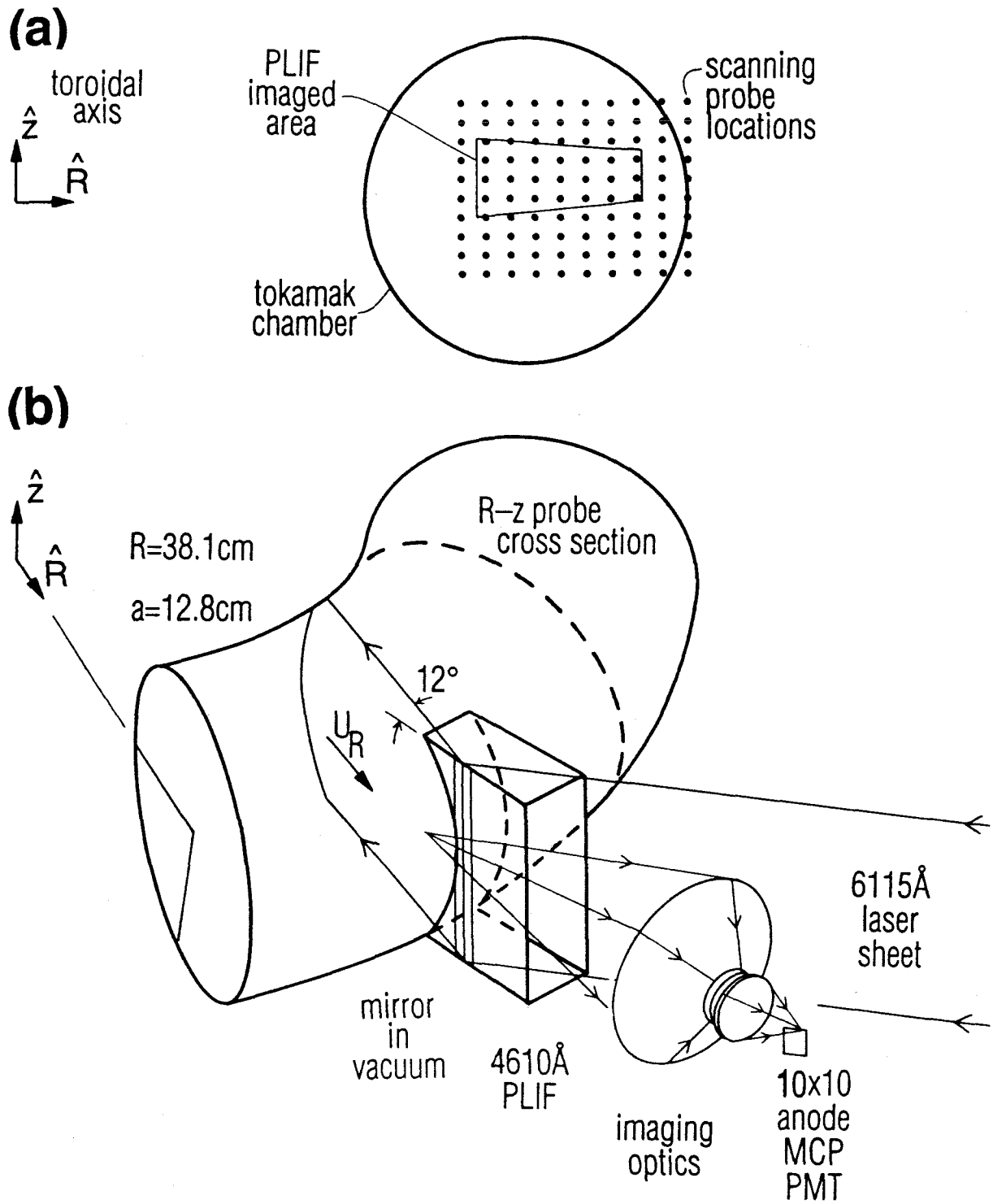

Figure 5.2 : (a) Projection of PLIF area in a poloidal cross section compared to the area scanned by the Langmuir probe (see Chapter 2). (b) Experimental setup.

5.2 System Design Overview

Figure 5.1 and Figure 5.2 show the PLIF experimental setup on Encore. PLIF at 4610Å from the ArII transition $4p'\,^2F^o_{7/2} \rightarrow 4s'\,^2D_{5/2}$ was excited by a narrow linewidth Nd-YAG pumped dye laser in resonance with the Doppler broadened transition from the metastable $3d'\,^2G_{9/2} \rightarrow 4p'\,^2F^o_{7/2}$. The pulsed 6115Å laser beam was expanded into a 0.5mm × 13cm sheet by a cylindrical lens. As shown in Figure 5.2(b), the sheet enters the vacuum vessel through a large port window and is reflected across the chamber $\sim 12^o$ to a major radius by a vertical mirror at the edge of the plasma. A beam dump (graphite powder in boron nitride) on the inside wall of the tokamak was necessary to prevent scattered light from inducing fluorescence outside the laser sheet. Plasma radiation and PLIF excited in the nearly poloidal cross section within the plasma exit through the same window. The light is filtered to eliminate all but the PLIF line and is imaged onto the photocathode of a gated, 10x10 anode, microchannel plate photomultiplier (MCP PMT). Since image magnification varies across the square anode array, the shape of the imaged plasma is a trapezoid (see Figure 5.2(a)) and the anode resolution varies from 9x4mm^2 to 20x7mm^2 (smaller than the ion gyroradius $\rho_i = 2 - 7$cm).

Because a low f/# Fresnel lens is used to increase collection of the small PLIF signal, a significant fraction of the rays are non-paraxial. Due to their large angles of incidence these rays would have been blocked by the shift in the transmission peak of the narrow bandwidth interference filter. To offset this effect, all rays were made to pass nearly paraxially through the filter by sandwiching the filter between a negative-positive lens pair. Although light from the PLIF transition is collected from the entire double cone subtended by the optics, the background emission forms an unfocussed, nearly uniform background 2-5 times smaller than the PLIF on the photocathode, is independent of laser wavelength and thus easily

subtracted. During a PLIF experiment the current pulses from each anode are fed into two separately gated channels of CAMAC controlled, gated integrators with 50ns gatewidths allowing single shot or averaged background subtraction; both methods are satisfactory. The stored analog signals are digitized and saved between discharges. A personal computer controls the CAMAC crates and custom electronics which in turn control the plasma, lasers and gated detector.

5.3 System Elements

Lasers

The previous single point LIF experiment on Encore (McChesney '87) used a tunable dye laser pumped by a copper vapor laser. The beam was transported by prisms from another room to the Encore plasma. The $\sim 80\mu J/mm^2$, 30ns pulse was more than adequate for making single point ($\sim 1mm^3$) measurements. The PLIF experiment described here would have required the same beam to be spread into a sheet with $\sim$ 100 times more area; this would have reduced the PLIF intensity to marginal levels even with an improved beam path.

A copper vapor laser depends on a repetitive pulsed high current plasma discharge to vaporize and excite copper in a large lasing volume. Our laser (Plasma Kinetics 451) had a number of problems stemming from this basic design including a marginally designed pulsed power electronics circuit based on expensive and often temperamental tubes, frequent maintainance problems which inactivated the laser, 2-3 hour warm-up delays even in normal operation, a fixed 6kHz repetition rate limiting experimental triggering flexibility and uncontrollable power drifts on experimental time scales ($\sim$1 hour). For the PLIF experiments the copper vapor laser was replaced by a Nd-YAG laser (Molectron MY32).†

† Thanks go to Caltech Professor A. Yariv for loaning us the YAG laser.

The Q-switched, frequency doubled Nd-YAG is a much more reliable and versatile pump laser (λ_{SHG} = 532nm, $t_{las} = 15 - 30$ns, E_{SHG}=80mJ/pulse). The YAG laser itself is flashlamp pumped so there are no startup delays. Although the flashlamps must be triggered at the plasma discharge rate (15 Hz) to decrease energy jitter, the timing tolerances are large enough to allow variable timing delays throughout the plasma lifetime (> 1 ms). The power stability is very good over many hours of operation with minimal adjustments of the doubling crystal with pulse to pulse energy jitter $\sim$15%. The YAG is Q-switched independently of the flashlamps so the laser can be 'turned off' by not sending the Q-switch trigger. This is an extremely important improvement because the computer can now be programmed to make background and PLIF measurements automatically. The flashlamps must be triggered 1ms before the Q-switch, but there is a $\sim$ 50μs tolerance in the relative timing between pulses. This enables the system to be fired with respect to an almost reproducible event in the plasma, e.g., wave phase.

The YAG pumps a Kiton Red 620/Rhodamine 640 dye mixture in a Lambda Physik FL2001 laser. The dye laser beam energy can be as high as 3mJ per pulse. During PLIF experiments the pulse energy (measured at the tokamak) was kept below 300μJ to avoid power broadening. The oscillator design is shown in Figure 5.3. Coarse tuning of the dye laser is performed by the prism beam expander and grating which acts as a very selective cavity mirror (Δf = 6GHz). An intracavity etalon narrows the line to 1.3 GHz and provides fine wavelength control necessary for ion distribution function measurements in Encore. The laser wavelength is determined by the angles of the grating and etalon which are externally controlled by stepper motors during the experiment (cf. McChesney '89). Although the laser linewidth and relative wavelength shifts were measured accurately with an external scanning etalon, the absolute wavelength of the laser has not been calibrated with

equal accuracy. The value of the zero velocity wavelength shift in the absorption line must be chosen to set the absolute wavelength of the laser.

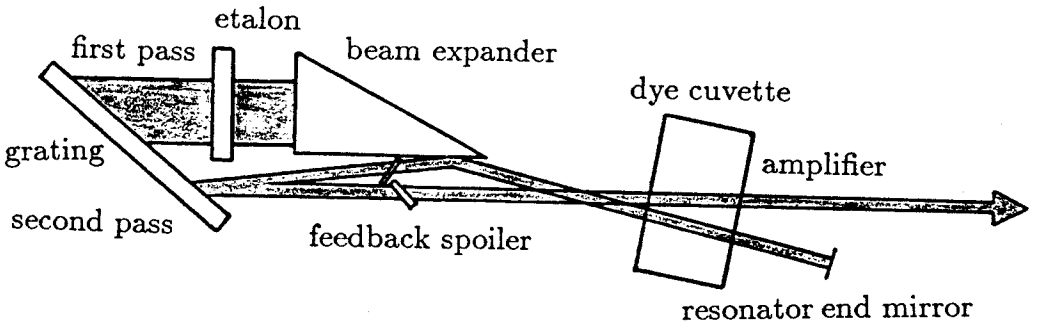

Figure 5.3 : Lambda Physik oscillator design.

As discussed in Chapter 3 it is desirable to make the laser line broader than 6GHz for single shot ion density measurements. To do this, part of the grating could be covered in normal operation, reducing the number of lines diffracting the expanded beam thus degrading the cavity spectral resolution. Another possible way to increase the laser linewidth is to exploit an unusual feature of the Lambda Physik oscillator design: the second pass of the light off a small spot on the grating (see Figure 5.3). By completely blocking the grating on the first pass and removing the feedback spoiler in the second pass, the laser linewidth can be broadened to $\sim$ 120GHz.†

† T.K. Gamble, private communication. His group at Los Alamos does PLIF on laser ablated Cu atoms using a Lambda Physik LPD3002.

Imaging Optics

A large Fresnel lens (ϕ=153mm, f=76.5mm) was used to collect as much light from the plasma as possible. A negative lens (ϕ=46mm, f=-50mm) was used immediately before the large narrow bandwidth interference filter (ϕ = 50.8mm, 10Å, Pomfret 10-4610-2) to make the light pass through the filter nearly parallel to the optical axis, increasing filter transmission. A positive lens (ϕ=50mm, f=50mm) refocussed the filtered PLIF onto the MCP PMT photocathode (ϕ=20mm). The negative lens is mounted in a fixed holder, the positive lens in a threaded lens tube which screws into the holder, sandwiching the filter between the lenses. For optics alignment, a spacer ring is used instead of the filter so a pattern on an illuminated slide viewer in the object plane can be focused visually.

Unfortunately, there are complications inherent in this optical design. The decrease in image intensity at the edges caused by the tokamak aperture, finite lens dimensions and filter transmission lead to severe vignetting. Results of system transmission calculations (see Appendix E) indicate that lens displacements of a few millimeters can change relative transmission figures between anodes by two orders of magnitude. Until these problems are resolved, quantitative single shot metastable density images cannot be made reliably. A possible way to avoid these problems is to image a much smaller region of the cross section. The more point-like the imaged region, the less variation in system transmission. Such a system could also be mounted on a remotely controlled precision three axis movable stage. Composite images could then be used to significantly increase the resolution of the PLIF system when single shot measurements are not required.

Multianode Microchannel Plate Photomultiplier

The imaging detector used in the PLIF diagnostic system is a gated 10x10 anode microchannel plate photomultiplier (Hamamatsu R3801). A schematic of

the MCP PMT and the gating circuit is shown in Figure 5.4. The PLIF image is focussed on the bialkali photocathode of the MCP PMT. Photoelectrons are ejected proportional to the number of photons hitting the photocathode. The electron flux inside the PMT has the same spatial variations as the focused PLIF image on the photocathode. The electrons are imaged by electrostatic focusing anodes onto the face of the chevron pair of MCPs which have an electron gain of $\sim 10^6$. The MCPs provide the required gain in the PLIF system *without* losing the spatial information in the electron image.

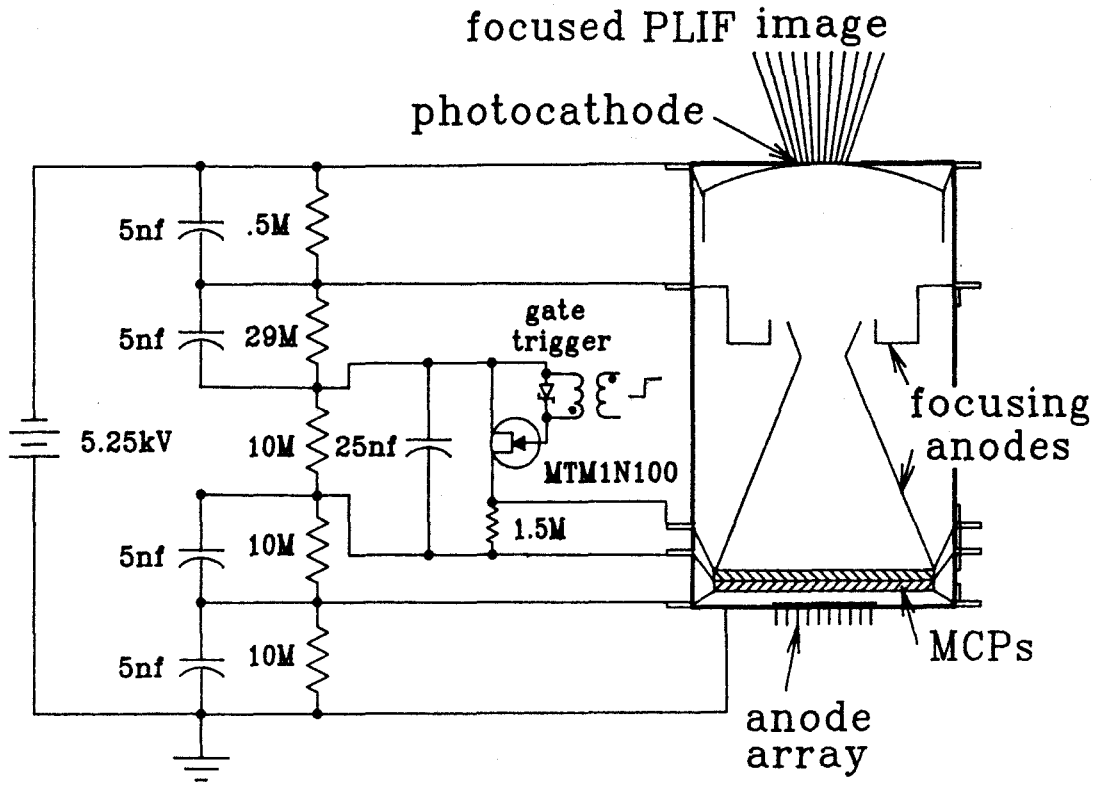

Figure 5.4 : Multianode microchannel plate photomultiplier and gating circuit.

One MCP (in this PMT) is a 0.48mm thick piece of lead glass constructed from glass tubes processed by a draw/multi-draw technique which results in a rod with 12μ diameter channels spaced 15μ apart. A plate is cut from the rod at an angle of 5^o to the channels to ensure no electrons can go through the plate without hitting a channel wall. High temperature reduction of the lead glass in a hydrogen atmosphere coats the insides of the channels with a resistive semiconductor layer with a high secondary electron coefficient (Wiza '79). When the plate faces are coated with electrodes (Fe-Cr) and a $\sim$1kV bias is applied across the plate, any photoelectron from the photocathode which strikes the inner wall of a microchannel begins an exponential electron cascade. Each channel can be considered a continuous dynode structure that acts as its own dynode resistor chain. The spatial information in the initial electron image is retained since the entire cascade takes place within a single microchannel. To increase the electron multiplier to $\sim 10^6$, two plates are connected in series. The channels are arranged to form a chevron to suppress ion feedback which can cause sputtering damage to the MCP. The electrons exiting the last MCP are collected by metal anodes causing a current proportional to the intensity of the optical image on the photocathode.

The MCP PMT was chosen over other detector options such as an amplified PIN diode array or an intensified charge coupled device (CCD) camera because it successfully incorporated three characteristics which the other systems could not match: high gain and large pixel elements in an integrated package. Although an intensified CCD has comparable gain to the MCP PMT, CCDs have very small light sensitive areas with large (typically 256x256) arrays of small pixels $\sim$50-100μ on a side. Given the magnification needed to image a large fraction of the poloidal cross section on a CCD, less than $\sim$10 photons would be detected per pixel even with very good optics. On the other hand, PIN diodes are readily available in

1mm^2 pixels so hundreds of photons could be detected, but PIN diodes do not have high gain. A single channel amplifier with a gain of $\sim 10^6$ capable of detecting 50ns pulses of PLIF was built and tested, but its performance was unsatisfactory.

MCP PMT Characteristics	
cathode radiant sensitivity @ 4600Å	55 mA/W
quantum efficiency @ 4600Å	14.4%
electron collection efficiency	$\sim$ 50%
channel packing fraction	58%
electron multiplier @ 1.6kV dc	1.7×10^6
anode size	1x1mm^2

Table 5.1: MCP PMT characteristics reported by Hamamatsu.

The characteristics of the MCP PMT are displayed in Table 5.1. One important characteristic not shown is the fact that MCPs saturate. The charge liberated from the walls of the channels is replaced slowly by current flowing along the highly resistive channel walls. For illumination levels in the PLIF system, the MCP PMT saturated in $\sim$ 250ns. This limitation was overcome by gating the 1kV bias voltage of the first MCP using a high voltage MOS FET ($\tau_{\text{rise}} \approx$ 50ns, see Figure 5.4 for circuit and Figure 5.5 for MCP PMT gate and response). The gate turn-off is not critical since the tube is saturated long before then. Although the MCP recharge time is long ($\sim$ 6ms) compared to the plasma lifetime, it is short compared to the time between discharges (66.7 ms).

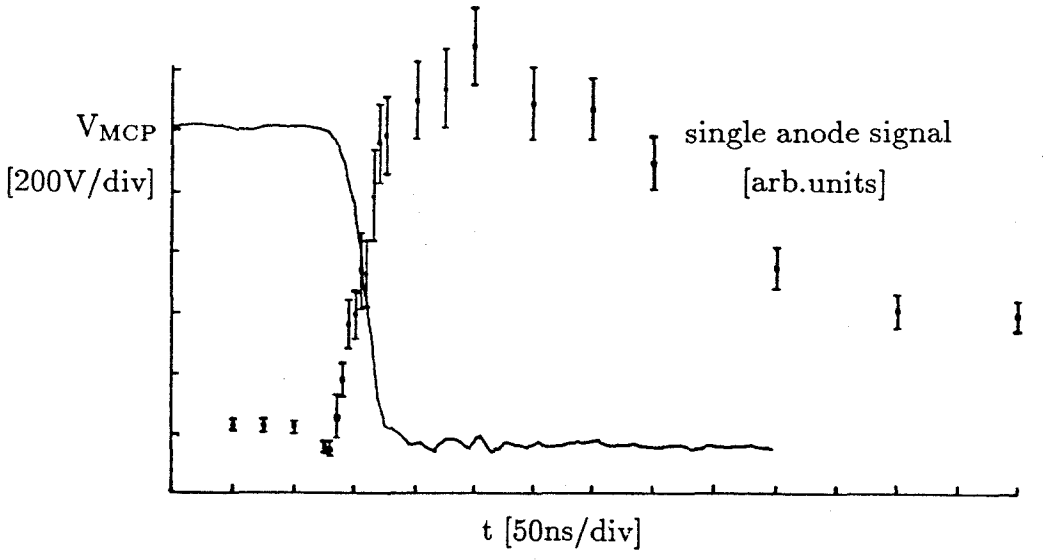

Figure 5.5 : MCP PMT gating pulse and single anode response.

Even while gating the MCP, it is possible to saturate the MCP during the 50ns measurement window. To stay in the linear signal regime for *all* the anodes, neutral density and colored glass filters were used to control the light intensity (44.6% transmission @ 460nm). It is ironic that half of the light collected is then filtered out, but simpler lens systems only aggravate the vignetting problem. Gating the MCP also caused problems with the electrostatic focusing of the electron image in the MCP PMT. Using an electro-optically modulated He-Ne laser beam, the effective size and gain of the center anodes were found to be greater than those on the edge when the MCP was gated. A uniform response was achieved by adjusting the factory suggested bias levels on the focusing anodes.

Gated Integrators

The currents collected by the 100 MCP PMT anodes were fed via ~30 feet of 50Ω RG178 cable per channel into a number of 32 channel CAMAC controlled,

gated integrators called SHAMs.† The voltage across the 50Ω input resistance generated by the PMT current controls a current source inside the SHAMs which charges a capacitor during the 50ns signal gate giving a gain of 2.6×10^{10}V/coulomb (effective capacitance 37.5pF). After the signal gate, each channel of a SHAM module is sequentially output to a multiplexer (Standard Engineering MX-016A). The multiplexer output is fed to an analog to digital converter (Kinetic Systems 3553, 12 bit, 1.22 mV/count) which is read via the CAMAC bus and stored in a 25MHz 486 personal computer. The SHAMs are very reliable instruments. All the channels have been individually calibrated with the cable between the MCP PMT and the CAMAC crate. They were all found to have linear responses very near the reported values (Cisneros '80).

Data Acquisition and Experimental Control

The entire tokamak has been put under the control of a personal computer. The precise timing necessary for the PLIF experiment was also controlled by the computer via a CAMAC output register (DSP PR612) which communicated with a number of circuits designed and built for the experiment. Figure 5.6 shows a schematic of the timing and control.

† The etymology of 'SHAM' is uncertain although it may stand for Sample and Hold Analog Multiplexer. Ours are on loan from the Stanford Linear Accelerator Center where they were developed.

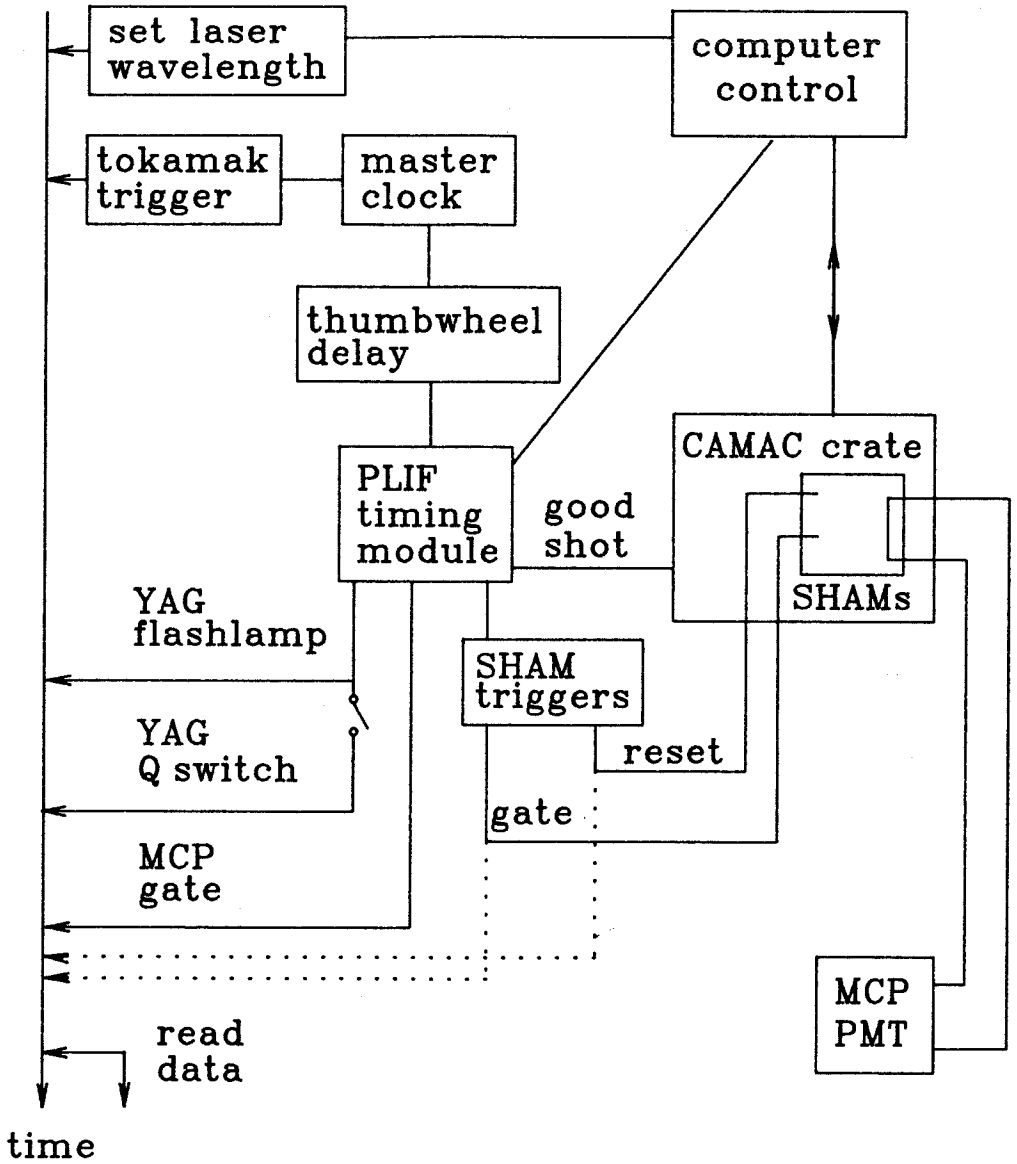

Figure 5.6 : Experimental timing and control.

A voltage controlled oscillator in a phase locked loop on the 60Hz line (to avoid the three phase modulations in the toroidal magnetic field) generated a timing clock which was divided down to trigger the tokamak discharge via a preloaded CAMAC waveform generator (BiRa H910). A variable delay based on the same clock then triggered the custom PLIF system timing module. During the experiment the PLIF timing module is controlled by the computer via the CAMAC output register. It sets the PLIF measurement time, triggers the YAG flashlamp and Q-switch, triggers the MCP gate, sends a 'good' shot trigger to a computer monitored CAMAC line and triggers electronics which send the reset and signal gates to the SHAMs. The laser wavelength is set by stepper motors also controlled via the CAMAC output register. All the data for one discharge is acquired before the next discharge at the 15Hz discharge rate. Data from approximately 150 discharges could be saved in RAM before being stored to disk automatically during PLIF scans. Three other features of the system discussed below will prove useful in the future.

In some operating regimes the Encore plasma discharge is not as reproducible as desired, but the waves are almost reproducible. The timing module can be armed (by computer) so the data acquisition time is set by an external trigger within an 'allowed' time window. If such a trigger is not received, the Q-switch and 'good' shot triggers are not sent and no data is collected. This mode has been used in conjunction with a circuit monitoring a Langmuir probe in the plasma edge detecting the drift wave density fluctuations. The plasma shots which vary too much from a chosen discharge are discarded. A similar option monitoring the laser energy is also operational. A fast photodiode signal is fed into a spare SHAM channel. If the energy level as read from the SHAM falls outside a user specified range the data is discarded. Both these methods were found to reduce the

shot-to-shot signal fluctuations. Since the plasma was very reproducible for the experiments described in this thesis, the reduced data acquisition rates outweighed the data improvement and these techniques were not used.

The PLIF timing module is also prepared to control a second laser system which has recently been installed. The circuitry and programming is designed to allow the timing flexibility and control for the first planar tagging experiments or concurrent single point LIF experiments.

5.4 System Performance

Using the system parameters presented in the last section an estimate of the system sensitivity can be made. Ignoring the uncertainties in the numbers, the digitized PLIF signal is

$$D = \gamma_e \sigma_p \alpha_o I_p \quad [\text{counts}]$$

where I_p is the plasma emission at the PLIF wavelength in W/cm^2, α_o is the 'efficiency' of the optics and interference filter to collect the light in cm^2 (see Appendix E for derivation), σ_p is the sensitivity of the MCP PMT in A/W and γ_e is the conversion factor for the rest of the electronics in counts/A. Ignoring the background emission

$$I_p \approx (h\nu/t_{det}) N_{h\nu} \Delta_\perp \sim 10^{-12} N_{h\nu} \text{ W/cm}^2 \quad \text{with } N_{h\nu} \text{ in cm}^{-3}$$

$$\alpha_o \approx 10^{-3} \text{cm}^2$$

$$\sigma_p \approx s\, \epsilon g_{MCP} \sim 10^4 \text{ A/W}$$

$$\gamma_e \approx r_{ADC} t_{det} / C_{SHAM} \sim 10^5 \text{ counts/A}$$

where t_{det} is the detection time; $h\nu$ is the energy of an LIF photon; $N_{h\nu}$ is the number of LIF photons/cm^3 (see Chapter 4 and Appendix D); $\Delta_\perp$ is the transverse dimension of the laser sheet; s is the MCP PMT photocathode radiant sensitivity

at the LIF wavelength; ϵ is the product of the transmission of the filters used to keep the MCP out of saturation, the electron collection efficiency and channel packing fraction inside the MCP PMT; g_{MCP} is the MCP gain; C_{SHAM} is the effective capacitance of the SHAMs and r_{ADC} is the ADC conversion resolution (820 counts/V). This calculation gives ~1 count per detected photon and a sensitivity of $\sim 10^{-6} N_{h\nu}$ counts. For typical PLIF measurements D $\sim$ 300 counts which implies a metastable density $\sim 10^8 cm^{-3}$, an order of magnitude lower than the calculations and the single point measurements discussed in Chapter 4. This is still good agreement given the uncertainties in the values used in the calculation, especially α_o and g_{MCP}.

The major design goal left unmet by the PLIF diagnostic is a confident determination of the gains of the system. The optical collection efficiency is sensitive to small changes in lens position and the absolute gains of the gated MCP PMT are not known accurately. In principle it should be possible to devise a calibrated flat field light source at 4610Å which could be used to calibrate the optics and MCP PMT gains simultaneously. However, this would be non-trivial and has not been attempted.

The PLIF diagnostic system *has* met most of the design goals originally posed. In addition, the laser system has been significantly upgraded with the YAG which provides a more reliable, energetic laser beam. The YAG also introduces the experimental flexibility of computer controlled shuttering and variable external triggering of the laser. An additional laser system has also been set up and is ready to be used in future PLIF experiments. The existing plasma PLIF diagnostic system successfully images a significant fraction of a poloidal cross section with a detector and data acquisition system capable of making single shot measurements of PLIF at the 15Hz discharge rate.

6

PLIF MEASURED ION FLUID VELOCITY AND TEMPERATURE FIELDS

6.1 The PLIF Experiment and Data

The plasma PLIF diagnostic system described in the last chapter was used to measure the ArII velocity distributions in the undriven, large amplitude, low frequency, coherent drift waves dominating the discharges in Caltech's Encore tokamak. PLIF excited by the laser sheet is measured on a 10x10 spatial grid with resolution of the order of the ion gyroradius in a poloidal cross section (see Figure 6.1).

The PLIF data presented in this chapter and Langmuir probe data described in Chapter 2 were taken during 15 hours of continuous Encore discharges with the same monitored machine and plasma parameters. Figure 6.2 shows the coherent density oscillations of the wave measured with the fixed Langmuir probe biased to collect the ion saturation current in the plasma edge. The waves in each discharge are reproducible so variable time delays from the tokamak trigger were used to trigger PLIF data acquisition in phase with the waves. For a given time in the plasma, ion velocity distributions are deduced by scanning the narrow linewidth dye laser wavelength and measuring the resulting PLIF signals. The measurements presented here were averaged over 75 discharges for each of 51 wavelengths ($\Delta\lambda = 0.01$Å). The data set for each anode is χ^2 fit to a Maxwellian with the amplitude, amplitude offset, temperature and center wavelength as parameters (see Figure 6.3). The ion fluid velocity parallel to the laser propagation vector is $u_R = c\Delta\lambda/\lambda_o$ where $\Delta\lambda = \lambda_c - \lambda_o$ is the Doppler induced shift of the center wavelength of the distribution λ_c from the PLIF absorption wavelength

$\lambda_o = 6114.92$Å(Norlén '73) for a stationary ion. The maximum measured wavelength shifts $\Delta\lambda \sim 0.03$Å correspond to velocities $u_R \sim 1.5 \times 10^5$cm/s.

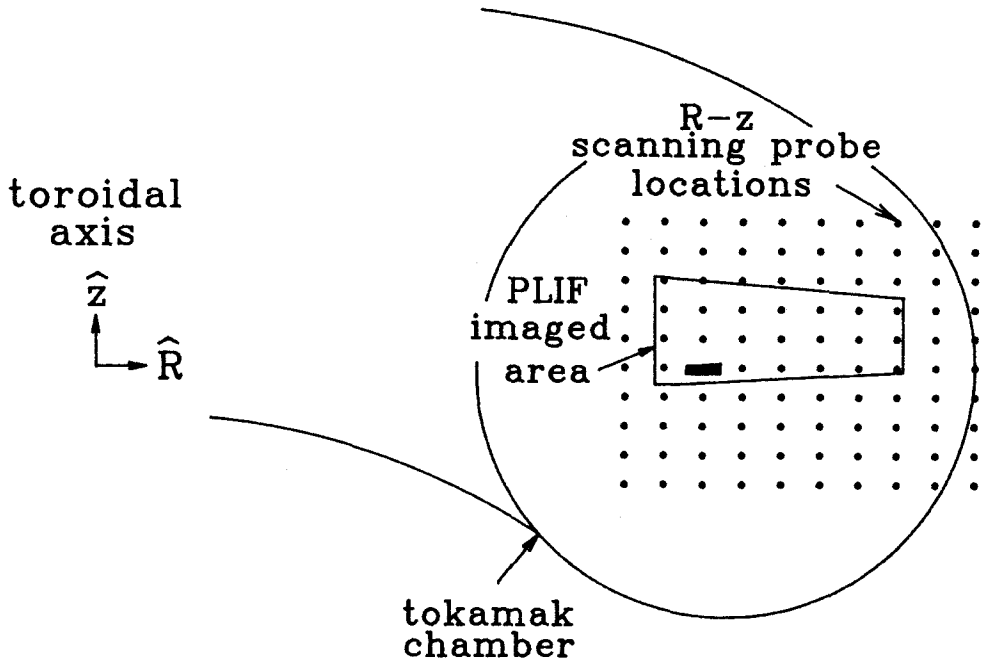

Figure 6.1 : Poloidal cross section of Encore showing imaged plasma. The data in Figure 6.6 is from the shaded anode.

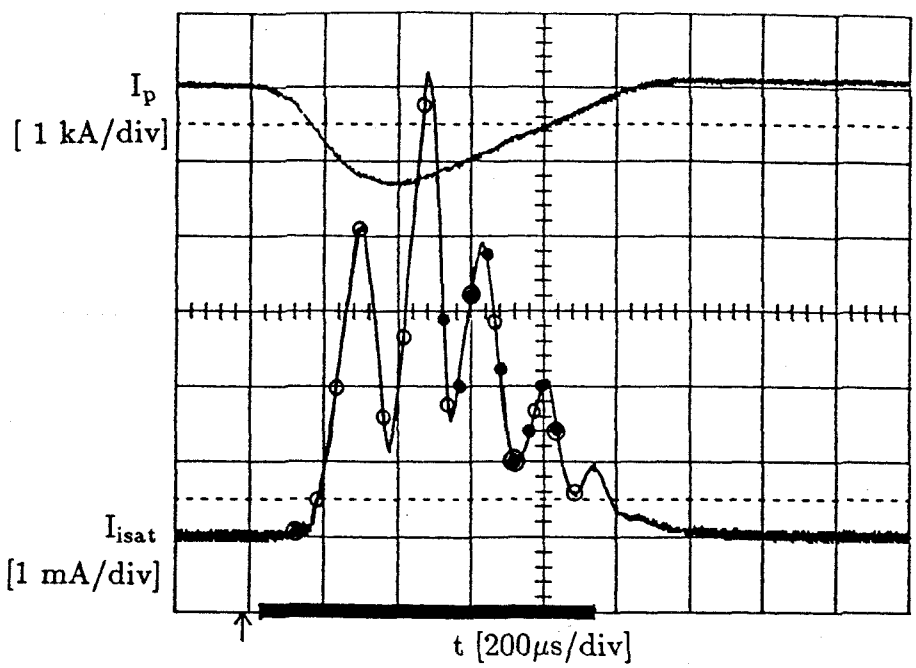

Figure 6.2 : Ion saturation current to a Langmuir probe in the edge showing drift wave density fluctuations. PLIF data was taken at 20μs time intervals during the time indicated by the heavy bar on the time axis. Open circles mark the times for the data displayed in Figure 6.4 and filled circles for Figure 6.5.

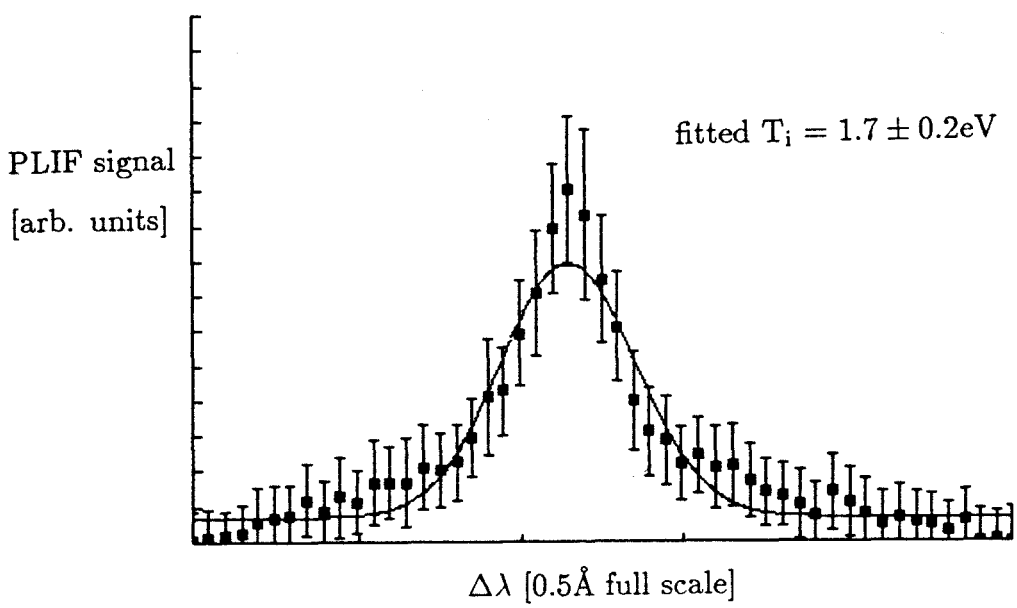

Figure 6.3 : Example of a measured ion distribution function and a χ^2 fit.

Figure 6.4 displays smoothed images of the primary measurements of this thesis. The PLIF measured ion temperature T_i and center wavelength λ_c are displayed with the probe measured density in 60μs intervals during the plasma (see Figure 6.2). There are clear oscillations in both the λ_c and T_i measurements coherent with the drift wave fluctuations. Regions of increased T_i and lower λ_c repeatedly appear in the upper left corner of the imaged region, move down and fill the lower half of the image and then move out of view off the lower right corner. The regions of lower λ_c, i.e., blue shifted *absorption* line, correspond to regions of ion fluid moving opposite the laser propagation (to the left in the figures). These regions of retreating ion fluid are closely correlated with the regions of increased T_i. The PLIF measured $\Delta\lambda_c$ are quite small compared to the widths of the distributions, but the observed fluctuations are repeatable. Based on the consistency of many hundreds of measurements with repeatable spatial variations and the smooth temporal variations in u_R observed on single anodes, the estimated uncertainty in the u_R measurements is $\pm 8 \times 10^3$cm/s.

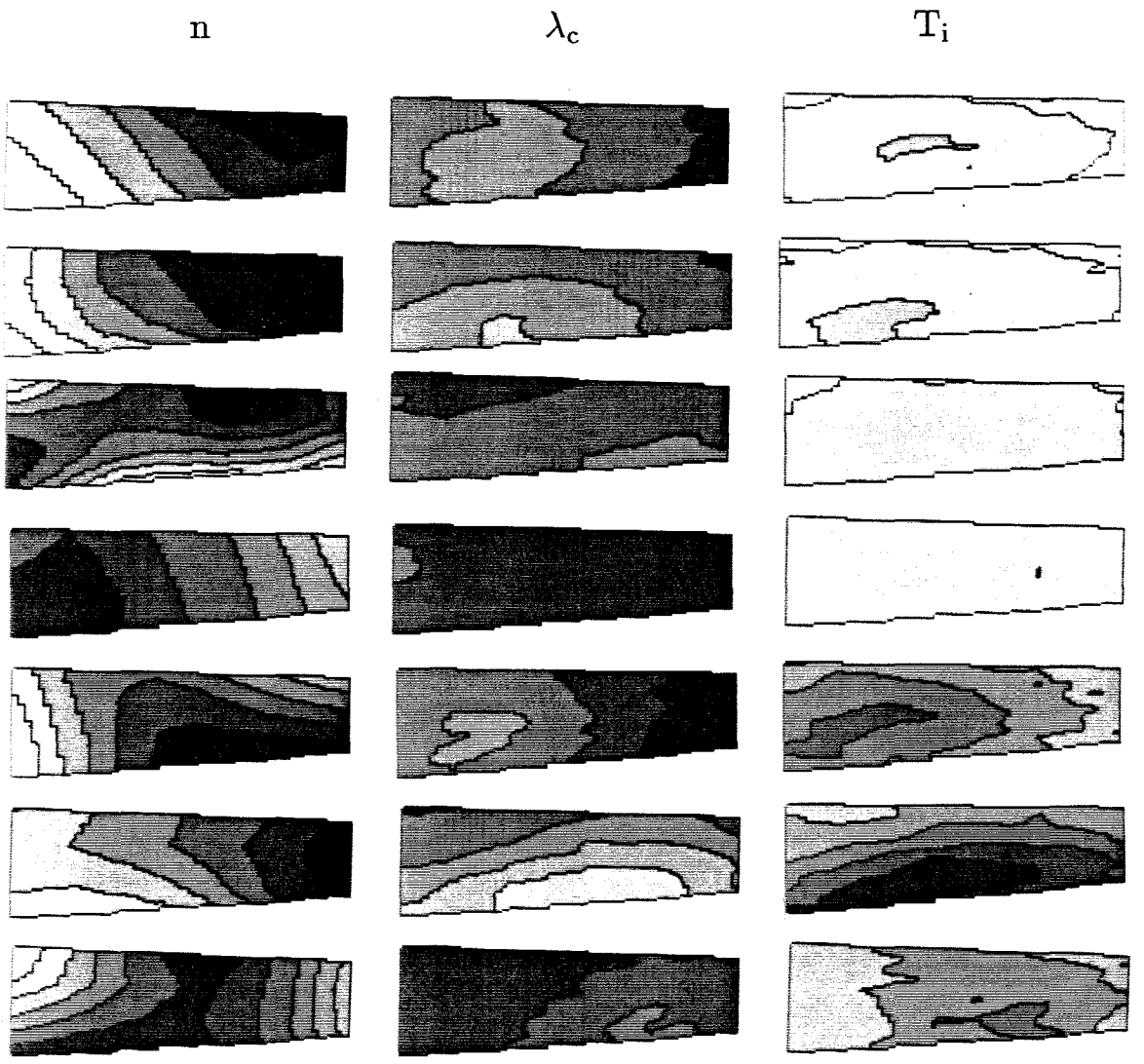

Figure 6.4 : PLIF measured λ_c and T_i and Langmuir probe measured density displayed in 60μs intervals during the discharge. Time advances from the top to the bottom corresponding to the open circles in Figure 6.2. Each image is plotted in a six-level linear gray scale progressively darker for larger data values; Each density image is plotted normalized to its own data range. The λ_c and T_i scales are fixed: $\Delta\lambda_c = 0.055$Å and the range of T_i is 2 to 10.5eV full scale. The magnetic field points out of the page so that the electron diamagnetic rotation is counterclockwise.

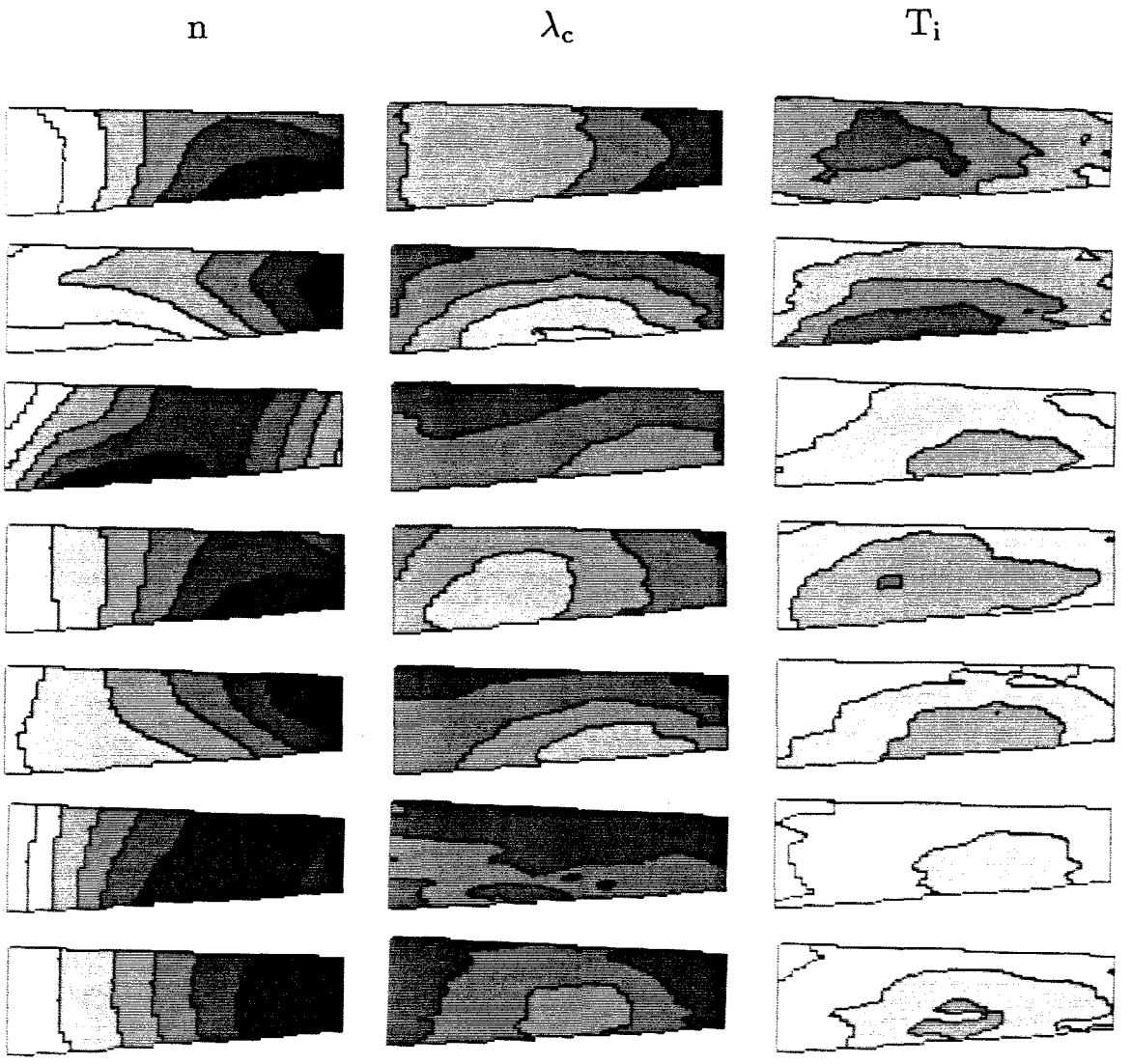

Figure 6.4 (continued): $\Delta\lambda_c = 0.055$Å, T_i 2 to 10.5eV.

6.2 PLIF Measured Ion Fluid Velocity Field

By choosing λ_o in the center of the observed oscillations, the time dependent spatial structure of the ion fluid velocity field can be displayed using black and white for the sign of u_R (see Figure 6.5(a)). The dominant feature of the u_R field is a periodic spatial movement of localized regions of positive and negative u_R in phase with the wave. Figure 6.5(a) shows the upper left corner of the imaged plasma with a negative u_R component at t_1. During the next 80μs (t_2, t_3) the region moves down and to the right, across the lower half of the image. The negative u_R region is shrinking into the lower right corner at t_4, disappearing altogether at t_5. A new region has dropped and expanded to fill the left half of the image at t_6 to repeat the cycle again during the next 80μs. This pattern is observed for all five wave periods in this plasma (see Figure 6.4) and is typical of Encore discharges having coherent drift waves.

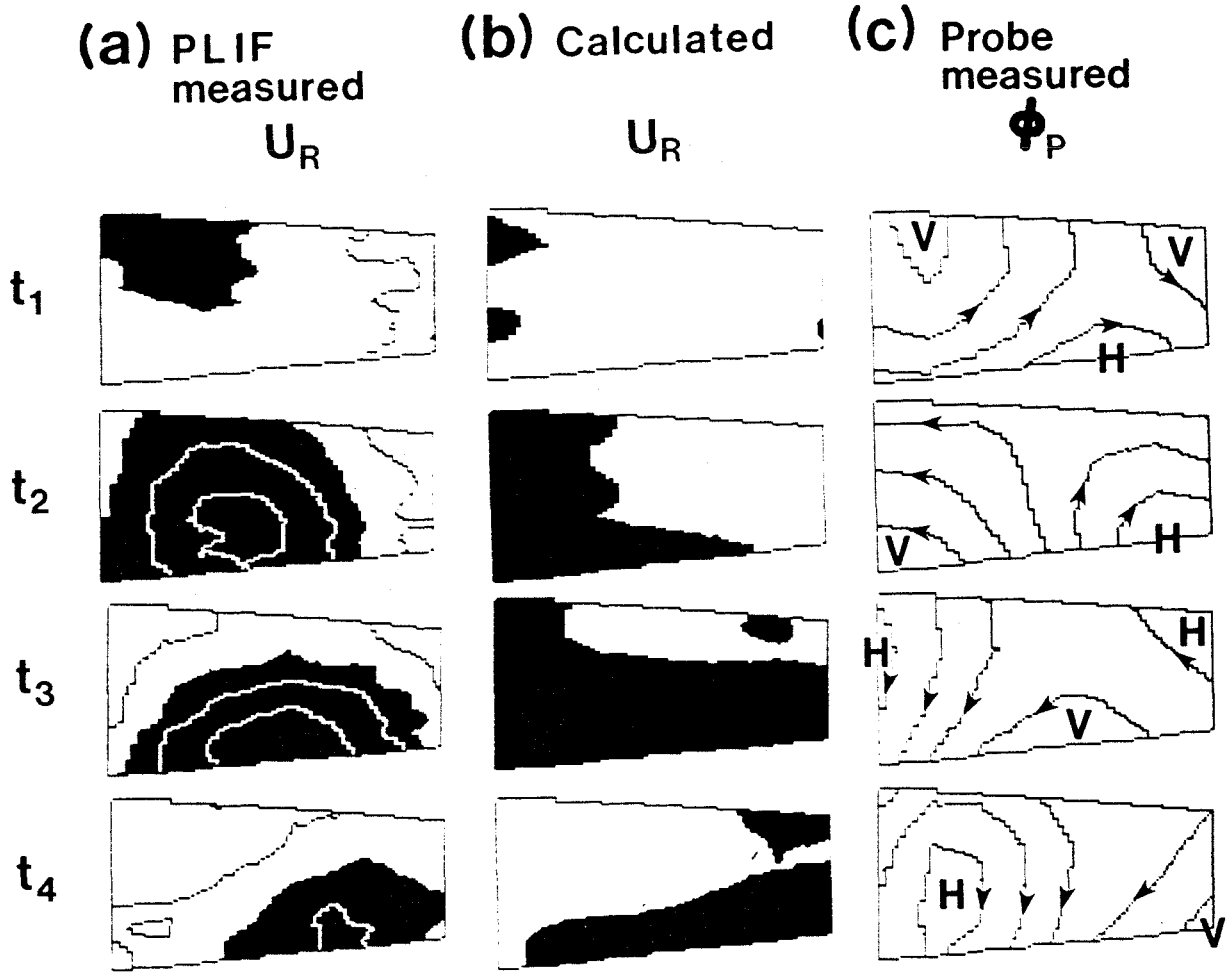

Figure 6.5 : (a) PLIF measured u_R field (full scale $\pm 1.1 \times 10^5$cm/s, 2.7×10^4 (cm/s)/contour) (b) u_R field calculated using the drift approximation. Black(white) indicate velocities to the left(right) for u_R. (c) Langmuir probe measured $\tilde{\phi}$ (2 V/contour). Arrows on the equipotentials indicate the direction of $\mathbf{E} \times \mathbf{B}$ drifts around potential hills (H) and valleys (V). Time advances from the top to the bottom in 40μs intervals corresponding to the filled circles in Figure 6.2. See Figure 6.1 for the correct spatial aspect ratio. $\mathbf{B}$ is out of the page so that the electron diamagnetic rotation is counterclockwise.

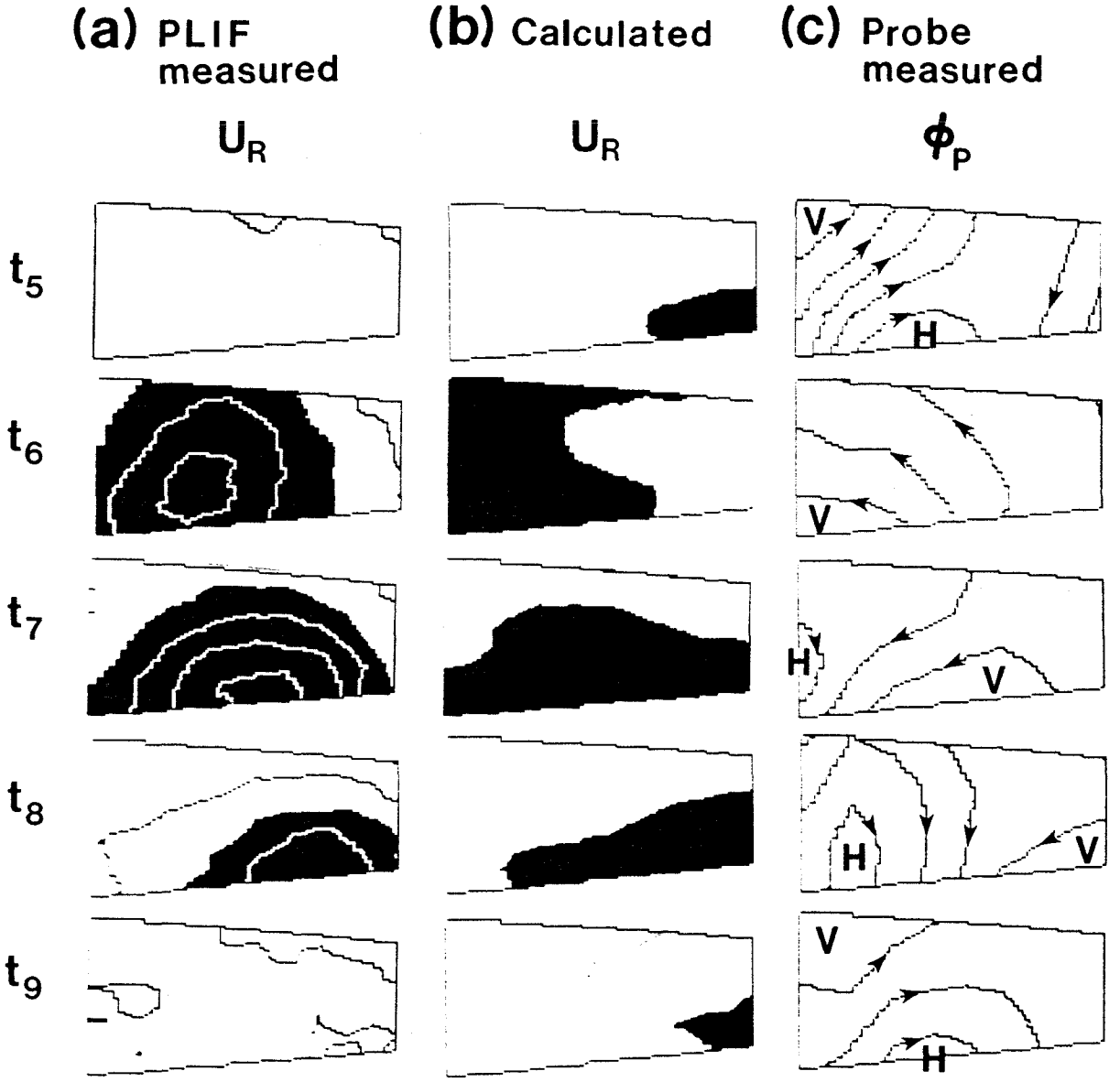

Figure 6.5: (continued)

The complete two-dimensional velocity flow field consistent with this data is not immediately obvious since only the single component u_R is measured. As the Langmuir probe data in Chapter 2 showed, the Encore plasma is not a uniform plasma with a controlled, single mode, monochromatic perturbation, but a dynamic plasma dominated by a naturally occurring, spatially complex, time dependent wave. To provide an interpretation of the PLIF data without using analytic functions for the plasma parameters, the Langmuir probe measurements made in a nearby poloidal cross section (separated toroidally by 0.1 parallel drift wavelengths) are used to calculate the solution of the ion fluid equation of motion in the drift approximation.

The two-fluid plasma theory provides a self-consistent approximation of the plasma treating the electrons and ions as two conducting fluids coupled by Maxwell's equations. The ion fluid equation of motion

$$nm\Big\{\frac{\partial \mathbf{u}}{\partial t} + \mathbf{u}\cdot\nabla\mathbf{u}\Big\} = en\big\{\mathbf{E} + \mathbf{u}\times\mathbf{B}\big\} - \nabla(nT_i) \tag{6.1}$$

is a nonlinear partial differential equation for the ion fluid velocity $\mathbf{u}(\mathbf{x}, t)$ as a function of space and time in terms of the electric and magnetic fields, ion density and ion temperature, all of which may depend on space and time. The ion charge e and mass m are considered constant and the ion pressure has been taken to be nT_i. Given $\mathbf{E}$, $\mathbf{B}$, n and T_i, a solution for $\mathbf{u}(\mathbf{x}, t)$ in Eq. 6.1 would be the self-consistent ion fluid velocity (in the two-fluid approximation).

The ion fluid velocity perpendicular to the magnetic field can be solved in the drift approximation by ignoring the total time derivative on the left-hand side of Eq. 6.1. Checking the magnitude of the ignored terms in a one-dimensional drift wave, this approximation is equivalent to requiring the wave frequency to be low compared to the cyclotron frequency $\omega/\omega_{ci} \ll 1$ to drop the $\partial\mathbf{u}/\partial t$ term and

the normalized wave amplitude $\alpha = k^2\tilde{\phi}/\omega_c B$ must be small, $\alpha \ll 1$, to drop the $\mathbf{u}\cdot\nabla\mathbf{u}$ term. Considering the drift waves in Encore as plane waves, these ratios are $\omega/\omega_{ci} \approx 0.5$ and $\alpha \approx 1$. Since Eq. 6.1 exhibits both radial and azimuthal nonlinearity the exact requirements for the validity of the drift approximation in the experiment are not known precisely. Ignoring the validity questions for the moment and assuming the waves are electrostatic, the ion fluid velocity in the drift approximation is the sum of the $\mathbf{E}\times\mathbf{B}$ and diamagnetic drifts so that the $\hat{\mathbf{R}}$ component of the ion fluid velocity is

$$u_R = \hat{\mathbf{R}}\cdot\left[\frac{-\nabla\phi_p\times\mathbf{B}}{B^2} - \frac{\nabla(nT_i)\times\mathbf{B}}{enB^2}\right]. \tag{6.2}$$

A theoretical prediction for u_R can be calculated from Eq. 6.2 using the Langmuir probe and PLIF data. The local density (determined by the Langmuir probe with a temporal shift to account for $k_{||}$) and T_i measured by PLIF are used to calculate the diamagnetic drift. Figure 6.5(b) shows u_R images *calculated* for the same sequence of times used in Figure 6.5(a). Examination of Figure 6.5(b) shows striking similarity between the qualitative behavior of the negative u_R region in the calculated images and the PLIF measured images in Figure 6.5(a).

The $\mathbf{E}\times\mathbf{B}$ drift is the dominant drift determining the direction of u_R. In a stationary potential the $\mathbf{E}\times\mathbf{B}$ drift is along potential contours. With $\mathbf{B}$ out of the page the drift is counterclockwise around potential valleys and clockwise around potential hills. In Figure 6.5(c) the probe measured plasma potential is displayed with arrows on the equipotentials to indicate the $\mathbf{E}\times\mathbf{B}$ flow. In the $m = 2$ drift-Alfvén waves the ion fluid is flowing in two pairs of counter-rotating vortices around the potential hills and valleys. As the entire mode structure rotates, the direction of the u_R components oscillate in the imaged plasma (compare Figure 6.5(a) and (b) with (c)).

Despite the agreement on the flow pattern between the PLIF measured field and the drift approximation, the magnitudes of the calculated velocities are often an order of magnitude larger than those actually measured. The discrepancies in the overall magnitude are not within the ~50% error inherent in the calculation. Initial attempts to include polarization terms, the convective derivative and the Alfvén character of the wave have not resolved this discrepancy in magnitudes.

6.3 PLIF Measured Ion Temperature Field

These data also represent the first time resolved *images* of the ion temperature field using LIF. The periodic spatial structure in the ion temperature field is the first observation of T_i oscillations ($\tilde{T}_i \sim 3eV$) coherent with the drift waves in Encore (see Figure 6.4 for images and Figure 6.6 for time history at a single point). The temperature oscillations are out of phase with the plasma potential. It should be pointed out that it is not a trivial matter to show that T_i *should* oscillate in the wave fields since the drift waves can be derived *without* temperature fluctuations (see Appendix A).

The mean ion temperatures $\langle T_i \rangle \approx 6eV$ are consistent with the stochastically heated values measured by McChesney ('87). The heating rate $\sim 10^4 eVs^{-1}$ is also in agreement with McChesney's measurements. An interesting feature of the temperature time history (Figure 6.6) is the sudden jump in T_i around $t = 370\mu s$. This could be the effect of the wave fields passing the stochastic heating threshold.

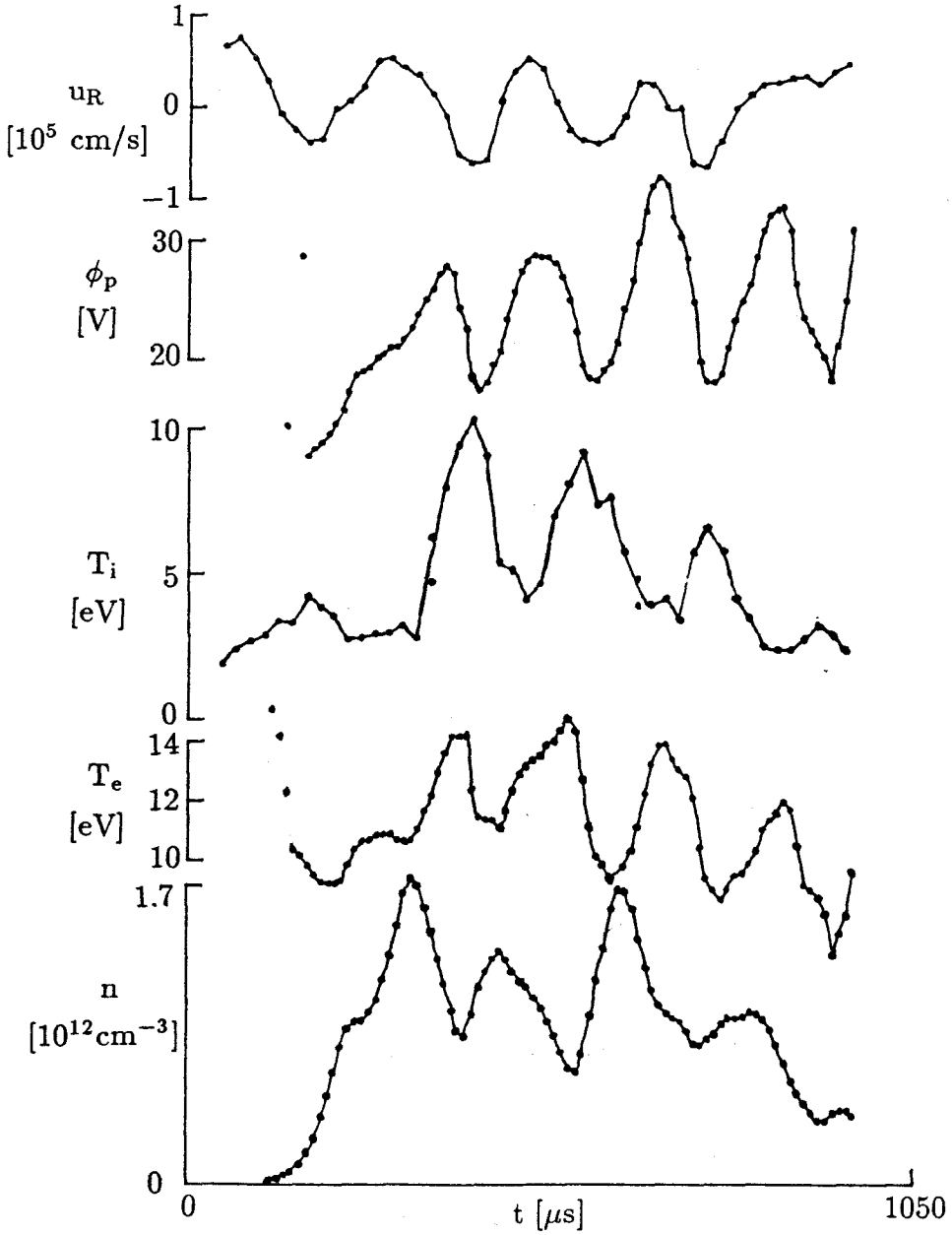

Figure 6.6 : Plasma parameters measured by PLIF and a Langmuir probe at one position in the plasma (see Figure 6.1).

6.4 Summary and Significance of PLIF Measurements

The plasma PLIF diagnostic system has been used to make the two-dimensional ion fluid velocity and temperature field measurements. Figure 6.6 (only 1/100 of the data) shows *measured* time histories of n, ϕ_p, T_e, T_i and u_R at a single position in the plasma. The PLIF and Langmuir probe data represent an extensive characterization of a nontrivial plasma. The Ar discharges in Caltech's Encore tokamak have a fortuitous blend of 'well understood' and 'previously unobserved' phenomena which continue to reveal new challenges for the experimentalist and theorist alike.

The drift waves in Encore were identified by comparing Langmuir probe measurements of wave frequency and fluctuating quantities to a two-fluid theory that assumed $T_i = 0$ (Fredrickson '85). McChesney ('87, '89, '91) studied the ion temperature using single point LIF and found the ions to be much hotter than expected. The ion heating observed in very low amplitude drift waves was attributed to stochastic ion motion in the drift wave. Now the ion fluid velocities and temperatures have been measured in large amplitude waves. Oscillations in both PLIF measured quantities are observed. Although the ion fluid flow field is qualitatively described by the ion fluid equation in the drift approximation, the magnitude of the predicted velocities is too large. To date there is no clear explanation of the fluctuations in T_i. They seem consistent with a conservative motion in the wave potential superimposed on a stochastically heated mean temperature. McChesney† has recently observed similar temperature oscillations in a Monte-Carlo code (McChesney '91) with wave amplitudes appropriate to this plasma.

The qualitative agreement between the calculations and the PLIF measurements, despite the stochastic dynamics, emphasizes the robust nature of the fluid

† private communication

equations as a description of the plasma. This might be expected since the waves were identified using a two-fluid model (Fredrickson '85). On the other hand the discrepancies between the PLIF measurements and the calculations highlight the need for a self-consistent treatment of the plasma. Moments of the ion distribution function are observed to differ with drift theory predictions in the wave: the temperatures are very high and have large oscillations in phase with the wave and the fluid velocity magnitudes are lower than predicted. Although stochasticity accounts for the high mean ion temperature, the collective effects due to the stochastic dynamics and large ion temperatures on the the fluid velocity and wave fields are unknown. The self-consistent problem may be avoided if one is willing to simply make the conjecture that since the fluid equations are derived from *integral* moments of the distribution function, it is unsurprising that they are insensitive to the existence of stochastic dynamics of particles in the bulk of the distribution. Rather than dismiss the problem in this way, an explicit connection between particle dynamics and distribution functions which shows promise in explaining the observations is explored in the next chapter.

7

SELF-CONSISTENCY AND STOCHASTICITY FROM A NEW VIEWPOINT

7.1 Introduction

The understanding of plasma physics would be very limited if a *complete* description of the plasma were needed to explain observed phenomena. By necessity and convenience a wide range of theoretical methods have been used to address the behavior of plasmas. Each approach is based on a set of approximations that simplify, obscure or ignore certain aspects of reality in order to shed light on the physics of interest. As the experimental work of this thesis has shown, it is often surprising how well some models work even though they ignore significant phenomena known to exist in the plasma.

This chapter will focus on the connection between *microscopic* particle behavior and *macroscopic* plasma parameters using two fundamental descriptions of the plasma: single particle orbits and the Vlasov equation. The first deals simply with the dynamics of a test particle described by the Lorentz equation in prescribed electric and magnetic fields. Important concepts and features of plasma behavior are revealed simply by calculating orbits for various electric and magnetic field topologies, e.g., drift motions and adiabatic invariants. However, for many (surprisingly simple) field choices the single particle dynamics exhibit stochasticity. A particular area where stochastic single particle dynamics has been important to the understanding of plasma behavior is ion heating in waves.

The Vlasov description of the plasma on the other hand, ignores single particles altogether and depends on the familiar concept of the continuous distribution

function f($\mathbf{x}, \mathbf{v}, t$) of the number of particles with spatial position $\mathbf{x}$ and (independently) velocity $\mathbf{v}$ at time t. Mathematically there is no airtight derivation of the Vlasov equation (Montgomery '71), but by accepting the distribution function, invoking conservation of particles, using only mean fields (due to external circuits and distant particles) and ignoring binary collisions, the standard Vlasov equation can be derived. The rigorous demands of mathematical proof seem insignificant compared to the overwhelming success of the Vlasov equation in describing plasma behavior. Velocity moments of the Vlasov equation are the primary equations used to describe macroscopic plasma phenomena. There are situations when the Vlasov equation and its moment equations *do not* provide sufficient insight into the physics underlying plasma observations, e.g., the anomalously hot ions and anomalously low fluid velocities in the Encore drift waves. In practice it is difficult to bridge the gap between the results of single particle models and measured macroscopic plasma parameters. Some of the arguments and experiments used to relate single particle dynamics to ion temperatures are described in Section 7.2 to provide background for the ideas presented in the rest of the chapter.

In Section 7.3 an *explicit* connection between the distribution function and particle orbits will be described. Such a relationship exists because the characteristics of the Vlasov equation are identical to the particle trajectories found by solving the Lorentz equation for the same mean fields. Possible implications of this new viewpoint will be described in Section 7.4 for a special case related to the drift waves in Encore. By considering the characteristics of the collisionless Vlasov equation, it can be shown that in stochastic regions of phase space, a self-consistent distribution function is restricted to being constant in that region. When the bulk of the ions are stochastic, the center of the distribution function is flattened, leading to higher ion 'temperatures' derived from Maxwellian fits. Although the

stochasticity affects the bulk of the distribution, the center and width of the envelope of the stochastic region and thus the fluid velocity and temperature oscillate periodically with the wave despite the nonperiodicity of the individual particle orbits. Suggestions for experimental verification of these predictions and further numerical work are also discussed.

7.2 Stochastic Particles in Plasmas

The stochastic dynamics of single particles have played an important role in the understanding of particle heating in plasmas. Most of the work has been theoretical or numerical in nature. Typically, the particle dynamics are investigated in simplified static and wave fields chosen to model a physical situation. This investigation usually involves analysis to isolate resonances which play a critical role in the stochasticity. Then the equations (sometimes a reduced set or a related mapping) are solved numerically and plotted graphically to visually determine parameters of interest and support hypotheses about plasma behavior.

One of the critical features of stochasticity is its abrupt appearance with a small change in some parameter in the dynamical equations. Zaslavskiĭ ('68) and Rechester ('79) discussed this 'stochastic instability' in the case of one traveling plane wave perturbed by another wave. Smith and Kaufman ('75, '78) were the first to point out the existence of stochastic dynamics of a particle in a *single* wave travelling oblique to a magnetic field. They proposed using an ion acoustic wave satisfying the stochastic criterion to heat the tail of an ion distribution. Interest in heating ions for fusion by waves propagating perpendicular to the magnetic field, i.e., propagating towards the center of a tokamak, motivated further research in the dynamics of particles in a single wave propagating across a static magnetic field.

Fukuyama ('77) studied the stochastic dynamics of ions in a plane monochromatic electrostatic wave exactly perpendicular to a static magnetic field near an ion cyclotron harmonic. Karney ('77, '78, '79) studied the same equations in more detail for lower hybrid wave ion heating at an arbitrary frequency above the cyclotron frequency. The same set of equations in different parameter limits (Drake '81, Malkov '84, McChesney '87, Zaslavskiĭ '89), magnetic fields with shear (Gell '80) and with relativistic effects (Karimabadi '90) have also been studied analytically, usually in relation to particle heating. Stochastic ion heating has also been observed in plasma simulations in a nonhomogeneous plasma (Abe '84).

In the theoretical studies, a connection between the stochastic dynamics of single ions in applied fields and the ion temperature is made heuristically. Convincing arguments based on intuition often appear in descriptions of how stochasticity *causes* heating and in justifying particular heating *models* based on knowledge gained from studying the stochastic dynamics. These phrases are typical: particles 'random walk' from resonance to resonance, "(w)e may then expect the particle to be able to move from the vicinity of one resonance to the vicinity of another" (Smith '75), it "should be expected that diffusion of phase points from a cell to another cell takes place" (Fukuyama '77), "qualitative picture suggested by" calculations in which "an ion whose velocity satisfies (a condition) moves stochastically, ranging over that portion of (phase space)" (Smith '78). Most authors then support their arguments with numerical results by calculating the trajectories of a number of particles and constructing ion distribution functions which do indeed show ion heating (8 ions in Smith '75, 10 in Fukuyama '77, 50 in Karney '78 and '79, 100 in Smith '78, 512 in Hsu '79, 10,000 in Abe '80, 200,000 in McChesney '91).

An alternative approach foreshadowing the results derived in Section 7.7 was used by Smith and Kaufman ('78). They attempted to determine the equilibrium ion distribution by modifying an initially Maxwellian *distribution function.* The following argument based on experience with the single particle dynamics was used: "The modification (of the distribution) is accomplished by successively considering semicircular annuli in $v_\perp v_z$ space, each of which represents particles with a small range of speeds. For each annulus the Maxwellian is *integrated over the stochastic portion* of the annulus to find the total number of stochastic ions in the annulus. This number is then *redistributed over the stochastic portion* of the annulus" (italics added, Smith '78). The idea is that the ions will spread themselves within a stochastic region *instantly* whenever they enter it. Since there are more particles with low velocities initially, the spreading quickly increases the number of particles with higher velocities, thereby heating the ions.

The focus in experimental work on stochastic heating has been to show three things in the experiment: 1) the temperatures are hotter with the wave than without the wave or hotter than expected, 2) the heating displays a threshold behavior with wave amplitude and 3) the heating is fast. Doveil ('81) measured stochastic electron heating in a standing wave. The unique capabilities of LIF have been successfully exploited to study stochastic ion motion with unprecedented detail. Stochastic ion heating has been observed in a number of plasma waves: ion Bernstein waves in an Ar linear magnetized plasma (Skiff '87a), drift-Alfvén waves in Encore (McChesney '87) and electrostatic ion cyclotron waves in a Ba Q-machine plasma (Skiff '88), all using LIF techniques. Unlike the theoretical work which ignores or argues away self-consistent effects, the experiments are by their nature self-consistent.

The experiments on the drift waves in Encore highlight the importance of stochastic particle dynamics within a plasma that can still be described using a relatively simple model. The waves in Encore were identified using a cold ion two-fluid model (Fredrickson '85) yet the ion temperatures are anomalously hot due to stochastic ion motion in the coherent waves (McChesney '87). The PLIF measured ion fluid flow pattern is qualitatively well described by the fluid equations, but not the magnitude of the velocities. The PLIF measurements also confirm the anomalously hot ion temperatures and add a previously unobserved large ion temperature oscillation to the Encore drift wave picture. The next two sections present an idea that may lead to a clearer understanding of how the complex ion dynamics and simple periodic behavior of the plasma are intertwined in a self-consistent way.

7.3 The Explicit Connection

The self-consistent relationships between stochastic single particle dynamics and macroscopic plasma parameters are not fully understood. One solution to this problem is to find a distribution function *consistent* with the fields that *cause* stochastic particle motion. The integral moments of such a distribution can then be used to find macroscopic plasma parameters. The idea is to begin with mean fields, study the dynamics of single particles in those fields, then *derive* a distribution function consistent with the fields using the dynamics, therefore insuring consistency with the stochasticity. If the distributions derived this way change significantly when the single particle dynamics change from being integrable to stochastic, then it can be concluded that the stochasticity *caused* the change in the distribution.

The simplifications in this approach are identical to those needed to derive the Vlasov equation.

$$\frac{\partial f}{\partial t} + \mathbf{v} \cdot \frac{\partial f}{\partial \mathbf{x}} + \frac{q}{m}(\mathbf{E} + \mathbf{v} \times \mathbf{B}) \cdot \frac{\partial f}{\partial \mathbf{v}} = 0 \tag{7.1}$$

A standard method for obtaining approximate solutions to the Vlasov equation for prescribed fields is the method of characteristics or integration over unperturbed orbits (Drummond '58, Sagdeev '58, Rosenbluth '58, see Swanson '89). In this technique the perturbation to an initial distribution function due to a wave is found by integrating the perturbation along *unperturbed* orbits which are presumably known analytically. This method is not accurate when the perturbed trajectories are qualitatively different from the unperturbed orbits, e.g., when there are effects of trapped particles in nonlinear Landau damping (O'Neil '65) or in situations where the perturbed orbits become stochastic.

The Vlasov equation is simply a statement that the distribution function is constant along its characteristics in phase space which correspond to particle orbits described by the Lorentz equation

$$\begin{aligned} \frac{d\mathbf{x}(t)}{dt} &= \mathbf{v}(t) \\ \frac{d\mathbf{v}(t)}{dt} &= \frac{q}{m}\{\mathbf{E}(\mathbf{x}, t) + \mathbf{v}(t) \times \mathbf{B}(\mathbf{x}, t)\}. \end{aligned} \tag{7.2}$$

If the distribution function $f(\mathbf{x}, \mathbf{v}, 0)$ is known at some time $t = 0$ and the characteristics are known, the Vlasov equation has effectively been solved because the value of the distribution function at time t can be found by tracing back the characteristic to $t = 0$; $f(\mathbf{x}, \mathbf{v}, t) = f(\mathbf{x}(-t), \mathbf{v}(-t), 0)$. A distribution function which satisfies the Vlasov equation can be constructed by setting the values of the distribution function in a plane transverse to the characteristics, essentially assigning a value to each characteristic. This is a generalization of the familiar statement

that any function of the constants of motion is a distribution function satisfying the Vlasov equation.

The errors inherent in integration over unperturbed orbits may be avoided if the exact orbits are calculated directly. In a system with well defined constants of motion, whole classes of characteristics lie on smooth surfaces in the phase space making the description of some distribution functions especially simple, i.e., functions of the constants of motion. In stochastic cases the phase space may not be foliated with such surfaces, but the characteristics can still be calculated by direct integration of Eq. 7.2. The problem remaining is to develop a way to understand what the distribution looks like once the characteristics are known.

The standard way of viewing the dynamics of single particle orbits is the Poincaré surface of section (Poincaré 1899, see Wiggins '90). Each time a particle trajectory passes through a chosen plane (transverse to the dynamic flow) in the dynamic phase space a point is plotted in the plane. Since a particle trajectory maps out a characteristic of the Vlasov equation, each point made on the surface of section by a single particle trajectory has the same distribution function value. The points in the surface of section found by following the particle for infinite positive and negative time make up a set of points in the plane which are invariant under a Poincaré map (a map of the plane to itself under the particle dynamics). Thus *invariant sets of a Poincaré map are level sets of the distribution function.* Invariant sets from integrable dynamics often appear as curves in Poincaré surface of sections, manifestations of the 'constants' of motion. On those curves in phase space the value of a distribution function satisfying the Vlasov equation is constant. Thinking of the distribution function as an altitude function over the surface of section plane, Poincaré surface of section plots provide unmarked 'topographic maps' of the distribution function consistent with the prescribed fields. The maps

are unmarked because *any* choice of constants on the characteristics will satisfy the Vlasov equation by construction.

This *explicit* connection between Poincaré maps of the particle dynamics and the distribution function consistent with prescribed fields follows from the following observations:

1. A distribution function consistent with prescribed fields is invariant on the characteristics of the Vlasov equation.
2. Single particle orbits in the prescribed fields are identical to the characteristics of the Vlasov equation.
3. Invariant sets of a Poincaré map may be constructed by following a single particle trajectory in the prescribed fields.

Therefore,

Invariant sets of a Poincaré map are level sets of distributions consistent with the prescribed fields.

This interpretation of the Poincaré map gives new significance to a surface of section plot as a window onto the physical world and not only as a geometric display of the mathematical dynamics. If the axes of a Poincaré section are chosen to be easily interpreted physically, i.e., velocities or positions rather than variables constructed purely for mathematical purposes, a Poincaré plot can be viewed with a distribution function as well as stochastic dynamics in mind. The missing link to make this picture truly self-consistent is to determine the values of the distribution function in a given plane which not only satisfy Vlasov's equation, but also Maxwell's equations with the *same* fields. The Poincaré map shows where the distribution values must be the same, but it does nothing to set those values. Further discussion on this point will be postponed until the end of the chapter. First, the implications of this new viewpoint are explored for a particular case

relying on the assumption that *the* self-consistent velocity distribution is similar to a Maxwellian; it has large values for small speeds and decreases monotonically to zero at large speeds.

7.4 Implications for a Model of the Drift Wave

Consider the fields of a monochromatic plane electrostatic wave propagating perpendicular to a uniform magnetic field.

$$\mathbf{B} = \mathrm{B}\hat{\mathbf{z}} \quad \mathbf{E} = \tilde{\phi}\mathrm{k}\sin(\mathrm{ky} - \omega\mathrm{t})\hat{\mathbf{y}}$$

This is a simplification of the drift-Alfvén wave in Encore which is a mostly electrostatic wave propagating perpendicular to the mostly toroidal magnetic field in a torus with poloidal mode number m = 2.

The perpendicular equations of motion (from Eq. 7.2) can be simplified to

$$\dot{\mathrm{q}} = \mathrm{p}, \quad \dot{\mathrm{p}} = -\mathrm{q} + \alpha\sin(\mathrm{q} - \nu\mathrm{t}) \tag{7.3}$$

where time and space have been shifted to eliminate initial conditions and normalized to ω_c and k respectively. The ratio of the characteristic frequencies is $\nu = \omega/\omega_c$, the normalized wave amplitude is $\alpha = \mathrm{k}^2\tilde{\phi}/\omega_c\mathrm{B}$ and in normalized units $\mathrm{v_x} = \mathrm{q}$ and $\mathrm{v_y} = \mathrm{p}$. For parameters relevant to the drift waves in Encore $\nu \approx 0.5$, $\alpha \approx 1$. Many of the authors referenced in Section 7.2 studied the stochastic dynamics of these equations for the cases when $\nu \gg 1$ and/or $\alpha \gg 1$. Some aspects of the nonlinear behavior of these equations for $\nu < 1$, $\alpha > 1$ have been studied by Forslund ('71, '72), Drake ('81) and McChesney ('87). Despite the physically significant nature of the situation described by these equations, there has not been a clear analytic treatment of the transition to chaos for the $\nu \leq 1$, $\alpha \lesssim 1$ case which includes the the drift waves in Encore. As the normalized wave

amplitude α increases to ~ 0.7 the dynamics become stochastic in a large region of phase space near $(q, p) = (0, 0)$.

To construct the Poincaré sections displayed in this thesis, eight particle trajectories are found by directly integrating Eq. 7.3 on a computer for $\lesssim 1000$ wave periods ($\sim$ 15min on a 25MHz PC486). Before choosing the plane to display the Poincaré section, the dimension of the phase space must be extended by a phase space variable which contains the time. Two Poincaré section plots in the $q = 0$ plane in the $(q, p, \theta = \nu t)$ phase space are displayed in Figure 7.1 and Figure 7.2 for two values of α. In these plots θ is the phase of the wave. From the viewpoint set out in the last section, the 'curves' in the Poincaré section are level sets of a distribution function $f(q = 0, p, \theta)$ or equivalently $f(v_x = 0, v_y, \theta)$. When $\alpha > 0$ but below the stochastic threshold, particle heating is not expected. The level sets are smooth curves in the plane (see Figure 7.1). For α above threshold when heating is expected, low velocity particles with stochastic trajectories map out invariant sets which intersect large areas in the phase plane (see Figure 7.2). Although this fact alone does not directly imply heating, a firmer connection between stochasticity and heating can now be made without resorting to a plasma simulation or Monte-Carlo program. This viewpoint also has implications for other macroscopic plasma parameters.

Plausible distributions derived by interpreting the Poincaré maps of the dynamics of single particles with a 'Maxwellian' distribution model are easily drawn for $\alpha = 0.4$ (see Figure 7.1). A 1eV Maxwellian was used to label the characteristics for $\theta = \pi$. This fixes the distribution in the rest of the phase space. The peak of the distribution function oscillates periodically with the wave, implying the 'fluid velocity' also oscillates periodically. The width of the distribution is also broadened in various phases of the wave (see $\theta = 5\pi/8$ in Figure 7.1).

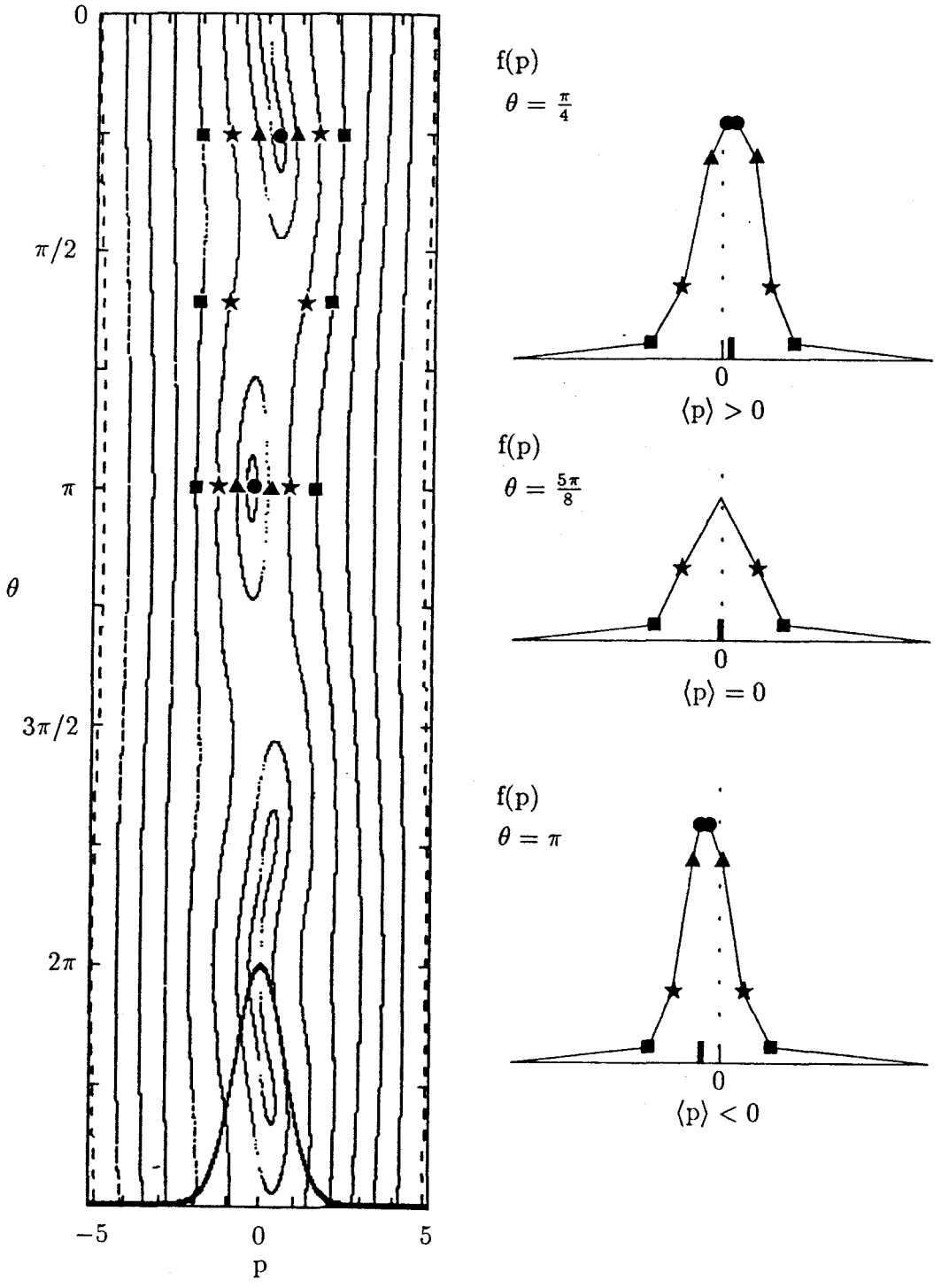

Figure 7.1 : Poincaré section in q = 0 plane for $\alpha = 0.4$ with $\nu = 0.4567$. Each symbol marks a crossing of a single particle in the wave phases corresponding to the unnormalized distribution functions. A normalized Maxwellian corresponding to 1eV is plotted on the Poincaré section for perspective.

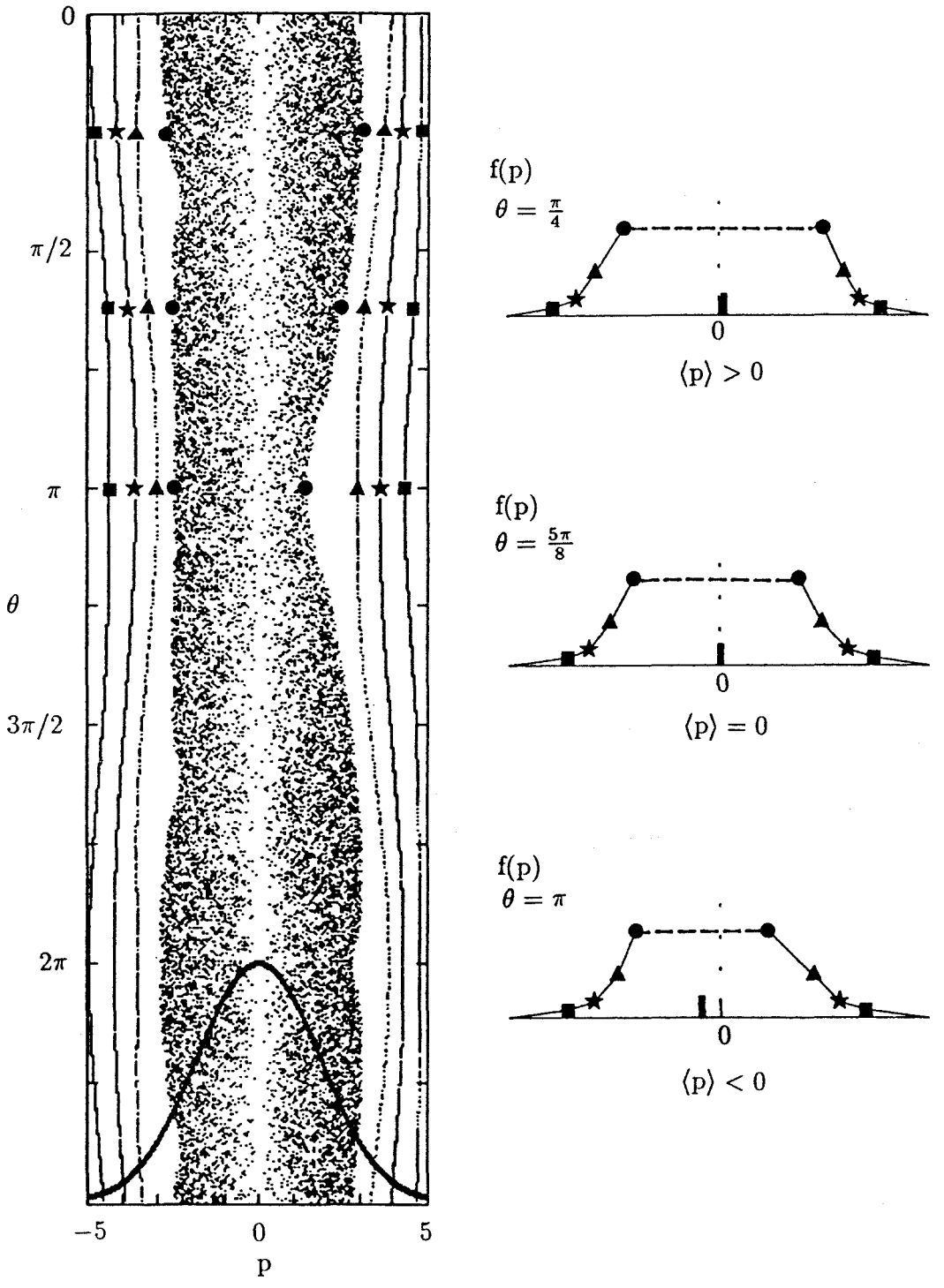

Figure 7.2 : Poincaré section in q = 0 plane for $\alpha = 0.95$ with $\nu = 0.4567$. Each symbol marks a crossing of a single particle in the wave phases corresponding to the unnormalized distribution functions. A normalized Maxwellian corresponding to 6eV is plotted on the Poincaré section for perspective.

It is less clear how to draw distributions in the case when α is above the stochastic threshold (see Figure 7.2). Due to the complicated, intertwined characteristics in the stochastic region, the distribution function would become discontinuous if each characteristic were given a different value. Experimentally this implies that any finite bandwidth measurement in that region of phase space would result in a single averaged value (assuming the stochastic region was evenly covered by the different level sets). If a discontinuous distribution seems unacceptable on grounds of physical intuition, the values assigned to these intertwined stochastic characteristics must be *identical* to ensure continuity. To maintain continuity from the nonstochastic regions, the value chosen must equal that of the 'last' integrable characteristic. Both arguments lead us to postulate a distribution function with a flat central region, essentially a broadened distribution. In Figure 7.2 a normalized 6eV Maxwellian distribution was used to set the values of the level sets at $\theta = 5\pi/8$. Once again, this choice determines the distribution in the rest of the phase space. Since the stochastic region spans all phases of the wave, this increased *temperature* is qualitatively different from the phase dependent broadening below the stochastic threshold.

Since it is the appearance of the stochasticity that leads to distribution functions with flat central regions in all phases of the wave, it is appropriate to say the heating is *caused* by stochasticity. From this viewpoint the heating does not depend on an irreversible transfer of energy from the wave to the particles via collisions or other irreversible phenomenon. The Poincaré maps are *only* valid for steady state.† Rather, these arguments lead one to propose that in order to have a large amplitude monochromatic wave propagating perpendicular to a constant

† The dynamics with a time dependent frequency and/or amplitude may be completely different (Wiggins '90).

magnetic field it is *necessary* that the distributions be broad. It is a misconception that the ions can be cold in large amplitude waves.

As Figure 7.2 shows, the envelope of the stochastic region continues to oscillate periodically with the wave. The width (temperature) and the 'center' (fluid velocity) of the envelope still oscillate in phase with the wave despite large stochastic regions of phase space. The existence of nonperiodic particle trajectories never excluded the existence of periodic fluid motion, but these arguments show how they are related. The exact nature of the oscillations of the envelope depend critically on ν. When $\nu = 1/n$ very strong resonant structures appear in the Poincaré maps. None of these features appear in the simple $\mathbf{E} \times \mathbf{B}$ plus polarization drift approximation.

The drift approximation of the ion velocities in the same fields were discussed in Chapter 2. It was shown that the the polarization drift in the y direction diverges to infinity as α approaches one. The fluid velocities expected using the Poincaré maps (see Figure 7.1 and Figure 7.2) are quite small; $\langle p \rangle \approx 1$ which corresponds to $\langle v_y \rangle \approx \omega_c/k$. This disparity between the drift picture and the single particle dynamics is reminiscent of the over-estimation of the fluid velocity magnitudes by the drift approximation used to describe the PLIF measurements. Although these results are promising, they do not explain the measurements quantitatively. The experimental results presented in this thesis are not directly comparable with this model due to the inherent integration over two velocity components performed by the PLIF measurement and the limitations of using a three instead of seven-dimensional phase space.

Some insight into the full distribution can be gained from this viewpoint by looking at Poincaré maps in the extended phase space (q, p, ψ) where $\psi = q - \nu t$ is the wave phase. In this case the level sets of the distribution $f(p, q)$ corresponding

to $f(v_x, v_y)$ may be displayed in any phase of the wave by constructing the Poincaré plot in the $\psi = \psi_o$ plane. Figure 7.3 and Figure 7.4 show series of plots in eight phases of the wave for the same particles and values of α and ν used in Figure 7.1 and Figure 7.2. Thinking in terms of unmarked topographical maps, as α increases, the 'summit' of the distribution changes from a single oscillating peak for very low α (not pictured) to a complicated set of 'rolling hills' for intermediate α (Figure 7.3) to a 'stochastic mesa' for α near one (Figure 7.4). Since the exact distribution value for each level surface is not known and the fluid velocity requires the first velocity moment of the distribution, it is difficult to predict the fluid velocity at each phase. It is clear that this is not the standard drift picture.

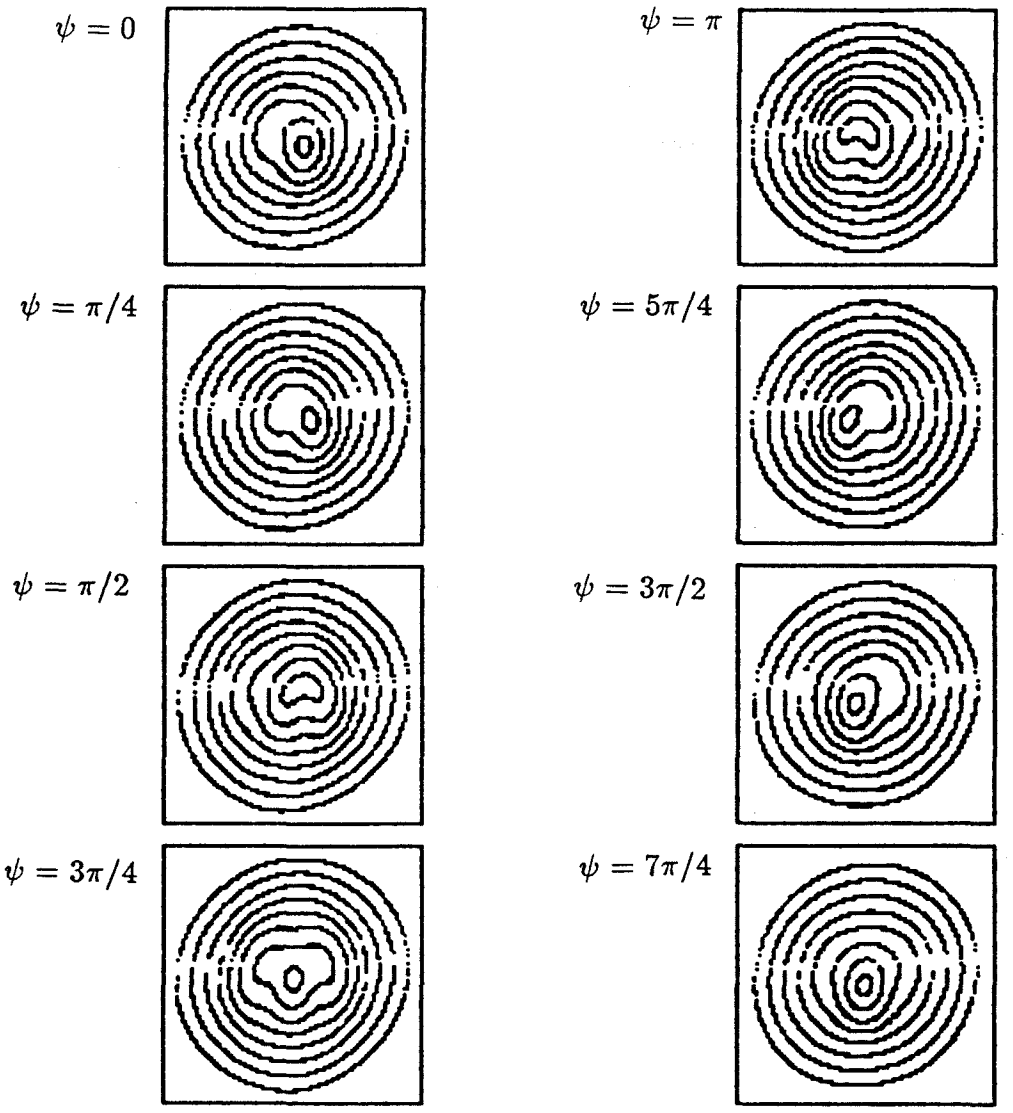

Figure 7.3 : Poincaré sections in constant ψ planes for $\alpha = 0.4$ with $\nu = 0.4567$. Each box is 5 units square centered on the (q,p) origin.

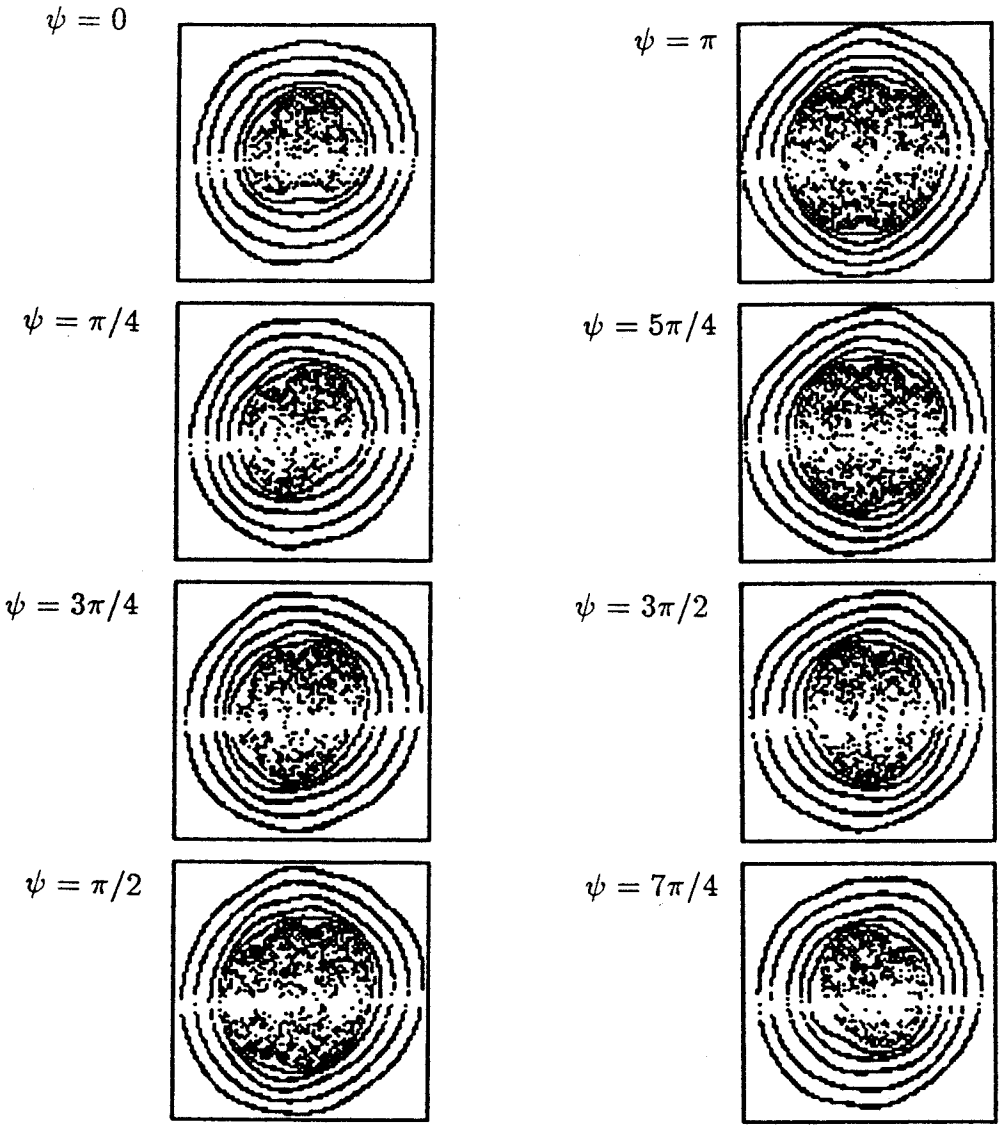

Figure 7.4 : Poincaré sections in constant ψ planes for $\alpha = 0.95$ with $\nu = 0.4567$. Each box is 5 units square centered on the (q,p) origin.

Further work is required to ascertain whether a distribution with the level sets constructed using a Poincaré section can also satisfy Poisson's equation. An iterative approach starting with the perturbed distribution calculated using integration over unperturbed orbits may provide a self-consistent solution to a basic plasma physics problem: what is the distribution consistent with a monochromatic wave traveling perpendicular to a constant magnetic field?

A computer program to calculate and label the characteristics for a desired phase space resolution is not difficult to imagine. Once the phase space is divided by labeled characteristics, the velocity moment integrals would be numerically trivial and could be compared to the Maxwell's equations for self-consistency. If the initial levels are not self-consistent, a choice must be made to relabel the characteristics. It is not clear if this step can be made with an analytic formula. It is also not clear that a self-consistent choice for the values necessarily exists. These questions must be left for the future.

A tagging experiment can be designed to measure $f(v_x = 0, v_y, \theta)$ from which level curves directly comparable to Figure 7.1 and Figure 7.2 could be calculated. The idea is to tag a zero velocity class of ions with a laser in one direction then search for the tagged class of particles with laser tuned to an arbitrary velocity class *perpendicular* to the tagged beam. Consider exciting the transition $3d'\,^2G_{7/2} \rightarrow 4p'\,^2F^o_{7/2}$ with a narrow linewidth, *horizontal* laser beam with $\lambda_{tag} = 6123$Å. A fraction of the excited ions will decay directly to another metastable $3d'\,^2G_{9/2}$.† After firing the tag laser, the $3d'\,^2G_{9/2}$ distribution will have an increased number of particles with *zero horizontal* velocity, v_R. Next a second, narrow linewidth, *vertical* laser in resonance with the $3d'\,^2G_{9/2} \rightarrow 4p'\,^2F^o_{7/2}$ transition ($\lambda_{search} =$

† It is shown in Appendix B that pumping this transition is the most effective way to tag the $3d'\,^2G_{9/2}$ state.

6115Å) for an arbitrary velocity class v_z is fired. The brightest line to monitor the search LIF is the $4p'\,^2F^o_{7/2} \rightarrow 4s'\,^2D_{5/2}$ transition with $\lambda_{LIF} = 4610$Å.† The difference between the LIF signal measured when the tag laser is fired and when it is not is a measure of the number of particle with zero horizontal velocity and vertical velocity v_z. By scanning the wavelength of the search laser the distribution function $f(v_R = 0, v_z)$ can be measured. If the diagnosed point is in the edge of the plasma on the tokamak midplane (see Figure 7.5), the wave vector will be vertical and $f(v_R = 0, v_z)$ will be nearly equivalent to $f(q = 0, p)$ in the Poincaré maps in Figure 7.2 and Figure 7.3.

† Since the tagging laser induces fluorescence at the search LIF wavelength, the signal analysis for the tagging scheme presented above is most straight forward if the search laser is fired *after* the tag laser LIF is over ($\sim$ 10ns). If it is found that the population of the $3d'\,^2G_{9/2}$ state far exceeds the $3d'\,^2G_{7/2}$ population the above tagging scheme may be reversed to increase tagged population. The efficiency of tagging in the reversed direction ($\Xi_B = 0.009$) is $\sim$ 100 times less effective than in the other direction (see Appendix B).

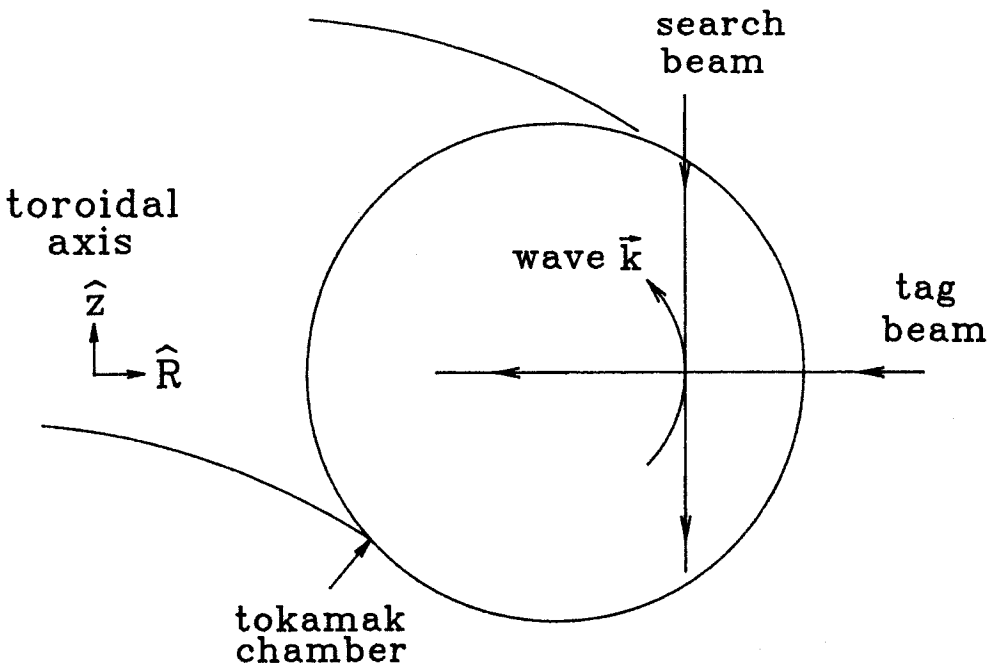

Figure 7.5 : Schematic of crossed beam tagging experiment designed to test the implications of the theoretical viewpoint.

8

SUMMARY AND CONCLUSIONS

The development of the first plasma PLIF diagnostic system has been described in this work. The diagnostic was used to make time resolved two-dimensional images of fluorescence excited in a poloidal cross section of Caltech's Encore tokamak. A significant fraction of the PLIF from an Ar plasma discharge is filtered and imaged by a carefully designed optical system. PLIF signals from a gated, 10x10 anode, microchannel plate photomultiplier due to hundreds of detected photons per anode are measured each discharge. PLIF presents new opportunities for imaging plasma parameters without losing the nonintrusive, high resolution (spatial, velocity and temporal), easily interpreted aspects of single point LIF measurements.

Ion fluid velocity field measurements in two spatial dimensions were made by imaging PLIF excited by a narrow linewidth laser in resonance with a Doppler broadened absorption line from an Ar metastable ion. The Encore discharges were dominated by reproducible, large amplitude, coherent, drift-Alfvén waves with poloidal mode number m = 2. Spatial structures in the field of the measured fluid velocity component were found to oscillate coherently with the wave. Ion fluid flowing with peak speeds $\sim 10^5$cm/s in the $\mathbf{E}\times\mathbf{B}$ direction around the potential hills and valleys of the rotating m = 2 potential of the drift wave reproduces the behavior of the PLIF measured structures in the fluid velocity field. Probe and PLIF measurements of plasma parameters were used to calculate the fluid velocity field predicted by the drift approximation in the ion fluid equation of motion. Although a two-fluid theory (Fredrickson '85) explains the frequency and phases of the oscillating plasma parameters in the drift wave, the magnitudes of

the ion fluid velocities predicted by the drift approximation are nearly an order of magnitude larger than the measured values even though the predicted flow pattern is well described by the approximation. It was shown that dropping the convective derivative in the drift approximation required that the normalized wave amplitude $\alpha \equiv k^2\tilde{\phi}/B\omega_{ci} \ll 1$. Since this is not the case for these large amplitude drift waves ($\alpha > 1$), it is surprising that the drift approximation works at all. The agreement with the measured flow pattern may explain why the approximation can still be used to derive the gross features of the wave.

The first measurements of the ion temperature field in two dimensions were also made in the same discharges using PLIF. The ion temperatures were found to be very high $\langle T_i \rangle \approx 6eV$. This is consistent with previous work (McChesney '87) which showed that stochastic ion motion in coherent drift waves with $\alpha > 0.6$ is responsible for the anomalously hot ion temperatures observed in Encore. Ion temperature fluctuations were also observed for the first time in the drift waves in Encore. The temperature field displayed an oscillating spatial structure similar to the ion fluid velocity field out of phase with the plasma potential. The PLIF observations extend and complement the Langmuir probe measurements of the plasma potential, density and electron temperature, providing the most detailed picture of the coherent drift waves in Encore to date.

Although the PLIF system can also be used to make metastable density measurements, it was shown that the metastable ion density is not directly proportional to the bulk ion density for the plasma parameters in Encore discharges. A simple model including the dominant metastable production and quenching reactions showed that the metastable population is very sensitive to both the electron density and temperature. Comparison of PLIF measurements with probe data

confirmed the conclusion that the metastable ion density is not easily interpreted in terms of other plasma parameters.

The importance of the normalized wave amplitude α in both the drift approximation and the stochastic ion heating prompted a reexamination of the ion dynamics in a simple model of the wave fields. This led to a new approach for understanding the relationship between stochastic single particle dynamics and macroscopic plasma parameters. An *explicit* connection between the ion distribution function and Poincaré maps of the single particle dynamics in prescribed mean fields was made by considering the characteristics of the collisionless Vlasov equation. This new viewpoint shows how stochasticity broadens distribution functions by constraining the distribution function to be constant in stochastic regions of phase space. It also extends the use of Poincaré maps as a visual tool to study (and possibly calculate) the distribution functions consistent with the particle dynamics. Initial results show the promise of integrating the observations of hot, oscillating ion temperatures and periodic fluid velocities lower than predicted by standard approximations.

There are still many avenues which may be explored using the PLIF diagnostic and the theoretical framework presented in this thesis. A number of possible experimental refinements of the PLIF system have been discussed in the text. The problems involved in making a single shot broad linewidth PLIF density diagnostic may not be insurmountable. Interesting observations could be made in a plasma of turbulent drift waves (in Encore the drift waves become turbulent when the plasma current is increased to $\sim$1.7kA). The possibilities for PLIF tagging experiments have not yet been attempted, e.g., tag with a laser beam and image the search PLIF excited with the laser sheet. Although previous tagging experiments in Encore were hampered by the short lifetime of the tagged particles due to electron

collisions (McChesney '91), a new tagging scheme discussed in Appendix A may have a long enough tagging lifetime to study stochastic ion trajectories in Encore.

The implications of the theoretical viewpoint presented here may be tested by the crossed beam tagging experiment described in Chapter 7 which would measure distribution functions with one velocity component equal to zero. Results from such an experiment could be compared with the Poincaré maps of the dynamics of the particles as the drift wave potential is increased. On the analytic side, the critical step missing from the theory is an algorithm for choosing the distribution function satisfying Vlasov's equation which *also* satisfies Maxwell's equations.

As the measurements in the plasma become more detailed, the theoretical models needed to describe the physics become more constrained. For the plasmas in Caltech's Encore tokamak these measurements force consideration of fundamental questions in plasma physics. Why are the fluid equations such a robust description of the plasma even when significant phenomena are ignored? Given the fact that microscopic particle dynamics affect macroscopic plasma parameters, how can these dynamics be included in a description of the plasma? Undoubtedly these questions will continue to stimulate work in plasma physics in the foreseeable future.

Appendix A

DRIFT-ALFVÉN WAVE DISPERSION

The drift wave is a nearly electrostatic wave which propagates in the electron diamagnetic direction. Because the wave does not propagate exactly perpendicular to the magnetic field, it is coupled to the Alfvén wave by the magnetic fluctuations due to the currents in the wave along the magnetic field.

In this derivation based on Kadomtsev ('65), the wave is assumed to be driven by a density gradient in only the x direction $\partial n/\partial x \neq 0$, $\partial n/\partial y = \partial n/\partial z = 0$, the magnetic field is constant $\mathbf{B} = B\hat{\mathbf{z}}$, $T_i = 0$, T_e is constant, the wave frequency is much less than the ion and electron cyclotron frequencies $\omega \ll \omega_{ci}, \omega_{ce}$, the plasma is quasineutral $n_i = n_e = n$, the small fluctuating quantities vary as $\exp[-i(\omega t - \mathbf{k}\cdot\mathbf{x})]$ and the wave propagates in only the y-z plane, $k_x = 0$. The coupling to magnetic fluctuations is incorporated by allowing the wave potential along the field $\tilde{\psi}$ to be different from that perpendicular to the field $\tilde{\phi}$

$$\tilde{\mathbf{E}} = -\frac{\partial\tilde{\phi}}{\partial y}\hat{\mathbf{y}} - \frac{\partial\tilde{\psi}}{\partial z}\hat{\mathbf{z}}.$$

Four steps are required to derive the dispersion.

1) $\tilde{B}_x$ and $\tilde{J}_z$ are written in terms of $\tilde{\psi}$ and $\tilde{\phi}$ using Faraday's and Ampere's laws.
2) $\tilde{n}_e$ and $\tilde{n}_i$ are written in terms of $\tilde{\psi}$ and $\tilde{\phi}$ using 1) and the two fluid equations of motion.
3) $\tilde{\psi}$ and $\tilde{\phi}$ are related through $\nabla\cdot\mathbf{J} = 0$ and 1).
4) The dispersion is found by using 3) in the expression for $\tilde{n}_e$ from 2) and invoking quasineutrality to set $\tilde{n}_e = \tilde{n}_i$.

Step 1

Faraday's law gives

$$\tilde{B}_x = \frac{ik_y k_z}{\omega}(\tilde{\phi} - \tilde{\psi})$$

and from the z component of the curl of Faraday's law using Ampere's law and $c^2 \ll \omega^2/k_y^2$

$$\tilde{J}_z = \frac{k_z k_y^2}{\omega \mu_o}(\tilde{\phi} - \tilde{\psi}). \tag{A.1}$$

Step 2

The solution to electron fluid equation of motion to zero-order gives the electron diamagnetic drift

$$\mathbf{u}_e = -\frac{T_e}{eB}\frac{\partial n_e/\partial x}{n}\hat{\mathbf{y}} \equiv v_D \hat{\mathbf{y}}$$

and to first-order shows the deviation from Boltzmann caused by the Alfvén character of the wave

$$\frac{\tilde{n}_e}{n} = \frac{e}{T_e}\left[\tilde{\phi} - (\tilde{\phi} - \tilde{\psi})(\frac{\omega_*}{\omega} - 1)\right] \tag{A.2}$$

where $\omega_* = v_D k_y$. Both these equations were derived from

$$m(\frac{\partial \mathbf{u}_e}{\partial t} + \mathbf{u}_e \cdot \nabla \mathbf{u}_e) = -e(\tilde{\mathbf{E}} + \mathbf{u}_e \times \mathbf{B}) - \frac{\nabla(n_e T_e)}{n}. \tag{A.3}$$

For this particular slab geometry the convective term $\mathbf{u}_e \cdot \nabla \mathbf{u}_e$ in the zero-order equation is identically zero. To arrive at the solution to the first-order equation (Eq. A.2) the z component of the left-hand side of Eq. A.3 was dropped compared to the remaining terms

$$m(\frac{\partial \tilde{u}_z}{\partial t} + v_D \frac{\partial \tilde{u}_z}{\partial y}) \ll -iek_z\tilde{\psi},\ ev_D\tilde{B}_x,\ -\frac{iT_e k_z \tilde{n}_e}{n}$$

which is equivalent to requiring

$$\frac{\omega}{k_z}\tilde{u}_z,\ \frac{\omega_*}{k_z}\tilde{u}_z \ll v_T^2\frac{\tilde{n}_e}{n}$$

where $v_T^2 = T_e/m$. Solving for $\tilde{u}_z$ directly gives

$$\tilde{u}_z = \frac{ek_z}{m_e(\omega_* - \omega)}[\tilde{\phi} - (\tilde{\phi} - \tilde{\psi})(\frac{\omega_*}{\omega} - 1) - \frac{T_e}{e}\frac{\tilde{n}_e}{n}]$$

which is zero *if* Eq. A.2 holds which implies the assumptions are valid. Thus Eq. A.2 and the assumptions needed to derive it are consistent. In the Encore plasma these assumptions are in general true, although it should be noted that they are not *necessarily* true uniformly or in all plasmas.

Since $T_i = 0$ and $\omega \ll \omega_{ci}$ are assumed, the first-order ion velocities are easily derived and used in the ion continuity equation to derive

$$\frac{\tilde{n}_i}{n} = -\frac{k_y\tilde{\phi}}{\omega B}\frac{\partial n/\partial x}{n} - \frac{k_y^2\tilde{\phi}}{\omega_{ci}B} + \frac{ek_z^2\tilde{\psi}}{m_i\omega^2}. \tag{A.4}$$

Step 3

From quasineutrality $\nabla \cdot J = 0$ which implies $\tilde{J}_z = -k_y\tilde{J}_y/k_z$ which can be written out explicitly in terms of ion and electron velocities giving (ignoring terms order ω_{ce}^2/ω^2, m_e/m_i and $m_eT_e\tilde{n}_e/m_ie\tilde{\phi}n$)

$$\tilde{J}_z = \frac{k_y^2\omega}{\mu_o v_A^2 k_z}\tilde{\phi} \tag{A.5}$$

where $v_A = (B^2/nm_i\mu_o)^{1/2}$ is the Alfvén velocity. Equating the expressions for $\tilde{J}_z$ (Eq. A.5 and Eq. A.1) gives $\tilde{\psi}$ in terms of $\tilde{\phi}$

$$\tilde{\phi} - \tilde{\psi} = \frac{\omega^2}{k_z^2 v_A^2}\tilde{\phi}. \tag{A.6}$$

Step 4

The last step is to use Eq. A.6 to eliminate $\tilde{\psi}$ in the equations for the densities (Eq. A.4 and Eq. A.2). Equating $\tilde{n}_e = \tilde{n}_i$, $\tilde{\phi}$ cancels and one is left with the dispersion

$$k_y^2\rho_s^2 + \beta = \frac{k_z^2c_s^2}{\omega^2} + (\frac{\omega_*}{\omega} - 1)(1 - \frac{\beta\omega^2}{k_z^2c_s^2})$$

where $c_s = (T_e/m_i)^{1/2}$ is the ion sound speed, $\rho_s^2 = c_s^2/\omega_{ci}^2$ and $\beta = nT_e\mu_o/B^2$. For $\omega_* \ll k_z v_A$, $\beta \ll 1$ and $c_s \ll \omega k_z$ the drift wave dispersion is obtained

$$\omega = \frac{\omega_*}{1+b}\left[1 - \left(\frac{\omega_*}{k_z v_A}\right)^2 \frac{b}{(1+b)^3}\right]$$

where $b = k_y^2\rho_s^2$.

For the drift waves to be unstable there must be a slight phase difference between the wave field and the density fluctuations. Collisions, electron Landau damping and/or a parallel electron drift may introduce this phase shift. In Encore the electron mean free path is longer than the distance the electrons need to travel along the field lines to move one parallel wavelength. Thus electron damping dominates collisions as a destabilizing effect in Encore.

Results obtained from a kinetic approach including a zero-order electron drift along the magnetic field v_{zo} may be used to compare the importance of Landau damping and the current to the instability.† The density gradient $n \sim \exp(-\beta x)$, constant magnetic field $\mathbf{B} = B\hat{\mathbf{z}}$, $\omega \ll \omega_{ci}, \omega_{ce}$ and the thermal velocities related to the wave phase velocity $v_{Ti} \ll \omega/k_z \ll v_{Te}$ are assumed in a magnetized collisionless Vlasov plasma. The real and imaginary parts of the plasma dielectric are derived by integration over unperturbed orbits.

$$\epsilon_r = 1 + k^2\lambda_{De}^2 - \frac{\omega_e^*}{\omega} - \left(1 + \frac{T_i\omega_e^*}{T_e\omega}\right)\left(\frac{k_z^2 c_s^2}{\omega^2} + \frac{k_y^2 c_s^2}{\omega^2 - \omega_{ci}^2}\right)$$

$$\epsilon_i = \pi^{\frac{1}{2}}\left[\frac{T_e}{T_i}\frac{(\omega - \omega_i^*)}{k_z v_{Ti}}\exp\left(-\frac{\omega^2}{k_z^2 v_{Ti}^2}\right) + \frac{\omega - k_z v_{zo} - \omega_e^*}{k_z v_{Te}}\exp\left(-\frac{(\omega - k_z v_{zo})^2}{k_z^2 v_{Te}^2}\right)\right]$$

where quantities are as defined earlier and $\omega_e^* = \omega_* = -\omega_i^* T_e/T_i$. The real part of the frequency ω_r is found by setting $\epsilon_r = 0$. The imaginary part $\omega_i \approx -\epsilon_i/(\partial\epsilon_r/\partial\omega)$

† These are my results from Prof. Bellan's 1988 plasma physics final exam.

($\omega_i > 0$ implies instability). For drift waves

$$\omega_r = \frac{\omega_*}{1+b}\left[1 + \frac{k_z^2 c_s^2}{\omega_*^2}(1+b)\right]$$

$$\omega_i \approx \frac{\pi^{\frac{1}{2}}\omega^2}{(1+b)k_z v_{Te}}\left[b + \frac{k_z v_{zo}}{\omega}\right].$$

In the expression for ω_i, the first term in the square brackets is from the Landau damping and the second from the current. For Encore parameters the term due to the current is approximately an order of magnitude larger than the Landau damping term.

Since the drift waves in Encore are primarily current driven, it is not surprising that the amplitude of the waves is somewhat controlled by the plasma current. For this work a fairly high plasma current ($I_p = 1.3kA$) was used in order to get very repeatable plasmas in the present configuration of Encore. The plasmas used by Fredrickson ('85) and McChesney ('87) to study the drift waves had some characteristics similar to the discharges used in this thesis, but there are also some differences. In light of the PLIF temperature measurements, the most important difference to note is that the plasmas used by McChesney ('87) to study the ion heating rates had much lower currents ($I_p \lesssim 300A$) and thus lower amplitude drift waves.

Appendix B

THE BEST ArII LIF AND TAGGING SCHEMES

B.1 Evaluating LIF Schemes

The *best* LIF scheme and the *best* optical tagging scheme for ArII are determined. A series of simplifying assumptions about the LIF and tagging processes is made which results in easily calculable figures of merit for the proposed schemes. The validity of these expressions is limited by the assumptions used in the derivation which primarily evaluates the relative importance of atomic parameters. The most serious limitation to applying these results in experimental situations is the assumption on the initial state populations. The discussion of metastable populations in Chapter 4 makes it clear that prediction of state populations is in general a very difficult problem to which the only sure solution is experimental data. These results should be considered as guidelines for future LIF choices.

To achieve easily detectable LIF signals the pumped state must be highly populated compared to the upper state. The ground and metastable states of an atomic species are expected to have large populations and are good LIF candidates. Since the transitions from the ground states of ArII have wavelengths too short for optical lasers, only the metastable and very long-lived states of ArII will be considered as pump states. These states will be referred to collectively as metastables without distinction. Since all the metastables are in the 3d level of ArII and the radiative lifetimes of the upper states are short compared to electron-ion collisional times ($\tau_{\text{life}} \sim 10\text{ns} \ll 10\mu\text{s} \sim \tau_{\text{col}}$), it is assumed at t = 0 all the upper states are empty. For simplicity the metastables are assumed to be populated in proportion to their statistical weights $n_i(0) = g_i n_0$. All possible LIF

schemes based on these states can be read from Table B.5 by simply choosing an upper state u and then a pair of lower states radiatively connected to u.

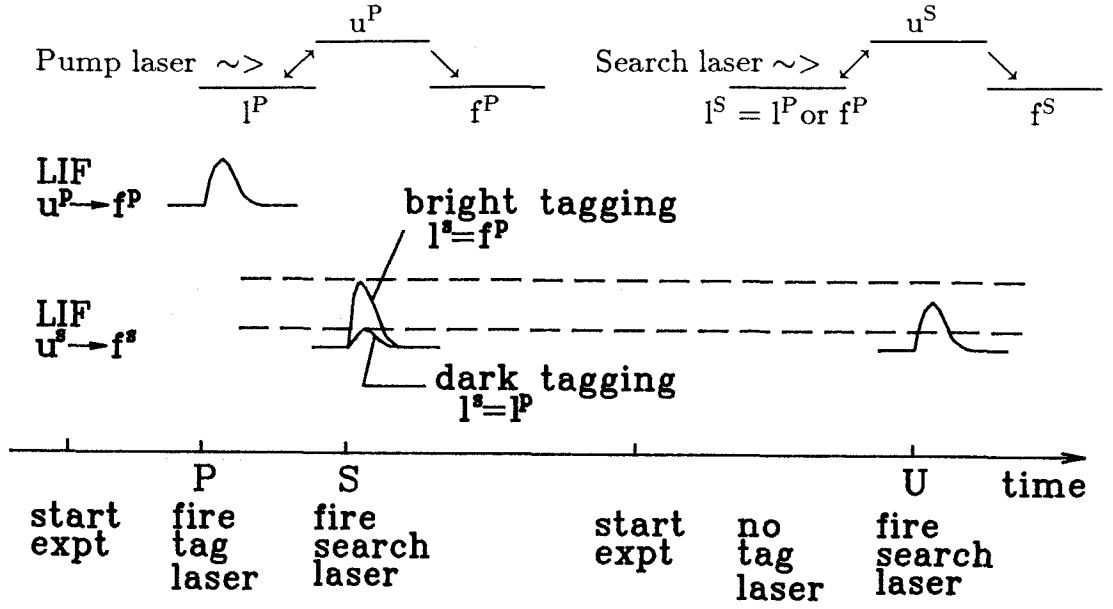

Figure B.1 : Tagging scenario and simplified energy level diagram displaying notation.

Optical tagging is a three-step process. Each step involves a lower state l and a final state f both radiatively connected to a single upper state u (see Figure B.1). The transition $l^P \rightarrow u^P$ is pumped by a laser at time t = P. This reduces the population in l^P and increases the population of the other states f^P radiatively connected to u^P. These modifications of the initial state populations *tag* the class of ions resonant with the exciting laser. At a later time t = S LIF from a search laser tuned to a transition from one of the tagged states $l^S \rightarrow u^S$ is detected (l^S is either l^P or f^P). Tagging depends on comparing the tagged LIF signal, measured at t = S, to an untagged LIF signal from the same transition measured at time t = U equivalent to t = S in terms of all other experimental parameters, e.g., wave

phase. The difference in the two signals is a measure of the tagged population. In a *dark* signal tagging scheme the pump and search lower states are identical $l^P = l^S$ and a reduction in LIF signal is expected. In a *bright* tagging scheme the final pump state and the lower search state are the same $f^P = l^S$ (assumed metastable) and an increased LIF signal is expected.

The lasers are assumed powerful enough to saturate any transition instantly and maintain saturation during the pulse lengths $\Delta t_{las} = \theta_T$ where T denotes the laser at time t = P, S or U. The radiative lifetimes of the upper states and the laser pulse lengths are assumed much shorter than the proposed tagging time $\Delta t_{tag} = S - P = \Theta$. Allowing the upper state population to decay to zero, the population of the lower state n_l and the LIF photons n_{LIF} after a laser pulse may be calculated by solving the appropriately simplified semi-classical model equations presented in Chapter 4.

$$\begin{aligned} n_l(T) &= \frac{n_l(t < T)(1 + g_{ul}A_{ul}\tau_u)}{(1 + g_{ul})} \exp\left(-\frac{\theta_T}{(1 + g_{lu})\tau_{oth}}\right) \\ &\equiv [1 - \xi]n_l(t < T) \\ n_{LIF}(T) &= A_{uf}\tau_{oth}\Big[n_l(t < T) - n_l(T)\Big] \\ &= A_{uf}\tau_{oth}\xi n_l(t < T) \end{aligned} \tag{B.1}$$

where time T = P, S or U, $\tau_{oth} = (\tau_u^{-1} - A_{ul})^{-1}$ is the lifetime of state u for decay to states other than l, $g_{ji} = g_j/g_i$ the ratio of statistical weights, and ξ, as defined above, is the efficiency of pumping the population out of state l. If state f is a metastable then $n_{LIF}(T)$ is also the additional population pumped into that state.

For untagged LIF Eq. B.1 gives an expression proportional to the detectable LIF and can be used to define a figure of merit for a proposed LIF scheme

$$\Xi_L \equiv n_{LIF}/n_0 = A_{uf}\tau_{oth}\xi g_l. \tag{B.2}$$

If A_{uf} is replaced by A_{ul}, Eq. B.2 is proportional to the LIF signal at the exciting laser wavelength. The dependence of Eq. B.2 on g_l is due to the linear dependence of the LIF signal on the initial lower state population. The best LIF scheme for each lower state using $\theta_U = 20$ns is shown in Table B.1. Ξ_L is a measure of the efficiency of pumping the population out of state l (ξ term) via the u $\rightarrow$ f transition ($A_{uf}\tau_{oth}$ product). The fraction of the initial metastable population that produces LIF photons Ξ_L/g_l is also shown in Table B.1. If the actual metastable populations n_m are known, $n_m\Xi_L/g_l$ would be used as the figure of merit to compare various schemes. The repeated appearances of the $4p'\,^2F^o_{7/2} \rightarrow 4s'\,^2D_{5/2}$ and $4p\,^4D^o_{7/2} \rightarrow 4s\,^4P_{5/2}$ LIF lines are due to the fact that both transitions have high transition probabilities compared to all the transitions and also much higher probabilities than any other transition from the given upper state. This means that any ion pumped from a metastable to one of these upper states is not only very likely to decay to a different final state, but is also most likely to decay via the above transitions.

The LIF scheme used on Encore $3d'\,^2G_{9/2} \rightarrow 4p'\,^2F^o_{7/2} \rightarrow 4s'\,^2D_{5/2}$ with $\Xi_L = 5.7$ was chosen by experimental comparison of LIF signals from a couple schemes. It can be seen in Table B.1 there are two schemes which have larger Ξ_L. Neither scheme has been proposed before. The scheme based on the $3d\,^4D_{7/2}$ state is experimentally difficult with the current laser system due to the pump laser wavelength. But the $3d\,^4F_{9/2} \rightarrow 4p\,^4D^o_{7/2} \rightarrow 4s\,^4P_{5/2}$ scheme has laser wavelength and detector requirements similar to the current scheme and could give $\sim 24\%$ increase in signal.

l	λ_{las} [Å] →	u	λ_{LIF} [Å] →	f	Ξ_L	Ξ_L/g_l
$3d\,^4D_{7/2}$	4014	$4p\,^4D^o_{7/2}$	4348	$4s\,^4P_{5/2}$	7.3	0.91
$3d\,^4D_{5/2}$	4039	$4p\,^4D^o_{7/2}$	4348	$4s\,^4P_{5/2}$	4.3	0.72
$3d\,^4D_{3/2}$	4461	$4p\,^4P^o_{5/2}$	4806	$4s\,^4P_{5/2}$	2.6	0.65
$3d\,^4D_{1/2}$	4352	$4p\,^4P^o_{1/2}$	4806	$4s\,^4P_{3/2}$	1.5	0.75
$3d\,^4F_{9/2}$	6644	$4p\,^4D^o_{7/2}$	4348	$4s\,^4P_{5/2}$	6.5	0.65
$3d\,^4F_{7/2}$	6687	$4p\,^4D^o_{7/2}$	4348	$4s\,^4P_{5/2}$	5.6	0.70
$3d\,^2F_{7/2}$	4682	$4p'\,^2F^o_{7/2}$	4610	$4s'\,^2D_{5/2}$	4.4	0.55
$3d'\,^2G_{9/2}$	6115	$4p'\,^2F^o_{7/2}$	4610	$4s'\,^2D_{5/2}$	5.7	0.57
$3d'\,^2G_{7/2}$	6123	$4p'\,^2F^o_{7/2}$	4610	$4s'\,^2D_{5/2}$	4.4	0.55

Table B.1: The best LIF scheme for each lower state in ArII. Metastables are in boldface.

Continuing the analysis of the tagging schemes, detection of tagged signals depends on the persistence of the tagging effect. Tagging is often used to track a class of particles from one spatial position to another. For Encore parameters a tagging time long enough to follow a thermal ion a distance comparable to the minor radius would be desirable, $\Theta \approx a\,v_i^{-1} \approx 50\mu s$. Assuming all the tagged particles remain together spatially, estimates for tagging persistence times can be made.

Dark tagging is limited by the repopulation of the *emptied* metastable state l^P. Repopulation by ionization to the metastable or electron impact excitation of Ar^+ are the dominant mechanisms (see Appendix C).

$$\begin{aligned} n_l^P(t > P) &= n_l^P(P) + \left(n_{Ar^+} n_e \langle \sigma_e v_e \rangle + n_{Ar} n_e \langle \sigma_m v_e \rangle\right) t \\ &\approx n_l(P) + R\,t, \end{aligned}$$

where $R \approx 4g_l \times 10^{13} cm^{-3}\ s^{-1}$ for Encore parameters. An expression for the lifetime of dark tagging Θ_D will be derived below using this equation. Electron

collisional excitation from other metastables into state l^P is also approximately linear and of the same order, but much more difficult to calculate.

Bright tagging is destroyed by depopulation of the *filled* metastable state $f^P = l^S$ due to electron collisional excitation. The cross section for electron excitation of the dipole allowed transition m $\rightarrow$ n averaged over a Maxwellian velocity distribution in the Bethe approximation is

$$\langle \sigma_{mn} v_e \rangle = 3.7 \times 10^{-13} \frac{A_{nm} g_{mn} \langle g(n,m) \rangle}{\Delta E_{nm}^3 T_e^{1/2}} \exp\left(-\frac{\Delta E_{nm}}{T_e}\right) cm^3 s^{-1}$$

where $\langle g(n,m) \rangle$ is the thermal averaged Gaunt factor (≈ 0.2 for ions), ΔE_{nm} is the energy difference between states in eV and T_e is the electron temperature in eV (Book '90). The depopulation rate is approximately

$$D_B = \sum_n n_e \langle \sigma_{ln} v_e \rangle (1 - A_{nl} \tau_n) \, s^{-1} \tag{B.3}$$

where the subscript B emphasizes that for bright tagging the final pump state and lower search state are identical to $l = f^P = l^S$. The sum is over all states n radiatively connected to the metastable state l, n_e is the electron density, and $1 - A_{nm}\tau_n$ is the fraction of excited ions that do not return to the metastable. Using D_B in a simple rate equation for the surplus population in state l,

$$n_l^S(t > P) \approx n_f^P(0) + n_{LIF}^P(P) \exp(-D_B t).$$

Bright tagging lifetimes $\Theta_B \equiv D_B^{-1}$ for states in ArII are given in Table B.2.

The difference between the two detagging mechanisms is that the depopulation rate of a filled state depends on the excess population, leading to exponential behavior in time. The repopulation of an emptied state, on the other hand, is determined primarily by the ambient plasma conditions which are changed very little by the tagging so the persistence has linear time behavior. Table B.2 shows

that in Encore tagging of both types will be limited to a marginal $\sim 20\mu s$ due to electron collisional processes except for bright tagging using $3d\,^2F_{7/2}$.

State	$\Theta_B[\mu s]$	$\Theta_D\,[\mu s]$	State	$\Theta_B[\mu s]$	$\Theta_D\,[\mu s]$
$3d\,^4D_{7/2}$	31	25	$3d\,^4F_{7/2}$	15	23
$3d\,^4D_{5/2}$	23	24	$3d\,^2F_{7/2}$	285	21
$3d\,^4D_{3/2}$	20	23	$3d'\,^2G_{9/2}$	20	18
$3d\,^4D_{1/2}$	52	24	$3d'\,^2G_{7/2}$	19	21
$3d\,^4F_{9/2}$	16	21			

Table B.2: Bright tagging times for long-lived ArII states calculated from Eq. B.3. Dark tagging times using $R = 4g_l \times 10^{13}cm^{-3}\ s^{-1}$, $n_l^S(0) = g_l \times 10^9 cm^{-3}$ and $\theta_{las} = 20ns$.

Assuming all LIF signals can be detected with equal efficiency, the *best* tagging scheme is the one which gives the largest modulation between tagged and untagged signal, i.e., the best ratio of tagged over untagged search LIF signal

$$\Xi = \left| \frac{n_{LIF}^S(S)}{n_{LIF}^S(U)} - 1 \right|.$$

For dark signal tagging this figure of merit may be expressed using the assumption $l^P = l^S = l^U$ implying $n_l^P(0) = n_l^U(0)$.

$$\Xi_D = \xi^P - \frac{\Theta}{\Theta_D},$$

where the superscript P is a reminder that ξ depends on atomic parameters of the pumped states. The dark tagging lifetime is found to be $\Theta_D = \xi^P n_l^S(0)/R$. Values of Θ_D for the best dark tagging scheme from each long-lived state are displayed in Table B.2. Dark signal tagging is limited to a figure of merit $\Xi_D \leq 1$ since the modulation is limited by reducing an LIF signal to zero, even if the tagging time were infinite. Table B.3 displays the best dark signal tagging schemes for

each lower state. While Ξ_D is determined by the pump efficiency ξ^P the absolute magnitude of the LIF signal is proportional to the efficiency ξ^S of the search transition. The search u and f states may be different from the pump scheme to increase the detectable signal.

Bright signal tagging is also proportional to the ξ^P

$$\Xi_B = A^P_{uf} \tau^P_{oth} \xi^P g^P_{lf} \exp\left(-\frac{\Theta}{\Theta_B}\right),$$

but the limit on Ξ_B depends on atomic parameters of the pump scheme states. Non-metastable states are typically radiatively connected to many lower states implying $A_{uf}\tau_{oth} \ll 1$. The ratio of statistical weights appears from the assumption $n^P_l(0)/n^P_f(0) = g^P_{lf}$. For ArII metastables $8/10 \leq g^P_{lf} \leq 10/8$. Allowing the use of the long-lived states gains little since $g^P_{lf} \leq 1 + 4/g^P_f \leq 3$ ($g = 2j + 1$ and $\Delta j = -1, 0, 1$). Thus Ξ_B is expected to be much less than Ξ_D when considering tagging from a given lower state unless $n^P_l(0)/n^P_f(0) \gg g^P_{lf}$ or $\Theta_B \gg \Theta_D$. Atomic parameters for allowed transitions do not vary that much so it is not surprising that $\Xi_B < \Xi_D$ irrespective of the lower state. The best bright tagging pump schemes are presented in Table B.3.

Compared to the other states the $3d\,^2F_{7/2}$ state has a much longer bright tagging time $\Theta_B \approx 250\mu s$ because the energy differences between the transitions most likely to be excited by electron collisions are greater than any of the other states. Perhaps this state could be used to follow ions over long distances in Encore. Unfortunately, it has $\Xi_B \leq 0.008$. Ignoring shot to shot fluctuations and spatial diffusion, the *best* modulation to be expected is only 0.008 which does little to encourage changing the current dye laser pump source to produce $\lambda^S_{las} = 4682$Å light.

	Dark Tagging ($l^P = l^S$)			Bright Tagging ($f^P = l^S$)			
l^S	λ^P_{las} [Å]	u^P	Ξ_D	l^P	λ^P_{las} [Å]	u^P	Ξ_B
$3d\,^4D_{7/2}$	4014	$4p\,^4D^o_{7/2}$	0.99	$3d\,^4D_{5/2}$	4432	$4p\,^4P^o_{5/2}$	0.195
$3d\,^4D_{5/2}$	4039	$4p\,^4D^o_{7/2}$	0.94	$3d\,^4D_{3/2}$	4400	$4p\,^4P^o_{3/2}$	0.13
$3d\,^4D_{3/2}$	3992	$4p\,^4D^o_{5/2}$	0.92	$3d\,^4D_{5/2}$	4352	$4p\,^4P^o_{3/2}$	0.19
$3d\,^4D_{1/2}$	3531	$4p\,^4S^o_{3/2}$	0.94	$3d\,^4D_{3/2}$	4432	$4p\,^4P^o_{1/2}$	0.316
$3d\,^4F_{9/2}$	6644	$4p\,^4D^o_{7/2}$	0.86	**$3d\,^4D_{7/2}$**	4014	$4p\,^4D_{7/2}$	0.087
$3d\,^4F_{7/2}$	6687	$4p\,^4D^o_{7/2}$	0.92	**$3d\,^4D_{7/2}$**	4431	$4p\,^4D^o_{5/2}$	0.088
$3d\,^2F_{7/2}$	4682	$4p'\,^2F^o_{7/2}$	0.84	**$3d'\,^2G_{9/2}$**	6115	$4p'\,^2F^o_{7/2}$	0.008
$3d'\,^2G_{9/2}$	6115	$4p'\,^2F^o_{7/2}$	0.73	**$3d'\,^2G_{7/2}$**	6123	$4p'\,^2F^o_{7/2}$	0.12
$3d'\,^2G_{7/2}$	6123	$4p'\,^2F^o_{7/2}$	0.84	**$3d\,^2F_{7/2}$**	4711	$4p'\,^2F^o_{5/2}$	0.13

Table B.3: The best tagging pump schemes for each lower state in ArII. Metastables are in boldface. ($\theta_P = 20$ns, $\Theta = 0$)

Earlier experiments on Encore were marginally successful in detecting tagged signal differences using the pump and search schemes based on $3d'\,^2G_{9/2}$ with $\Xi_D = 0.73$ and $\Xi_L = 5.7$ (McChesney '91). Since detection of the LIF was not a problem, the $3d\,^4F_{7/2} \rightarrow 4p\,^4D^o_{7/2} \rightarrow 4s\,^4P_{5/2}$ dark tagging pump and search schemes could increase the difference signal by $\sim 20\%$ and the tagging lifetime by $\sim 24\%$ with only a small reduction in absolute LIF.

B.2 Atomic Data Relevant to LIF in ArII

The following tables contain information necessary to assess the relative merits of proposed LIF schemes in ArII. There are seven metastable states and three very long-lived states in the 3d level which may be used for LIF. ArII has three systems of states with inner core excited states ^3P, ^1D and ^1S which are denoted by unprimed, singly primed and doubly primed notation respectively. Table B.4 lists the relevant states, their radiative lifetimes and their energies with respect to the ArII ground state $3p^4(^3P)$. The states are labeled using combinations of spin and orbital angular momenta.

Table B.5 lists many of the transitions between the states in Table B.4 with wavelengths and transition probabilities. All transitions from the metastables are shown if the transition rate is known. The double-headed arrows $\leftrightarrow$ are reminders that metastables and long-lived states may be suitable for lower states in LIF schemes. Only lower states with large transition probabilities or long lifetimes are explicitly displayed.

State	E (cm^{-1})	τ_n (ns)	State	E (cm^{-1})	τ_n (ns)
$3d\,^4D_{7/2}$	132 327	metastable	$4p\,^4P^o_{5/2}$	155 043	*8.0*
$3d\,^4D_{5/2}$	132 481	5870	$4p\,^4P^o_{3/2}$	155 351	*8.1*
$3d\,^4D_{3/2}$	132 631	13100	$4p\,^4P^o_{1/2}$	155 708	*8.1*
$3d\,^4D_{1/2}$	132 738	68500	$4p\,^4D^o_{7/2}$	157 234	5.57
$4s\,^4P_{5/2}$	134 242	67.1	$4p\,^4D^o_{5/2}$	157 673	7.5
$4s\,^4P_{3/2}$	135 086	28.7	$4p\,^4D^o_{3/2}$	158 168	7.4
$4s\,^4P_{1/2}$	135 602	119	$4p\,^4D^o_{1/2}$	158 428	*8.0*
$4s\,^2P_{3/2}$	138 244	0.45	$4p\,^2D^o_{5/2}$	158 730	*9.0*
$3d\,^4F_{9/2}$	142 186	metastable	$4p\,^2P^o_{1/2}$	159 707	*8.0*
$3d\,^4F_{7/2}$	142 717	metastable	$4p\,^4S^o_{3/2}$	161 049	*7.5*
$4s'\,^2D_{3/2}$	148 620	53.0	$3d'\,^2F_{7/2}$	163 506	**metastable**
$4s'\,^2D_{5/2}$	148 842	27.6	$4p'\,^2F^o_{5/2}$	170 401	*8.9*
$3d\,^2F_{7/2}$	149 179	metastable	$4p'\,^2F^o_{7/2}$	170 530	*8.5*
$3d'\,^2G_{9/2}$	154 182	metastable	$4p'\,^2D^o_{5/2}$	173 393	*8.0*
$3d'\,^2G_{7/2}$	154 204	metastable			

Table B.4: ArII states important for LIF schemes. Energies are from Bashkin ('75). Lifetimes are from Luyken ('72) except those in italic digits from García ('85) and in boldface from Varga ('81).

transition states lower		upper	λ (Å)	A ($10^6 s^{-1}$)
$3d\,^4D_{7/2}$	↔	$4p\,^4P^o_{5/2}$	4401	35.7
$3d\,^4D_{5/2}$	↔		4431	12.2
$3d\,^4D_{3/2}$	↔		4461	1.73
$4s\,^4P_{5/2}$	←		4806	87.2
$4s\,^4P_{3/2}$	←		5009	16.3
$3d\,^4D_{5/2}$	↔	$4p\,^4P^o_{3/2}$	4371	25.8
$3d\,^4D_{3/2}$	↔		4400	18.2
$4s\,^4P_{5/2}$	←		4736	65
3 more lines			4421–5062	
$3d\,^4D_{3/2}$	↔	$4p\,^4P^o_{1/2}$	4332	23
$3d\,^4D_{1/2}$	↔		4352	25.3
$4s\,^4P_{3/2}$	←		4848	94
$4s\,^4P_{1/2}$	←		4972	10.7
$3d\,^4D_{7/2}$	↔	$4p\,^4D^o_{7/2}$	4014	11.9
$3d\,^4D_{5/2}$	↔		4039	1.41
$4s\,^4P_{5/2}$	←		4348	137
$3d\,^4F_{9/2}$	↔		6644	18.3
$3d\,^4F_{7/2}$	↔		6887	1.7
$3d\,^4D_{7/2}$	↔	$4p\,^4D^o_{5/2}$	3944	4.47
$3d\,^4D_{5/2}$	↔		3968	5.2
$3d\,^4D_{3/2}$	↔		3992	1.69
$4s\,^4P_{3/2}$	←		4426	92
$3d\,^4F_{7/2}$	↔		6684	14.06
3 more lines			4267–6864	
$3d\,^4D_{5/2}$	↔	$4p\,^4D^o_{3/2}$	3892	8.1
$3d\,^4D_{3/2}$	↔		3915	3.6
$3d\,^4D_{1/2}$	↔		3931	2.2
$4s\,^4P_{3/2}$	←		4331	63
5 more lines			4178–6757	
$3d\,^4D_{3/2}$	↔	$4p\,^4D^o_{1/2}$	*3875*	*5.4*
$3d\,^4D_{1/2}$	↔		*3891*	*3.4*
$4s\,^4P_{1/2}$	←	$4p\,^4D^o_{1/2}$	*4380*	*87.9*
5 more lines			*4283–9151*	
$3d\,^4D_{7/2}$	↔	$4p\,^2D^o_{5/2}$	3786	1.3
$4s\,^2P_{3/2}$	←		4880	87.0
$3d\,^4F_{7/2}$	↔		6243	2.99
2 more lines			4082, 4228	
$3d\,^4D_{1/2}$	↔	$4p\,^2P^o_{1/2}$	*3707*	*0.6*
$4s\,^2P^o_{3/2}$	←		*4658*	*80.2*
6 more lines			*4147–9018*	
$3d\,^4D_{5/2}$	↔	$4p\,^4S^o_{3/2}$	*3499*	*0.5*
$3d\,^4D_{3/2}$	↔		*3518*	*0.2*
$3d\,^4D_{1/2}$	↔		*3531*	*<0.2*
$4s\,^4P_{5/2}$	←		*3729*	*47.1*
10 more lines			*3851–8190*	
$3d\,^4D_{7/2}$	↔	$4p'\,^2F^o_{5/2}$	*2626*	*<0.06*
$3d\,^4D_{5/2}$	↔		*2636*	*<0.06*
$4s'\,^2D_{3/2}$	←		*4590*	*62.9*
$3d\,^2F_{7/2}$	←		*4711*	*0.4*
$3d'\,^2G_{7/2}$	←		*6172*	*18.9*
7 more lines			*3108–5176*	
$3d\,^4D_{7/2}$	↔	$4p'\,^2F^o_{7/2}$	*2617*	*0.03*
$3d\,^4D_{5/2}$	↔		*2627*	*0.02*
$4s'\,^2D_{5/2}$	←		*4610*	*75.9*
$3d\,^2F_{7/2}$	↔		*4682*	*0.8*
$3d'\,^2G_{9/2}$	↔		*6115*	*21.2*
$3d'\,^2G_{7/2}$	↔		*6123*	*0.9*
4 more lines			*2754–5142*	
$3d\,^2F_{7/2}$	↔	$4p'\,^2D^o_{5/2}$	4129	2.52
$4s'\,^2D_{3/2}$	←		4035	2.22
$4s'\,^2D_{5/2}$	←		4072	40.6

Table B.5: ArII transitions important for LIF schemes. Wavelengths from Norlén ('73) and transition probabilities from Luyken ('72) except entries in italic digits from García ('85). Metastable states are in boldface.

Appendix C

METASTABLE POPULATION MODEL

Predicting the population of metastable states in a plasma involves considering the large number of reactions which produce and destroy metastables. In order to assess the relative significance of the various reactions the following typical Encore plasma parameters are assumed initially: $T_e = 15eV$, $T_i = 5eV$, $n_{Ar^+} \approx n_e \approx 10^{12}cm^{-3}$ and $n_{Ar} \approx n_{Ar_m^+} \approx n_{Ar^{++}} \approx 10^{11}cm^{-3}$. The assumed metastable and neutral populations are chosen to enhance the importance of reactions with these reactants. Below is a short list of the possible metastable production reactions.

$$Ar + e^- \rightarrow Ar_m^+ + 2e^- \tag{C.1}$$

$$Ar^+ + e^- \rightarrow Ar_*^+ + e^- \rightarrow Ar_m^+ + h\nu + e^- \tag{C.2}$$

$$Ar + h\nu \rightarrow Ar_m^+ \tag{C.3}$$

$$Ar^{++} + Ar \rightarrow Ar_m^+ + Ar^+ \tag{C.4}$$

$$Ar^{++} + e^- \rightarrow Ar_m^+ + h\nu \tag{C.5}$$

$$Ar^+ + h\nu \rightarrow Ar_*^+ \rightarrow Ar_m^+ + h\nu_* \tag{C.6}$$

$$Ar^+ \rightarrow Ar_m^+ + h\nu$$

$$Ar^+ + Ar \rightarrow Ar + Ar_m^+$$

$$Ar^+ + Ar \rightarrow Ar_m^+ + Ar$$

$$Ar^+ + Ar^+ \rightarrow Ar_m^+ + Ar^+$$

$$Ar^+ + Ar^+ \rightarrow Ar_m^+ + Ar_m^+$$

Based on the following simple estimations, direct electron impact ionization (Eq. C.1) and electron collisional excitation of non-metastable Ar^+ (Eq. C.2) prove to be the dominant metastable production mechanisms in the Encore plasma.

Using a linear composite approximation to the cross section for ionization to a metastable state as a function of incident electron energy σ_{im} (Varga '81) and averaging over a Maxwellian gives $\langle \sigma_{im} v_e \rangle \approx 10^{-10} cm^3 s^{-1}$. The metastable production rate per volume is $X_m = n_{Ar} n_e \langle \sigma_{im} v_e \rangle \approx 10^{13} cm^{-3} s^{-1}$ for Eq. C.1. Because spontaneous decay from electronic states above the metastable states takes place on a $\sim$10ns time scale, these cascade events were included in Varga's ('81) measurement. Compared to the total ionization cross section σ_{it} (Goeckner '91) $\sigma_{im}/\sigma_{it} < 3.5\%$. The production rate per volume due to electron excitation of Ar^+ to a metastable can be estimated using electron collision coefficients (Born-Coulomb approximation) and average radiative transition rates (Kitaeva '70). By definition the metastables do not have allowed transitions to any lower states. It is likely that the dominant electron-ion collision terms which populate the metastables are the 3p $\rightarrow$ 4p and 3p $\rightarrow$ 4d terms which then radiatively decay into one of the 3d metastable states.† Ratios of statistical weights are used to determine the population fractions within the 3d metastables giving a metastable production

† Even though the transition from the ground state to the metastable is forbidden, direct electron impact excitation and de-excitation may play an important role in determining the metastable population. The cross section for excitation via a forbidden transition σ_f is typically sharply peaked at low electron energy where the population of electrons is high while the cross section for excitation via an allowed transition σ_a is broad and peaks at much higher energies in the tail of the electron distribution. Although the peak in σ_f is usually over an order of magnitude smaller than σ_a, it may be that $\langle \sigma_f v_e \rangle \gg \langle \sigma_a v_e \rangle$ and the forbidden path plays a dominant role in determining the metastable population. Davis ('75) briefly discusses this case for Ar ion lasers, but the cross section data for Ar ions is not available to make quantitative calculations.

rate per volume of $X_e \approx 10^{13}cm^{-3}s^{-1}$ for Eq. C.2. Using the total cross section for charge exchange of Ar^{++} in Ar, $\sigma_{dx} \ll 10^{-18}cm^2$ (Arnot '39), the production rate per volume of Eq. C.4 can be overestimated at $X_{dx} \ll 10^{10}cm^{-3}s^{-1}$. Recombination (Eq. C.5 Turner '83) $X_{recomb} \approx 10^{11}cm^{-3}s^{-1}$ and photoionization (Eq. C.3 Silfvast '86) are negligible in the Encore discharge. Inelastic collisions and charge exchange events probably have similar cross sections so the other reactions have production rates per volume $\sim 10^{12}cm^{-3}s^{-1}$ (Cramer '59). It is beyond the scope of this work to include an accounting of the transition photons as Eq. C.6 demands. It is unclear how important a role they play in an optically thin, cold (compared to the energies of photons making transitions to the ground state) plasma inside a poorly reflecting vacuum vessel.

During a discharge the production of metastables is offset by metastable quenching reactions. An incomplete list of reactions is presented below.

$$Ar_m^+ + e^- \rightarrow Ar^+ + e^- \tag{C.7}$$

$$Ar_m^+ + Ar \rightarrow Ar_m + Ar^+ \tag{C.8}$$

$$Ar_m^+ + h\nu \rightarrow Ar^+ + h\nu_*$$

$$Ar_m^+ + Ar \rightarrow Ar^+ + Ar^*$$

$$Ar_m^+ + Ar \rightarrow Ar + Ar^+$$

$$Ar_m^+ + Ar \rightarrow 2Ar^+ + e^-$$

$$Ar_m^+ + Ar^+ \rightarrow Ar^+ + Ar^+$$

$$Ar_m^+ + Ar^+ \rightarrow Ar^{++} + Ar$$

The cross section for charge exchange with metastable ions $\langle \sigma_{xm} v_e \rangle \approx 3 \times 10^{-10}cm^3s^{-1}$ (Kadota '74), gives a quenching rate of $X_{xm} \approx 10^{12}cm^{-3}s^{-1}$ for Eq. C.8. As noted above, the other inelastic and charge exchange reactions may have similar rates

per volume. The de-excitation from a single metastable state due to electron collisions (Eq. C.7) is $X_{e\nu} \approx 10^{15}\text{cm}^{-3}\text{s}^{-1}$ (Kitaeva '70). Complete information on all the remaining cross sections are not known and the transition photons are again ignored. The results of these estimates are compiled in Table C.1.

Reaction Producing or Quenching ArII Metastables	X $[cm^{-3}s^{-1}]$ estimate	model
direct electron impact ionization	10^{13}	2×10^{14}
electron collisional excitation from a non-metastable Ar^+	10^{13}	4×10^{13}
charge exchange with Ar^{++}	$\ll 10^{10}$	0
recombination of Ar^{++}	10^{11}	0
photoionization	-	0
inelastic collisions	$\sim 10^{12}$	0
electron collisional de-excitation	(10^{15})	(2×10^{14})
neutral charge exchange	(10^{12})	(3×10^{12})
wall recombination	(10^{15})	(3×10^{13})

Table C.1: Summary of metastable production (quenching) reactions. The estimated rates used to determine the dominant reactions may be compared with the results of the model with $T_e = 15eV$, $T_i = 5eV$, $n_e = 2.5 \times 10^{12}$, $n_{tot} = 3 \times 10^{12} cm^{-3}$ and wall recombination time $\tau = 100 \mu s$.

A model for the metastable population can now be constructed retaining only the dominant reactions† and their cross sections,

$$Ar + e^- \rightarrow Ar_m^+ + 2e^-, \qquad \sigma_{im} \tag{C.1}$$

$$Ar^+ + e^- \rightarrow Ar_m^+ + h\nu + e^-, \quad \sigma_{em} \tag{C.2}$$

$$Ar_m^+ + e^- \rightarrow Ar^+ + e^- + h\nu, \quad \sigma_{e\nu}, \tag{C.7}$$

† Given the ignorance of most charge exchange cross sections and the assumption that inverse processes have comparable cross sections, these reactions are ignored. It can be shown a posteriori that metastable quenching rate due to charge exchange with neutrals is at least an order of magnitude smaller than the other rates (see Table C.1) and has negligible effect on the results of the model. It is more difficult to rationalize ignoring the transition photons.

adding ionization to a non-metastable with σ_i, recombination at the wall with time constant τ,

$$Ar + e^- \rightarrow Ar^+ + 2e^-, \quad \sigma_i \tag{C.9}$$

$$Ar^+, Ar_m^+ \overset{wall}{\rightarrow} Ar, \tag{C.10}$$

and requiring the total Ar density to be constant $n_{tot} = n_{Ar} + n_{Ar+} + n_{Ar_m^+}$. The following simple set of equilibrium equations can be solved for the metastable population.

$$\dot{n}_{Ar} = 0 = -\langle\sigma_I v_e\rangle n_e n_{Ar} + (n_{Ar+} + n_{Ar_m^+})\tau^{-1}$$

$$\dot{n}_{Ar+} = 0 = \langle\sigma_i v_e\rangle n_e n_{Ar} + \langle\sigma_{e\nu} v_e\rangle n_e n_{Ar_m^+} - \langle\sigma_{em} v_e\rangle n_e n_{Ar+} - n_{Ar+}\tau^{-1}$$

$$\dot{n}_{Ar_m^+} = 0 = \langle\sigma_{im} v_e\rangle n_e n_{Ar} - \langle\sigma_{e\nu} v_e\rangle n_e n_{Ar_m^+} + \langle\sigma_{em} v_e\rangle n_e n_{Ar+} - n_{Ar_m^+}\tau^{-1}$$

where $\sigma_I = \sigma_{im} + \sigma_i$ is the total ionization cross section. The solution to the system may be written using the rates normalized to the confinement time as follows: ionization to metastables $M = \langle\sigma_{im} v_e\rangle n_e \tau$, electron-ion collisions to metastables $E = \langle\sigma_{em} v_e\rangle n_e \tau$, ionization to non-metastables $I = \langle\sigma_i v_e\rangle n_e \tau$, electron de-excitation of metastables $N = \langle\sigma_{e\nu} v_e\rangle n_e \tau$ and total ionization $J \equiv I + M$.

$$n_{Ar} = \frac{n_{tot}}{1 + J}$$

$$n_{Ar_m^+} = \frac{(M + EJ) n_{tot}}{(1 + J)(E + N + 1)}$$

$$n_{Ar+} = \frac{(I + NJ) n_{tot}}{(1 + J)(E + N + 1)}$$

Given the electron density and temperature the $\langle\sigma v_e\rangle$ integrals (or approximations) over a Maxwellian velocity distribution are performed and the equations above calculated. The results from such calculations for parameters relevant to Encore are discussed in Chapter 4.

Appendix D

SEMI-CLASSICAL LIF MODEL

A semi-classical model is used to describe the interaction of light with a resonant electronic transition. Spatial uniformity of the laser and plasma is assumed and only the three states of the PLIF scheme used for this experiment are considered. See Figure D.1 for the states and the notation used in the model.

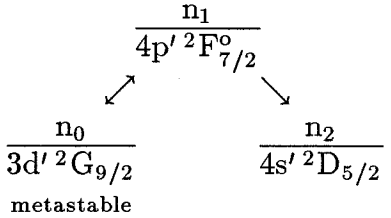

Figure D.1 : ArII LIF scheme with notation for the semi-classical model.

The state populations as a function of the ion speed parallel to the laser propagation vector and time $n_i(v,t)$ obey the following equations.

$$\begin{aligned} \dot{n}_0 &= -(\frac{1}{\tau_0} + B_{01}\Phi)n_0 + (A_{10} + B_{10}\Phi)n_1 \\ \dot{n}_1 &= B_{01}\Phi n_0 - (\tau_1^{-1} + B_{10}\Phi)n_1 \end{aligned} \tag{D.1}$$

A_{10}, B_{01} and B_{10} are the Einstein coefficients in terms of intensity for the transition with resonant frequency f_0; τ_0 and τ_1 are the radiative lifetimes of the states;

$$\Phi(v,t) \equiv \int_{-\infty}^{+\infty} I(f,t)\, g(v,f)\, df$$

is the effective intensity of the radiation for a class of particles with speed v parallel to the laser propagation taking into account the Doppler shifted homogeneous absorption lineshape

$$g(v,f) = \frac{A_{10}}{4\pi^2 \left[\left(f - f_0\left(1 + \frac{v}{c}\right)\right)^2 + \left(\frac{A_{10}}{4\pi}\right)^2\right]}$$

and a Gaussian frequency lineshape for a laser with intensity

$$I(f,t) = \begin{cases} I_0 \left(\frac{4\ln 2}{\pi}\right)^{\frac{1}{2}} \frac{\theta}{\Delta f_L} \exp\left[-4\ln 2 \left(\frac{f-f_L}{\Delta f_L}\right)^2\right] & 0 < t < \tau_L \\ 0 & t < 0,\ \tau_L < t \end{cases}$$

where the laser with linewidth Δf_L is centered on f_L with a step function dependence on time ($\theta = 1s^{-1}$ for proper units). Eq. D.1 can be written in matrix form as $\dot{\mathbf{x}} = \mathbf{A}\mathbf{x}$ which has the matrix solution $\mathbf{x} = \mathbf{x_0}\exp(\mathbf{A}t)$ where

$$\mathbf{A} = \begin{pmatrix} -\frac{1}{\tau_0} - B_{01}\Phi & A_{10} + B_{10}\Phi \\ B_{01}\Phi & -\frac{1}{\tau_1} - B_{10}\Phi \end{pmatrix}, \qquad \mathbf{x_0} = \begin{pmatrix} n_0 \\ n_1 \end{pmatrix}_{t=0}. \tag{D.2}$$

The eigenvalues of $\mathbf{A}$ are $\lambda_\pm = -\frac{\Gamma}{2}(1 \pm \gamma)$ where $\Gamma = \tau_0^{-1} + \tau_1^{-1} + b_{01} + b_{10}$, $\gamma = \left[1 - 4\Gamma^{-2}\left(\tau_0^{-1}\left(\tau_1^{-1} + b_{10}\right) + b_{01}\left(\tau_1^{-1} - A_{10}\right)\right)\right]^{\frac{1}{2}}$, $b_{01} = B_{01}\Phi(v,t)$ and $b_{10} = B_{10}\Phi(v,t)$. Defining $\alpha = \tau_1^{-1} + b_{10}$, $P = \lambda_+ + \alpha$, $M = \lambda_- + \alpha$, and $t_\pm = \exp(t\lambda_\pm)$,

$$e^{\mathbf{A}t} = \frac{1}{\Gamma\gamma}\begin{pmatrix} Pt_+ + Mt_- & (A_{10} + b_{10})(t_- - t_+) \\ b_{01}(t_- - t_+) & Mt_+ + Pt_- \end{pmatrix}.$$

Thus the state populations can be calculated. The LIF signal is proportional to the number of spontaneous fluorescence photons emitted per volume from the transition $1 \rightarrow 2$. Assuming the initial population of the upper state $n_1(v, t = 0)$ is negligible the number of LIF photons emitted per volume is

$$\begin{aligned} N_{h\nu} &= \int_{-\infty}^{+\infty} dv \int_0^{\tau_{obs}} A_{12} n_1(v,t)\, dt \\ &= \int_{-\infty}^{+\infty} dv A_{12} \left[n_0(v, t=0)\frac{b_{01}}{\Gamma\gamma}\int_0^{\tau_L} \left(e^{t\lambda_-} - e^{t\lambda_+}\right) dt \right. \\ &\qquad \left. + n_1(v, t=\tau_L)\int_{\tau_L}^{\tau_{obs}} e^{-\frac{t-\tau_L}{\tau_1}} dt \right] \\ &= \int_{-\infty}^{+\infty} dv\, A_{12} n_0(v, t=0)\frac{b_{01}}{\Gamma\gamma} \\ &\qquad \times \left\{ \frac{4\gamma}{\Gamma(1-\gamma^2)} + e^{\tau_L\lambda_-}\left[\lambda_-^{-1} + \tau_1(1-\delta)\right] - e^{\tau_L\lambda_+}\left[\lambda_+^{-1} + \tau_1(1-\delta)\right] \right\} \end{aligned}$$

where the terms involving $\delta = \exp[-(\tau_{obs} - \tau_L)/\tau_1]$ are usually small correction terms.† This expression can be calculated for given experimental conditions. Results from such calculations are discussed in Chapter 4.

† This expression is a generalization and slight correction of Equation 6 of Goeckner ('89).

Appendix E

OPTICAL SYSTEM DESIGN

E.1 Interactive Optical System Design

Conflicting nonlinear constraints and many design options prevented derivation of analytic formulae for *the optimal* PLIF system optical design. Due to the complexity of the system the computer program LENSYS was written to quickly calculate and display critical characteristics of proposed designs to allow personal evaluation of the various trade-offs in performance. LENSYS uses the paraxial approximation in the Gaussian lens formula and matrix ray tracing. The physical dimensions of the MCP PMT photocathode and housing, the Encore tokamak and the interference filter are considered fixed design constraints (see Figure 5.2). The angle between the laser sheet and a major radius is a user specified parameter. LENSYS also allows for the choice of the number of lenses with their focal lengths, widths, diameters and positions along a user specified optical axis (parallel to a major radius). Lenses oblique to the optical axis and off axis were also included for a time, but were finally rejected due to the complexity of the designs and insufficient promise for improved system performance. The interference filter can also be inserted anywhere in the system for transmission analysis.

The primary objective in designing the PLIF optical system was to image as much of a poloidal cross section of the Encore tokamak as possible. The plasma illuminated by the laser sheet at a small angle to the poloidal cross section is the object of the system. The MCP PMT photocathode is the field stop, the element limiting the size of the object which is imaged.† LENSYS calculates the image

† The phrases defining field stop, aperture stop, entrance pupil and marginal rays are adapted from Hecht and Zajac ('74).

plane of the laser sheet, places the photocathode field stop in that plane and finds the points in the fluorescing plasma sheet corresponding to each anode corner. Key dimensions and drawings of the resulting design are displayed on the screen for evaluation (see Figure E.2).

For a single lens with diameter D and focal length f, the image brightness is proportional to the solid angle Ω subtended by the lens which is proportional to $(D/f)^2$, the square of the relative aperture. Figure E.1 illustrates this point in a simple system with an object m focal lengths away from a small diameter lens. The angle θ between the optical axis and a marginal ray just hitting the edge of the lens determines the solid angle. The inverse of the relative aperture is the f-number of the lens (f/#). Since the PLIF is weak, a low f/# lens is desired to collect as much fluorescence as possible. Unfortunately, the necessary interference filter will only pass light at the desired wavelength for rays at nearly normal incidence. Much of the light collected by a low f/# lens would have large angles of incidence on a filter in front of the detector (see Figure E.1). This situation can be improved by sandwiching the filter between a negative-positive lens pair. A negative lens placed approximately one of its focal distances in front of the image formed by a primary lens will cause the resulting image to be at infinity. Then the rays will be nearly parallel to the optical axis, almost normally incident on a filter immediatly following the negative lens. The positive lens refocuses the filtered light to form an image on the detector.

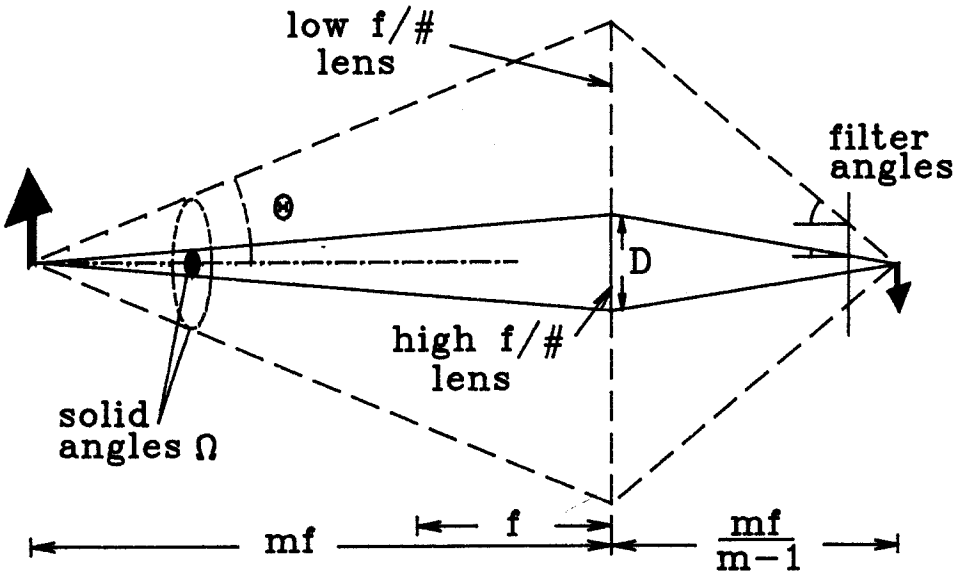

$$\Omega = 2\pi(1-\cos\theta) \approx 2\pi\frac{\theta^2}{2}$$
$$\approx \frac{\pi}{4m^2}\left(\frac{D}{f}\right)^2$$
$$\approx \frac{\pi}{4m^2}(f/\#)^{-2}$$

Figure E.1 : Simple imaging lens illustrating the concepts of relative aperture, f/# and their effect on angles of incidence on a filter.

For interactive design, nontrivial measures of the system collection efficiency and filter transmission must be calculated quickly. The solid angle subtended by the optics, which determines the maximum possible collection efficiency, is related to the clear aperture of the system. The physical element(s) that limit the amount of light reaching the image plane is(form) the aperture stop. The aperture stop varies across the imaged plasma in the PLIF experiment due to range of object distances. The aperture stop for a given point in the plasma may be the tokamak chamber, one of the lenses, the filter edge or a combination of elements. The 'cone' of light actually making it to the image is determined by the *entrance pupil.* Rays from the object pointing towards the edge of the entrance pupil just make it past the aperture stop; these are marginal rays (see Figure E.2). The entrance pupil turns out to be the image of the aperture stop as seen from the object through those elements preceding the stop. Using the pupils due to each lens, the filter and the tokamak chamber, an estimate of the cone angle can be calculated from four marginal rays at the four extreme corners of the imaged plasma. Marginal rays will have the largest angles of incidence on the filter. By tracing these rays through the system an average 'worst' angle of incidence is calculated. In general the angles of incidence tend toward normal for higher f/# systems, in direct competition with the goal of increased collection efficiency.

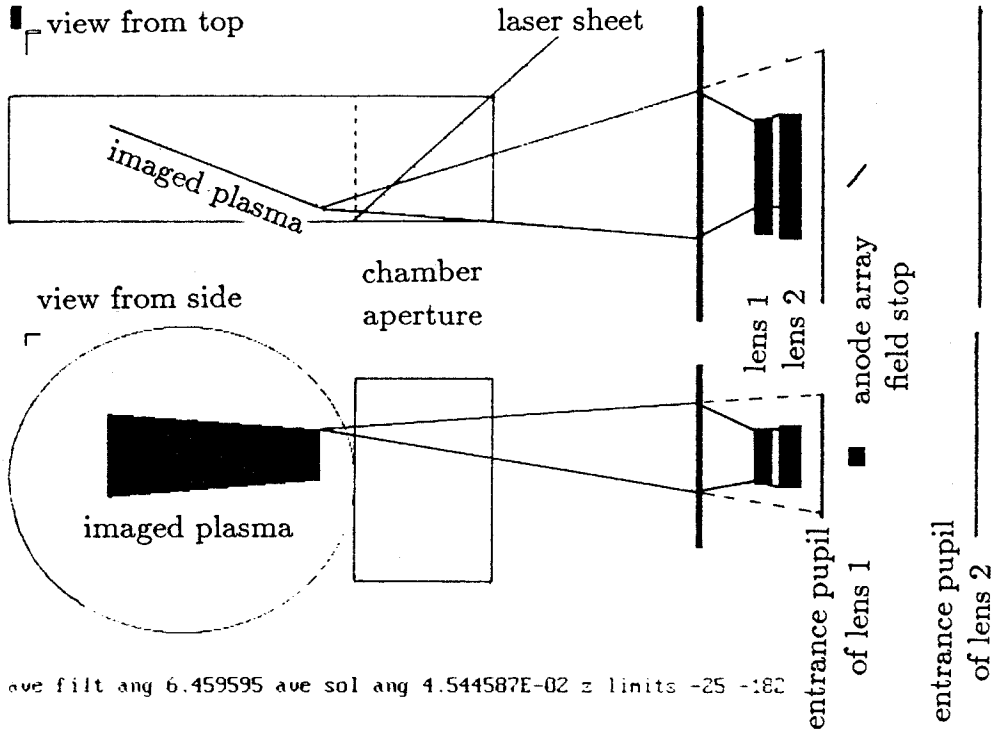

Figure E.2 : Typical LENSYS output screen showing the lens system, entrance pupils aperture stop and field stop. The fixed photocathode field stop determines the area imaged in the plasma. Four marginal rays from a single point in the plasma are displayed. The aperture stop for three of the marginal rays is the edge of lens 1. The tokamak chamber is the aperture stop for the lower ray in the upper figure.

The potential for a suitable design was explored by trying different optical systems with the LENSYS program. The imaged plasma could be compared to the poloidal cross section while noting the behavior of the two figures of merit for the

expected image brightness: the angle subtended by the entrance pupil (collection efficiency) and the angle of incidence on the filter (filter transmission). The design finally adopted attempts to image a large area of the poloidal cross section with a simple design using easily available components while maximizing the collection efficiency and minimizing the filter rejection of the PLIF.

E.2 Results from LENSYS

More detailed calculations of the PLIF collection efficiency were also performed by LENSYS. The details of the calculations are described in Section E.3. With careful choice and placement of optical elements, a large area extending $\sim 2/3$ of the way across the plasma in the poloidal cross section can be imaged (see Figure E.2). The image vignetting can be controlled so that the ratio of anode 'gains' α_o between the center and the edge is as small as 3 (see Figure E.3). However, moving the negative-positive lens and filter cluster a distance as small as 4mm causes the calculated 'gains' of the corner anodes to change dramatically.

A uniform image brightness is not absolutely necessary to make quantitative images of the PLIF magnitude, but it reduces the importance of the scaling factors due to the optical system. With the current system, the spatial structure of the PLIF signal magnitude is dominated by the optical system gains which cannot be calculated with enough confidence to rescale raw data to reflect real image brightness. This problem essentially prevents the present system from being used to make single shot density images. If the gains were known very accurately for a *particular* experimental configuration, they could be used to recover the real PLIF image amplitudes. To date none of the calibrating schemes attempted have proved satisfactory. Despite this problem, the PLIF diagnostic system can still be used to

make detailed plasma measurements that depend on the relative signal intensities on each anode *individually*, i.e, ion distribution measurements.

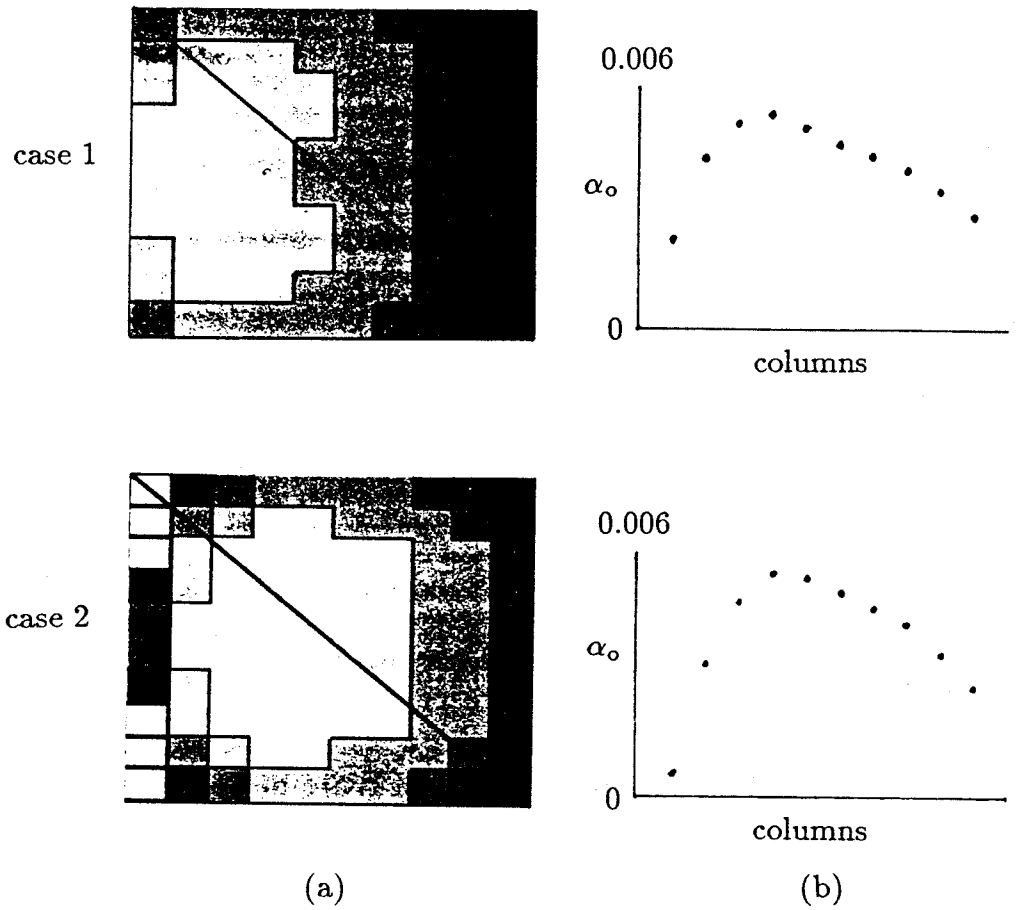

Figure E.3 : Lens system collection efficiency for two cases. The difference between case 1 and 2 is a 4mm displacement of the negative lens/filter/positive lens cluster. (a) Images of $1/\alpha_o$, the multiplication factor which would be used to normalize raw data. The diagrams were plotted in 6 grays with a range of 175 (light) to 450 (dark) cm^{-3}. Note in case 2 the six corner white anodes have gone off scale ($\sim$ 1700). (b) α_o in cm^3 for the anodes in the diagonals indicated.

E.3 Detailed Characterization of Optical Systems

The results discussed in Appendix E.2 were calculated in anticipation of making quantitative scaling of the detected PLIF intensities. The fluorescence from an optically thin plasma is determined by the ion population of the upper state n_1 of the LIF line, assuming the population of n_1 is only generated by the laser,

$$n_1(\mathbf{x}, v, t) = n_0(\mathbf{x}, v) j(t) \qquad \left[\frac{m^{-3}}{v}\right]$$

where $n_0(\mathbf{x}, v)$ is the particle distribution of the pumped state as a function of space and the ion speed and $j(t)$ contains the time dependence and proportionality due to the laser inducing the fluorescence. All these quantities depend on plasma conditions and laser parameters. The fluorescence power from a volume in the plasma is

$$p(\mathbf{x}, t) = \int h\nu(v)\, A_{12} n_1(\mathbf{x}, v, t)\, dv \qquad [W\, m^{-3}]$$

with Planck's constant h, the wavelength of the emitted fluorescence $\nu(v)$ as a function of the speed of the ions and the transition probability A_{12}. The power incident on the photocathode is the volume integral of $p(\mathbf{x}, t)$ collected by the optical system. This complicated integral is simplified by considering only the fluorescing volume in the laser sheet and assuming uniform density on scale of lengths the order of the laser sheet width $\Delta_\perp \approx 1$mm. The collection efficiency of the optics is also a complicated function involving the geometry of the optics and filter as described in Section E.1. The optics system transmission for a given differential solid angle element is a function of the exact path the ray bundle traverses (see Figure E.4).

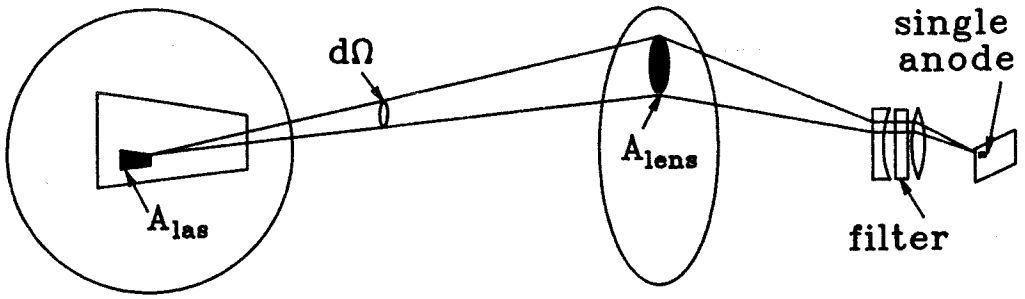

Figure E.4 : Schematic of a ray bundle path.

The power incident on the photocathode corresponding to a particular anode is

$$P_a(t) = \int \left\{ p(\mathbf{x}, t)\Delta_\perp \int T(\Omega, A_{lens}) \frac{d\Omega}{4\pi} \right\} dA_{las} \qquad [W]$$

where $T(\Omega, A_{lens})$ is the transmission of the filter as a function of the solid angle and the area of the lens which the ray bundles traverse. The fraction of the isotropically emitted fluorescence which is collected by the lens system is $d\Omega/4\pi$. The limits of the solid angle integral are determined by the location of the area of plasma being integrated over with respect to the optics. The limits of the integral over the area of the laser sheet A_{las} are determined by what area is imaged to the anode in question (see Figure E.4). This expression also uses the fact that the bandwidth of the fluorescence due to the ion velocities is much less than the filter bandwidth

$$0.15\text{Å} \approx \Delta\lambda_{PLIF} \ll \Delta\lambda_{filt} = 10\text{Å},$$

to decouple the velocity integral in $p(\mathbf{x}, t)$ from the integral over the solid angle.

Assuming the ion density may be pulled out of the spatial integral, the relevant optical system parameter used in system performance calculations (see Chapter 5) may be written

$$\alpha_O = \int\int T(\Omega, A_{lens}) \frac{d\Omega}{4\pi} dA_{las} \quad [m^2]. \tag{E.1}$$

The program LENSYS can compute the integration in Eq. E.1 for particular optical systems.

For computation the integral is expressed as

$$\alpha_O = \int_{p_{min}}^{p_{max}} G(p)\, dp \quad [m^2]$$

using the following three integrals

$$G(p) = \int_{q_{min}(p)}^{q_{max}(p)} H(p,q)\, dq$$

$$H(p,q) = H\big(\theta(p,q), \phi(p,q)\big) = \int_{\theta_{min}(p,q)}^{\theta_{max}(p,q)} I(\theta)\sin\theta\, d\theta$$

$$I(\theta) = \int_{\phi_{min}(\theta)}^{\phi_{max}(\theta)} T(\theta,\phi)\, d\phi$$

and a simplified model of the transmission of the filter. The two coordinates p and q are real space coordinates corresponding to the horizontal and vertical directions within the plane of the laser illuminating the plasma (see Figure E.5(a)). The area in p-q space over which the integrals are performed is determined by imaging the anode area at the photocathode back through the lens system to the laser sheet (see Figure E.5(b)). The coordinates θ and ϕ are the polar and azimuthal angles of the polar coordinate system with origin (p_i, q_j) (see Figure E.5(c)). The limits on θ and ϕ are determined the aperture stops of the lens system with respect to the point (p_i, q_i).

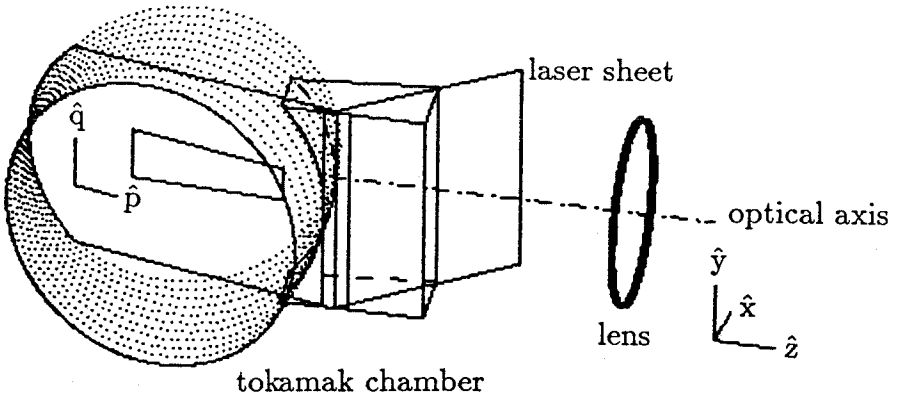

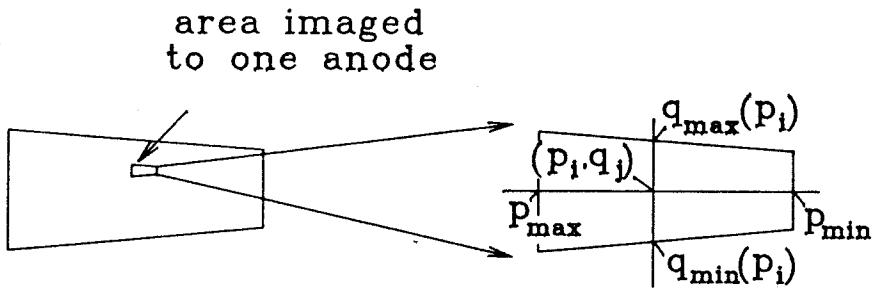

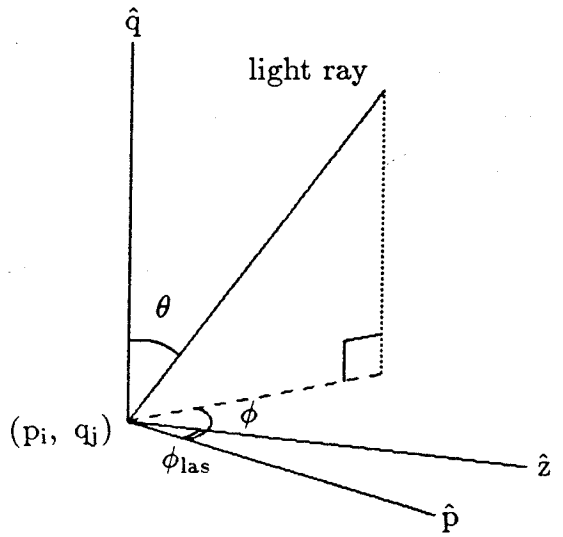

Figure E.5 : Coordinate systems used in optical system calculation. Certain angles are exaggerated for clarity.

The rays used to determine the aperture stops of the system all lie in a plane with the optical axis. Rays of this type are called meridional rays; all other rays are called skew rays. As described in Section B.1, the aperture stops of the system can be determined using paraxial *meridional* matrix ray tracing (Yariv '85) of marginal rays (which happen to be meridional). The angle of incidence of an arbitrary or skew ray must be known to calculate the transmission of the filter (see Conrady '57 for a more complete treatment of skew ray tracing). The approach used in LENSYS (valid in the paraxial approximation) is to decompose each skew ray into a meridional part and a skew part, trace each to the filter and add them at the filter. The advantage to this approach is that the meridional matrix ray tracing can be used throughout, simplifying the programing. Once the angle of incidence is known, the wavelength of the peak of the transmission curve is calculated by the paraxial equation

$$\lambda_\varphi = \lambda_f\left(1 - \frac{\sin^2\varphi}{n^2}\right)^{\frac{1}{2}}$$

with the peak normal transmission at $\lambda_f = 4611\text{Å}$ and the effective index of refraction of the filter $n \approx 2$. A triangular approximation to the measured filter transmission function at normal incidence is used by shifting the peak to λ_φ. The fluorescence $\lambda = 4610\text{Å}$ is slightly shifted from λ_f.

$$T(\varphi) = \begin{cases} T_0\left(1 - \frac{|\lambda - \lambda_\varphi|}{\Delta}\right) & |\lambda - \lambda_\varphi| < \Delta \\ 0 & |\lambda - \lambda_\varphi| \geq \Delta \end{cases}$$

where $\Delta = 8\text{Å}$.

The computationally intensive part of this calculation is determining the limits of the integrals. Given the imaged plasma and the angle of the laser sheet with the optic axis parallel to $\hat{\mathbf{z}}$ (see Figure E.5(a)) the reference frame is rotated into the object plane, i.e., the plane of the laser sheet. The trapezoidal region imaged on a single anode in (p, q) space is *always* bounded by the constants p_{max} and

p_{min} (see Figure E.5(b)). The range of p is divided with a grid. For a given p_i the limits on q can be determined. Given (p_i, q_j) the solid angle to integrate over must be determined.

Consider the spherical coordinate system with origin at (p_i, q_j), θ measured from the $+\hat{q}$ axis (parallel to the $+\hat{\mathbf{y}}$ lab axis) and ϕ measured from an axis parallel to $+\hat{\mathbf{z}}$. The angular extremes of the lens system aperture stop θ_{max}, θ_{min} are determined by checking the lens system aperture stop. Then the θ range is divided with a grid. Given a θ_k, ϕ_{max} and ϕ_{min} are determined and the ϕ range is divided. The angle of incidence on the filter and thus the filter transmission can be calculated by tracing the ray from (p_i, q_j) headed in the direction (θ_k, ϕ_l) through the lens system to the filter. The integration is computed by a series of Romberg integrations with varying grid sizes using Richardson extrapolation (Stoer '80) to increase the convergence rate of the sums as the grid sizes shrink.

Skew Ray Tracing

Using the coordinate conventions above, consider tracing a general skew ray in the direction (θ, ϕ) from (x, y, z) in the laser sheet through a lens. The goal is to reduce the skew ray to two rays which, in the paraxial approximation, can be traced through the lens using the meridional ray matrix formalism. In this formalism the quantities needed are the slope of the ray (in the plane containing the ray and optical axis) and the distance between the point of incidence and the optical axis. Consider the right-hand coordinate system $(\hat{\mathbf{a}}, \hat{\mathbf{b}}, \hat{\mathbf{c}})$, with $\hat{\mathbf{b}} = \hat{\mathbf{z}}$, $\hat{\mathbf{a}}$ perpendicular to the optical axis in the direction pointing to (x, y, z) and $\hat{\mathbf{a}} \times \hat{\mathbf{b}} = \hat{\mathbf{c}}$ (see Figure E.6). Let $\hat{\mathbf{r}}$ be a unit vector in the direction of the ray. With the lens

at (x_l, y_l) in terms of the lab Cartesian coordinates

$$\begin{aligned}
\hat{\mathbf{r}} &= \sin\theta\sin\phi\,\hat{\mathbf{x}} + \cos\theta\,\hat{\mathbf{y}} + \sin\theta\cos\phi\,\hat{\mathbf{z}} \\
\hat{\mathbf{a}} &= \frac{(x_l - x)\,\hat{\mathbf{x}} + (y_l - y)\,\hat{\mathbf{y}}}{[(x_l - x)^2 + (y_l - y)^2]^{\frac{1}{2}}} \\
\hat{\mathbf{c}} &= \frac{(y_l - y)\,\hat{\mathbf{x}} - (x_l - x)\,\hat{\mathbf{y}}}{[(x_l - x)^2 + (y_l - y)^2]^{\frac{1}{2}}}
\end{aligned} \tag{E.2}$$

We can use the meridional ray tracing matrices on the projections of $\hat{\mathbf{r}}$ into the a-b and b-c planes (meridional planes by construction). The vector $\hat{\mathbf{r}}$ can be decomposed into the projection into the a-b plane, a meridional ray, and the *skew part* in the $\hat{\mathbf{c}}$ direction.

$$\begin{aligned}
\mathbf{r_s} &= (\hat{\mathbf{r}}\cdot\hat{\mathbf{c}})\,\hat{\mathbf{c}} \qquad \text{skew part} \\
\mathbf{r_m} &= \hat{\mathbf{r}} - \mathbf{r_s} \qquad \text{meridional ray}
\end{aligned} \tag{E.3}$$

The meridional ray can be treated directly with an off-axis distance $[(x_l - x)^2 + (y_l - y)^2]^{1/2}$ and initial slope

$$\frac{r_{\hat{\mathbf{a}}}}{r_{\hat{\mathbf{z}}}} = \frac{((\sin\theta\sin\phi - r_{s_x})^2 + (\cos\theta - r_{s_y})^2)^{\frac{1}{2}}}{\sin\theta\cos\phi} \tag{E.4}$$

where $r_{\hat{\mathbf{a}}}$ and $r_{\hat{\mathbf{z}}}$ are the meridional ray components in their respective directions and r_{s_i} are components of the $\mathbf{r_s}$. The skew part of the ray is treated as an on axis ray with slope $|\mathbf{r_s}|/r_{\hat{\mathbf{z}}}$.

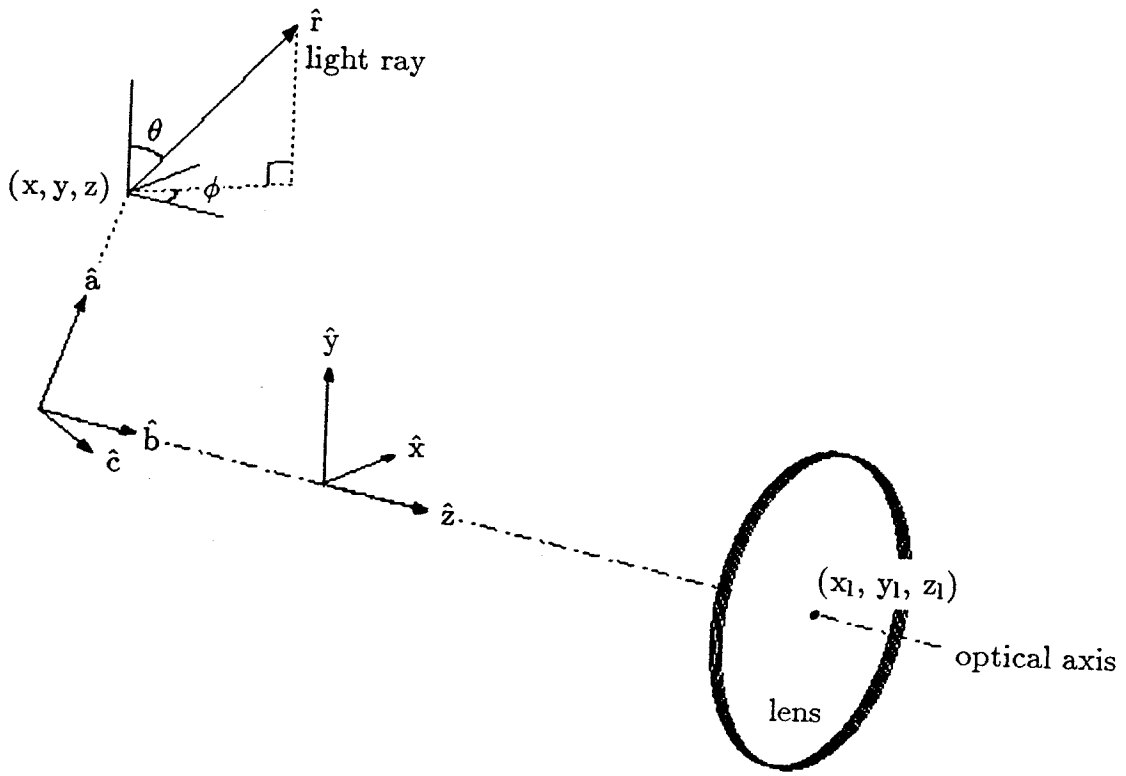

Figure E.6 : Coordinate systems for skew ray tracing.

Appendix F

OTHER COMMENTS

Many theses are read by individuals working on the same experiment trying to reproduce old results as a benchmark for new work. This appendix contains additional comments on the data presented in this thesis along with specific information necessary to retrace my steps.

Figure 2.1 Encore Tokamak — The tokamak has recently had a toroidal cut in the chamber welded shut. This improved the base vacuum attainable from the mid 10^{-6} torr to the high 10^{-7} torr (with all the probes and window ports). It was hoped this would improve the plasma pulse length and repeatablity in other regimes. It did not.

Figure 2.2 Plasma current and loop voltage traces — Below is the BiRa function generator wave form sent to the MB amplifier (after the attenuator) used to make the plasmas used in the thesis.

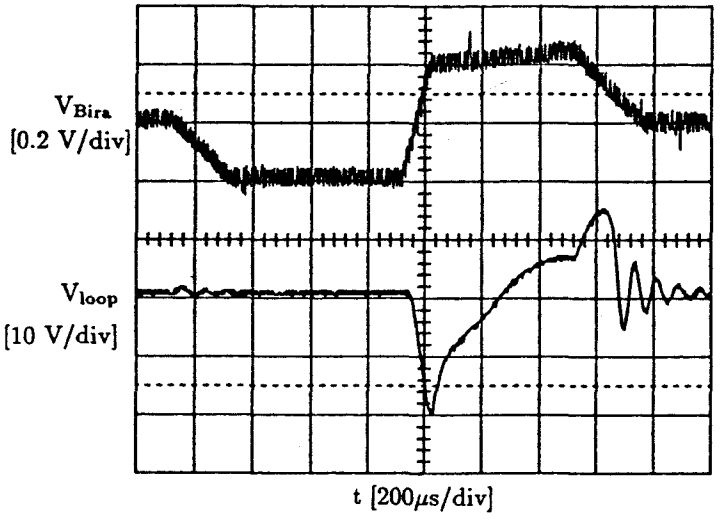

Figure F.1 : BiRa waveform and loop voltage for the plasmas used in the experiments.

Figure 2.5 Plasma I-V trace and T_e *fit* — Below are the errors in the least squares fit used to find T_e. If a fit was especially bad because of the roll-over in the I-V trace, the highest bias voltage points would be dropped and a new fit attempted. The fit with the lowest error was kept.

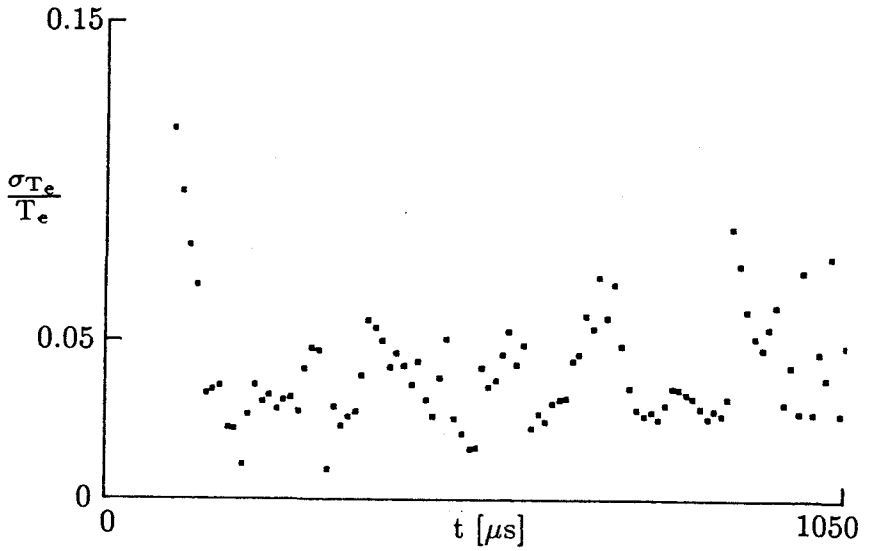

Figure F.2 : Errors in T_e fits for the particular position used in Figure 2.7.

Figure 2.6 Coherent drift wave density fluctuations in the edge — The discharges used during this data run were the most reproducible I could find in the current Encore setup. Figure F.3 shows the changes in the monitored probe traces at their worst and best. The discharges were usually closer to the good match. I estimate the plasmas were reproducible to $\lesssim$20% in amplitude and phase at any given point in the discharge.

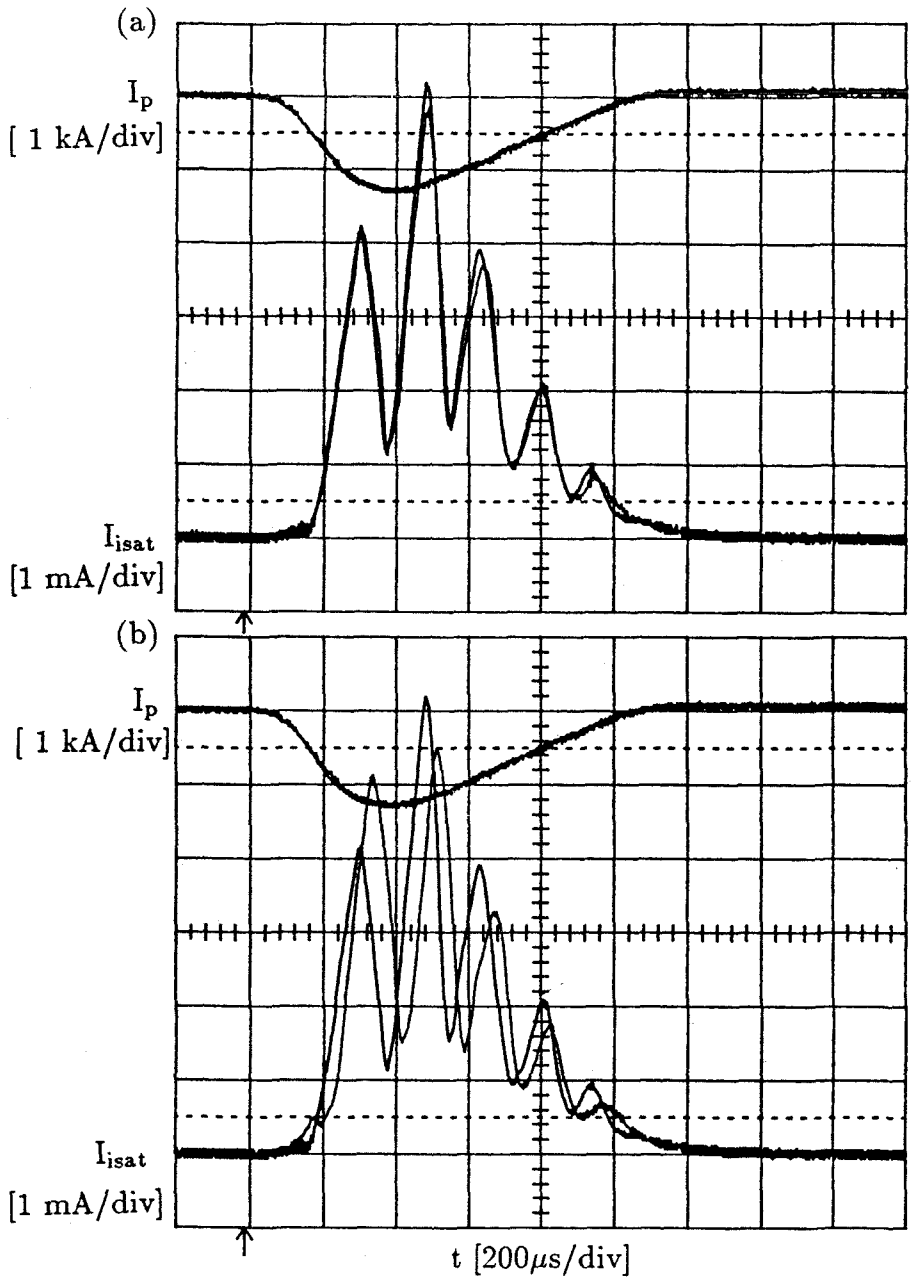

Figure F.3 : Two comparisons between the monitored ion saturation traces saved at 5:10PM with (a) a good match at 10:15AM and (b) the worst possible match at 9:30AM.

Figure 2.7 Plasma parameters at one point — The shape and magnitudes of the plasma parameter oscillations depend on the position in the plasma. In this figure an edge position was displayed. In Figure 6.6 a center position was displayed with the PLIF data.

Figure 4.8 Illustration of power broadening — Data for both figures were calculated using the semi-classical model. Δf_L = 6GHz, (a)T_i = 5eV, (b) T_i = 0.1eV.

Figure 6.6 PLIF data from a single anode — This data was taken in three disk filling PLIF scans. Because the laser was fine-tuned between each run the wavelength shifts were matched at the overlapping times for the data in this figure. The same shifts were used for all the data. Notice the pairs of data points a t = 350 and 750μs in the T_i data set. The errors in the χ^2 fit (see Press '89) are displayed below.

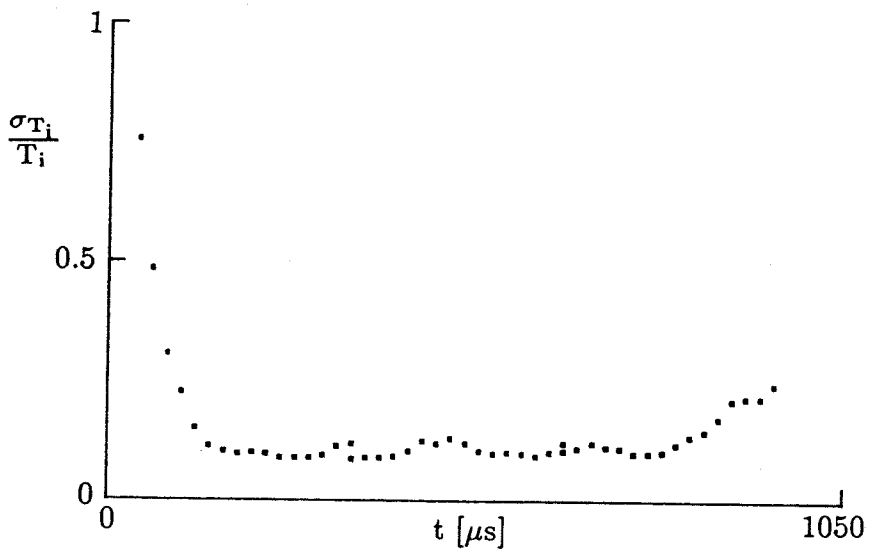

Figure F.4 : Errors in T_i fits for the particular anode used to generate Figure 6.6.

Bibliography

Abe, H. et al. "High-energy tail formation by a monochromatic wave in the magnetized plasma," *Phys. Fluids* **23** , 2417–2424 (1980).

Abe, H. et al. "Resonant heating due to cyclotron subharmonic frequency waves," *Phys. Rev. Lett.* **53** , 1153–1156 (1984).

Anderegg, F. et al., "Ion heating due to rotation and collision in a magnetized plasma," *Phys. Rev. Lett.* **57**, 329–332 (1986).

Arnot, F. L. and W. D. Hart, "Electron transfer in argon," *Proc. Roy. Soc. A* **171**, 383–397 (1939).

Bashkin, S. and J. O. Stoner, Jr., **Atomic Energy Levels and Grotrian Diagrams Vol. 2** (American Elsevier, New York, NY, 1975).

Bechtel, J. H. and A. R. Chraplyvy, "Laser diagnostics of flames, combustion products and sprays," *Proc. IEEE* **70**, 658–677 (1982).

Book, D. L., **NRL plasma formulary** (NRL Publication 177-4405, Washington, DC, 1990).

Bowles, J., R. McWilliams and N. Rynn, "Direct measurement of velocity-space transport in a fully ionized plasma," *Phys. Rev. Lett.* **68**, 1144–1147 (1992).

Burakov, V. S., "Use of the method of resonance fluorescence with a dye laser for plasma diagnostics in the FT-1 tokamak installation," *Pis'ma Zh. Eksp. Teor. Fiz.* **26** 547-550 (1977), *JETP Lett.* **26**, 403–406 (1977).

Burrell, C. F. and H. -J. Kunze, "Observation of resonance scattering on excited helium atoms in a plasma using a tunable dye laser," *Phys. Rev. Lett.* **28**, 1–4 (1972).

Chall, P., E. K. Souw and J. Uhlenbusch, "Laser diagnostics of a low-pressure hollow-cathode arc," *J. Quant. Spectrosc. Radiat. Transfer* **34**, 309–320 (1985).

Cisneros, E. *et al.*, "A low noise pwc cathode readout system," Stanford Linear Accelerator Center, SLAC-PUB-2641, 1980.

Conrady, A. E., **Applied Optics and Optical Design** (Dover, New York, NY, 1957).

Cramer, W. H., "Elastic and inelastic scattering of low-velocity ions: Ne^+ in A, A^+ in Ne, and A^+ in A," *J. Chem. Phys.* **30**, 641–642 (1959).

Dahm, W. J. A. and P. E. Dimotakis, "Mixing at large Schmidt number in the self-similar far field of turbulent jets," *J. Fluid Mech.* **217**, 299–330 (1990).

Davis, C. C and T. A. King, "Gaseous Ion Lasers," in **Advances in Quantum Electronics Vol. 3** edited by D. W. Goodwin (Academic Press, NY, NY, 1975).

the self-similar far field of turbulent jets," *J. Fluid Mech.* **217**, 299–330 (1990).

Dimock, D., E. Hinnov and L. C. Johnson, "Plasma diagnostics with ionized barium and tunable dye lasers," *Phys. Fluids* **12**, 1730–1732 (1969).

Doveil, F., "Stochastic plasma heating by a large-amplitude standing wave," *Phys. Rev. Lett.* **46**, 532–534 (1981).

Drake, J. F. and T. T. Lee, "Irreversibility and transport in the lower hybrid drift instability," *Phys. Fluids* **24**, 1115–1125 (1981).

Drummond, J. E., "Basic microwave properties of hot magnetoplasmas," *Phys. Rev.* **110**, 293–306 (1958).

Dyer, M. J. and D. R. Crosley "Two-dimensional imaging of OH laser induced fluorescence in a flame," *Opt. Lett.* **7**, 382–384 (1982).

Fasoli, A. et al., "Direct measurement of ion phase-space orbits in an electrostatic field," *Phys. Rev. Lett.* **63**, 2052–2055 (1989).

Fasoli, A. et al., "Dynamical chaos of plasma ions in electrostatic waves," *Phys. Rev. Lett.* **70**, 303–306 (1993).

Forslund, D. W., R. L. Morse and C. W. Nielson, "Nonlinear electron-cyclotron drift instability and turbulence," *Phys. Rev. Lett.* **27**, 1424–1428 (1971).

Forslund, D. W. et al., "Electron cyclotron drift instability and turbulence," *Phys. Fluids* **15**, 1303–1318 (1972).

Fredrickson, E. D. and P. M. Bellan, "Investigation of finite beta modified drift wave in a tokamak plasma," *Phys. Fluids* **28**, 1866–1876 (1985).

Fukuyama, A. et al., "Stochastic acceleration by an electrostatic wave near ion cyclotron harmonics," *Phys. Rev. Lett.* **38** , 701–704 (1977).

García, G. and J. Campos, "Lifetimes and transition probabilities of Ar(II)," *J. Quant. Spectrosc. Radiat. Transf.* **34**, 85–94 (1985).

Gell, Y. and R. Nakach, "Stochastic ion heating by an electrostatic wave in a sheared magnetic field," *Phys. Fluids* **23**, 1646–1655 (1980).

Goeckner, M. J. and J. Goree, "Laser-induced fluorescence measurement of plasma ion temperatures: correction for power saturation," *J. Vac. Sci. Technol. A* **7**, 977-981 (1989).

Goeckner, M. J., J. Goree and T. E. Sheridan, "Laser-induced fluorescence characterization of a multidipole filament plasma," *Phys. Fluids B* **3**, 2913–2921 (1991).

Groebner, R. J., K. H. Burrell and R. P. Seraydarian, "Role of edge electric field and poloidal rotation in the L-H transition," *Phys. Rev. Lett* **64**, 3015 (1990).

Hecht, E. and A. Zajac, **Optics** (Addison-Wesley Publishing Co., Reading, MA, 1974).

Hinnov, E. et al., "Spectroscopic observations of fully ionized barium plasma," *Phys. Fluids* **6**, 1779–1780 (1963).

Hoffman, F. W., "Ion density measurement in a barium plasma by scattering of resonance radiation," *Phys. Fluids* **7**, 532–536 (1964).

Hsu, J. Y et al.,"Stochastic heating of a large-amplitude standing wave," *Phys. Rev. Lett.* **43**, 203–206 (1979).

Hutchinson, I. H., **Principles of Plasma Diagnostics** (Cambridge University Press, New York, NY, 1987).

Ida, K. et al., "Edge electric field profiles of H-mode plasmas in the JFT-2M tokamak," Phys. Rev. Lett. **65**, 1364 (1990).

Kadomtsev, B. B., **Plasma Turbulence** (Academic Press, London, 1965).

Kadota, K. and Y. Kaneko, "Secondary electron ejection from contaminated metal surface by He and Ar atoms," *Jpn. J. Appl. Phys.* **13**, 1554–1561 (1974).

Karimabadi, H. et al., "Particle acceleration by a wave in a strong magnetic field: regular and stochastic motion," *Phys. Fluids B* **2**, 606–628 (1990).

Karney, C. F. F. and A. Bers, "Stochastic ion heating by a perpendicularly propagating electrostatic wave," *Phys. Rev. Lett.* **39**, 550–554 (1977).

Karney, C. F. F., "Stochastic ion heating by a lower hybrid wave," *Phys. Fluids* **21**, 1584–1599 (1978).

Karney, C. F. F., "Stochastic ion heating by a lower hybrid wave: II," *Phys. Fluids* **22**, 2188–2209 (1979).

Kinsey, J. L., "Laser induced fluorescence," *Ann. Rev. Phys. Chem.* **28**, 349–372 (1977).

Kitaeva, V. F., A. N. Odintsov and N. N. Sobolev, "Continuously operating argon ion lasers," *Sov. Phys. Uspekhi* **12**, 699–730 (1970).

Kychakoff, G. et al., "Quantitative visualization of combustion species in a plane," *Appl. Opt.* **21**, 3225–3226 (1982).

Kychakoff, G., R. D. Howe and R. K. Hanson, "Quantitative flow visualization technique for measurements in combustion gases," *Applied Optics* **23**, 704–712 (1984).

Luyken, B. F. J., "Transition probabilities and radiation lifetimes for ArII," *Physica* **60**, 432–458 (1972).

Malkov, M. A. and G. M. Zaslavskiĭ, "Wave-particle resonant interaction in a weak magnetic field," *Phys. Lett.* **106A**, 257–260 (1984).

McChesney, J. M., R. A. Stern and P. M. Bellan, "Observation of fast stochastic ion heating by drift waves," *Phys. Rev. Lett.* **59**, 1436–1439 (1987).

McChesney, J. M., "Observation of stochastic ion heating by low frequency drift waves," California Institute of Technology Ph.D. thesis, (1989).

McChesney, J. M., P. M. Bellan and R. A. Stern, "Observation of fast stochastic ion heating by drift waves," *Phys. Fluids B* **3**, 3363–3378 (1991).

McWilliams, R. et al.,"Cross-field transport and heating due to parametric decay of lower hybrid waves," *Phys. Rev. Lett.* **50**, 836–839 (1983).

McWilliams, R. and D. Sheehan, "Experimental measurements of phase space," *Phys. Rev. Lett.* **56**, 2485–2488 (1986).

McWilliams, R. and M. Okubo, "The transport of test ions in a quiet plasma," *Phys. Fluids* **30**, 2849–2854 (1987).

McWilliams, R., M. K. Okubo and N. S. Wolf, "The transport of ions in a turbulent plasma," *Phys. Fluids B* **2**, 523–529 (1990).

Measures, R. M., "Selective excitation spectroscopy and some possible applications," *J. Appl. Phys.* **39** , 5232–5245 (1968).

Meng, H. C. and H. -J. Kunze, "Investigation of the diffusion of impurity atoms in plasmas by laser fluorescence," *Phys. Fluids* **22**, 1082–1088 (1979).

Montgomery, D. C., **Theory of the Unmagnetized Plasma** (Gordon and Breach Science Publishers, New York, NY, 1971).

Moore, C. A.,G. P. Davis and R. A. Gottscho, "Sensitive, nonintrusive, *in-situ* measurement of temporally and spatially resolved plasma electric fields," *Phys. Rev. Lett.* **52**, 538–541 (1984).

Norlén, G., "Wavelength and energy levels of ArI and ArII based on new interferometric measurements in the region 3400-9800 Å," *Physica Scripta* **8**, 249–268 (1973).

O'Neil, T. "Collisionless damping of nonlinear plasma oscillations," *Phys. Fluids* **8**, 2255–2262 (1965).

Peyser, T. and G. C. Goldenbaum, "Plasma rotation during spheromak formation," *Phys. Rev. Lett.* **61**, 955 (1988).

Poincaré, H. , **Les Méthodes Nouvelles de la Mécanique Céleste 3 vols.** (Gauthier-Villars, Paris, 1899).

Press, W.H. et al., **Numerical Recipies** (Cambridge University Press, New York, NY, 1989).

Rechester, A. B. and T. H. Stix, "Stochastic instability of nonlinear oscillator," *Phys. Rev. A* **19**, 1656–1665 (1979).

Rosenbluth, M. N. and R. Rostoker, Proc. 2nd Intern. Conf., Geneva, **31**, 144 (1958).

Rosner, S. D., T. D. Gaily and R. A Holt, "Laser fluorescence measurement of relative electron impact cross sections for metastable states of Ar^+ and Xe^+," *J. Phys. B: Atom. Molec. Phys.* **9**, L489–L491 (1976).

Sagdeev, R. Z. and V. D. Shafranov, Proc. 2nd Intern. Conf., Geneva, **31**, 118 (1958).

Schweer, B. et al., "Measurement of the density and velocity distribution of neutral Fe in ISX-B by laser fluorescence spectroscopy," *J. Nucl. Mat.* **93**, 357–362 (1980).

Silfvast, W. T., D. Y. Al-Salameh and O. R. Wood II, "Multielectron photoionization to the $3p^4 4p$ configuration of Ar^+: Experiment and theory," *Phys. Rev. A* **34**, 5164–5167 (1986).

Skiff, F., F. Anderegg and M. Q Tran, "Stochastic particle acceleration in an electrostatic wave," *Phys. Rev. Lett.* **58**, 1430–1433 (1987a).

Skiff, F. and F. Anderegg, "Direct observation of plasma dielectric motion," *Phys. Rev. Lett.* **59**, 896–899 (1987b).

Skiff, F. et al., "Conservation laws and transport in Hamiltonian chaos," *Phys. Rev. Lett.* **61**, 2034–2037 (1988).

Smith, G. R. and A. N. Kaufman, "Stochastic acceleration by a single wave in a magnetic field," *Phys. Rev. Lett.* **34**, 1613–1616 (1975).

Smith, G. R. and A. N. Kaufman, "Stochastic acceleration by an obliquely propagating wave—an example of overlapping resonances," *Phys. Fluids* **21**, 2230–2241 (1978).

Stern, R. A. and J. A. Johnson, III "Plasma ion diagnostics using resonant fluorescence," *Phys. Rev. Lett.* **34** , 1548–1551 (1975).

Stern, R. A. et al.,"Nonlocal effects in the electrostatic ion-cyclotron instability," *Phys. Rev. Lett.* **37**, 833–836 (1976).

Stern, R. A., "Particle kinetics of selective excitation spectroscopy," *Phys. Fluids* **21**, 1287–1294 (1978).

Stern, R. A., D. N. Hill and N. Rynn, "Azimuthal coherent ion-ring–beam generation in unstable magnetized plasmas," *Phys. Rev. Lett.* **47**, 792–795 (1981).

Stern, R. A., D. N. Hill and N. Rynn, "Direct ion-transport measurement by optical tagging," *Phys. Lett. A* **93**, 127–130 (1983).

Stern, R. A., "Laser/ion-beam diagnostics for potential and magnetic-field measurements in plasmas," *Rev. Sci. Instrum.* **56**, 1006–1011 (1985).

Stoer, J. and R. Bulirsch, **Introduction to Numerical Analysis** (Spinger-Verlag, New York, NY, 1980).

Striganov, A. R. and N. S Sventitskii, **Tables of Spectral Lines of Neutral and Ionized Atoms** (Plenum, New York, NY, 1968).

Swanson, D. G., **Plasma Waves** (Academic Press, Inc., San Diego, CA, 1989).

Turner, W. C. et al., "Investigations of the magnetic structure and decay of a plasma-gun-generated compact torus," *Phys. Fluids* **26**, 1965–1986 (1983).

Varga, P., W. Hofer and H. Winter, "Apparent cross sections for metastable ion production by electron impact," *J. Phys. B: At. Mol. Phys.* **14**, 1341–1351 (1981).

Watanabe, Y. et al., "Study on electron density dependence of metastable Ar^+ density in pulsed-discharge plasma by using LIF method," *Jpn. J. Appl. Phys.* **26**, 184–185 (1987).

Wesson, J., **Tokamaks** (Oxford University Press, New York, NY, 1987).

Wiggins, S., **Introduction to Applied Nonlinear Dynamical Systems and Chaos** (Springer-Verlag, New York, NY, 1990).

Wiza, J. L., "Microchannel plate detectors," *Nucl. Instr. and Meth.* **162**, 587–601 (1979).

Wood, R. W., **Physical Optics 1934 Third Edition** (Optical Society of America, Washington, DC, 1988).

Yariv, A., **Optical Electronics** (Holt, Rinehart and Winston, Inc., New York, NY, 1985).

Zaslavskiĭ, G. M. and N. N. Filonenko, "Stochastic instability of trapped particles and conditions of applicability of the quasi-linear approximation," *Zh. Eksp. Teor.* **54**, 1590–1602 (1968), *Sov. Phys. JETP* **25**, 851–857 (1968).

Zaslavskiĭ, G. M. and B. V. Chirikov,"Stochastic instability of non-linear oscillation," *Usp. Fiz. Nauk.* **105**, 3–39 (1971), *Sov. Phys.-Usp.* **14** 549–568 (1972).

Zaslavskiĭ, G. M. et al., "Mechanism for enhanced diffusion in a wave-particle interaction in a weak magnetic field," *Fiz. Plazmy* **15**, 631–634 (1989), *Sov. J. Plasma Phys.* **15**, 368–370 (1989).